*minerals*

MDPI

*Article*

# Syn-Sedimentary Exhalative or Diagenetic Replacement? Multi-Proxy Evidence for Origin of Metamorphosed Stratiform Barite–Sulfide Deposits near Aberfeldy, Scottish Highlands

**Norman R. Moles [1,*], Adrian J. Boyce [2], Matthew R. Warke [3,†] and Mark W. Claire [4]**

[1] School of Applied Sciences, University of Brighton, Cockcroft Building, Lewes Road, Brighton BN2 4GJ, UK
[2] Scottish Universities Environmental Research Centre (SUERC), Rankine Avenue, Scottish Enterprise Technology Park, East Kilbride, Glasgow G75 0QF, UK; adrian.boyce@glasgow.ac.uk
[3] School of Earth and Environmental Sciences, Bute Building, University of St Andrews, St Andrews KY16 9TS, UK; mwarke438@gmail.com
[4] Blue Marble Space Institute of Science, 600 1st Avenue, Seattle, WA 98104, USA; mark@bmsis.org
* Correspondence: n.moles@brighton.ac.uk
† Current address: Taylor and Francis Group, Abingdon OX14 4RN, UK.

**Abstract:** Bedded barite, Fe-Zn-Pb sulfides, carbonates, and cherts within Ediacaran (Dalradian Supergroup) graphitic metasediments near Aberfeldy in Scotland have previously been interpreted as chemical sediments precipitated from hydrothermal fluids episodically exhaled into marine basins filled with organic-rich mud, silt, and sand. Lithological variation and compositional diversity in pyrite and sphalerite reflect varied redox environments and proximity to hydrothermal discharges. Thick beds (>2 m) of barite have relatively uniform $\delta^{34}S$ of +36 ± 1.5‰, considered to represent contemporaneous seawater sulfate, as negative $\Delta^{17}O$ indicates incorporation of atmospheric oxygen during precipitation in the water column. However, certain features suggest that diagenetic processes involving microbial sulfate reduction modified the mineralogy and isotopic composition of the mineralization. Barite bed margins show decimeter-scale variation in $\delta^{34}S$ (+32 to +41‰) and $\delta^{18}O$ (+8 to +21‰), attributed to fluid-mediated transfer of dissolved barium and sulfate between originally porous barite and adjacent sediments, in which millimetric sulfate crystals grew across sedimentary lamination. Encapsulated micron-sized barium carbonates indicate early diagenetic barite dissolution with incorporation of sulfur into pyrite, elevating pyrite $\delta^{34}S$. Subsequently, sulfidation reactions produced volumetrically minor secondary barite with $\delta^{34}S$ of +16 to +22‰. Overall, these processes affected small volumes of the mineralization, which originally formed on the seafloor as a classic SEDEX deposit.

**Keywords:** stratabound barite; Neoproterozoic; sulfur isotopes; triple-oxygen isotopes; sulfate reduction; barium carbonates; SEDEX deposit; diagenetic replacement

check for updates

**Citation:** Moles, N.R.; Boyce, A.J.; Warke, M.R.; Claire, M.W. Syn-Sedimentary Exhalative or Diagenetic Replacement? Multi-Proxy Evidence for Origin of Metamorphosed Stratiform Barite–Sulfide Deposits near Aberfeldy, Scottish Highlands. *Minerals* **2024**, *14*, 865. https://doi.org/10.3390/min14090865

Academic Editor: Pierfranco Lattanzi

Received: 22 July 2024
Revised: 20 August 2024
Accepted: 22 August 2024
Published: 25 August 2024

**Copyright:** © 2024 by the authors. Licensee MDPI, Basel, Switzerland. This article is an open access article distributed under the terms and conditions of the Creative Commons Attribution (CC BY) license (https://creativecommons.org/licenses/by/4.0/).

## 1. Introduction

In the geological record, disseminated or massively bedded barite is found in a range of environments, notably within clastic and chemical sedimentary successions and associated with clastic-dominant (CD-type) Zn–Pb sulfide deposits, volcanogenic massive sulfide, and Mississippi Valley-type (MVT) Zn–Pb sulfide deposits [1,2]. In modern marine environments, barite deposits occur in cold seep, diagenetic, hydrothermal, and pelagic settings [3–6] (Table 1). Barite precipitation requires the mixing of barium-rich and sulfate-poor fluids with sulfate-bearing fluids, and in the modern ocean this is usually below the sediment–water interface unless hydrothermal fluids are involved [7].

There are three main theories for the formation of stratiform barite deposits: (i) exhalation of hydrothermal fluids into seawater with syn-sedimentary precipitation of barite ± sulfides, referred to as sedimentary exhalative or SEDEX deposits [8–11] hosted by clastic

sediments (CD-type) or limestones (some Irish-type deposits e.g., [12]), (ii) seafloor precipitates associated with submarine methane seepage [13–17], and (iii) barite precipitation through biogenic processes in the water column or at shallow depths within marine sediments, with subsequent remobilization into beds during diagenesis [2–4,18–20]. These theories are not mutually exclusive; for example, burial diagenesis may remobilize barite originally precipitated from a SEDEX or seafloor cold seepage deposit.

**Table 1.** A simple classification of stratabound bedded barite deposits and their main characteristics, compiled from various sources [3,6,15,20–22].

| Deposit Model | SEDEX/CD-Type [1] | Carbonate-Hosted [2] | Biogenic/Cold Seep |
|---|---|---|---|
| Predominant age(s) | Proterozoic | Phanerozoic | Paleozoic, Recent |
| Lateral extent | Extensive (kms) | Intermediate (100s m) | Localized (10s m) |
| Associated Ba silicates | Common | Uncommon | Absent |
| Associated sulfides | Often [3] | Frequent | Absent |
| Range in barite $\delta^{34}S$ | Wide: seawater values in open systems, divergent due to MSR/TSR [4] in closed systems | Wide: seawater values in stratiform barite, divergent in discordant barite | Very wide: from seawater values to +80‰ |
| Range in barite $\delta^{18}O$ | Typically limited: seawater ± 6‰, may covary with $\delta^{34}S$ | Limited data: some deposits have seawater values, others are divergent | Very wide: from seawater values to +30‰, positive association with $\delta^{34}S$ |
| Range in barite $^{87}Sr/^{86}Sr$ | 0.704–0.707 similar to hydrothermal fluid | From seawater to basinal sediment values | 0.708–0.711 similar to terrigenous material |
| Ba and Sr source | Basinal brines: aluminosilicate alteration during deep burial | Basinal brines or hydrothermal circulation through basement | Porewaters: biogenic sediments during shallow burial |
| Sulfate source | Seawater | Seawater, porewater | Seawater/porewater |

[1] Sedimentary exhalative, also known as clastic-dominant (CD)-type deposits. [2] Mississippi Valley-type (MVT) and Irish-type strata-bound barite deposits. [3] Apart from in the sulfate-limited euxinic seawater model [21], in which the hydrothermal fluid is depleted in base metals as sulfides precipitate and the remaining Ba-rich fluid precipitates barite elsewhere. [4] MSR = microbial (including bacterial) sulfate reduction; TSR = thermochemical sulfate reduction.

Distinguishing between these various modes of formation can be challenging, and this has resulted in controversy in the literature on bedded barite deposits. In the past twenty or so years, many deposits that were originally described as SEDEX have been re-interpreted as diagenetic replacement in origin (Figure 1b,c) [22–24], while others have been recognized as examples of 'fossil' cold seepage deposits formed in low-temperature conditions [2,6,14,16,20]. The term SEDEX was initially used by Carne and Cathro (1982) [25] to categorize a group of Canadian ore deposits that included laminated, exhalative sulfides. This usage was subsequently expanded to encompass a diverse group of deposits containing laminated sulfides and/or barite hosted by clastic, carbonate, and metasedimentary rocks. In a review of sediment-hosted Pb–Zn sulfide deposits globally, Leach et al. (2005) [8] stated that, "Despite the "exhalative" component inherent in the term "SEDEX", direct evidence of an exhalite in the ore or alteration component is not essential for a deposit to be classified as SEDEX. The presence of laminated sulfides parallel to bedding is assumed to be permissive evidence for exhalative ores. The distinction between some SEDEX and MVT deposits can be quite subjective because some SEDEX ores replaced carbonate, whereas some MVT deposits formed in an early diagenetic environment and display laminated ore textures".

Stratiform barite and sulfide deposits typically form in continental-margin rift-basin settings, and as such, are prone to orogenic deformation and metamorphism during plate collision. Regional metamorphism can result in substantial recrystallization and remobilization that tends to obscure or destroy the original fine textural details, micron-scale geochemical variations, and primary fluid inclusions, which would otherwise provide evidence for ore genesis [6]. Nevertheless, even strongly metamorphosed sediment-hosted ore deposits may preserve textural, mineralogical, geochemical, and isotopic characteristics

of their unmetamorphosed precursors [26–28], and thus these characteristics may be used to illuminate the primary ore-forming processes in metamorphosed deposits.

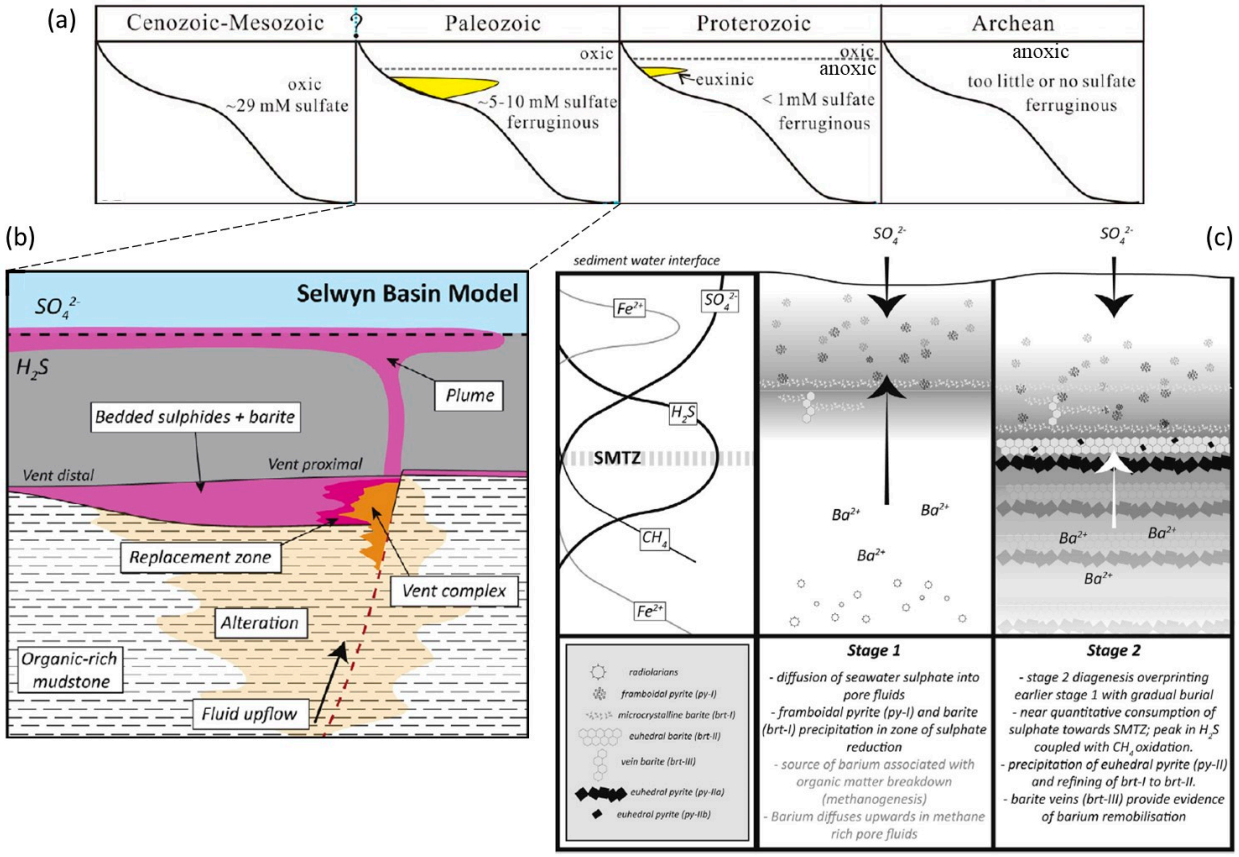


**Figure 1.** (**a**) Schematic sections of continental shelf environments, summarizing key differences in ocean chemistry and stratification during four periods of Earth history, from Han et al. (2022) [21]. Yellow-filled volume indicates inferred euxinic conditions. The "?" indicates uncertainty in the timing of the transition in the global ocean redox state from stratified to fully oxygenated. (**b**) Schematic section from Magnall et al. (2016) [23] illustrating the conventional sedimentary-exhalative (SEDEX) model for Paleozoic (Late Devonian) formation of mineralization in the Selwyn Basin, in which sulfide and barite precipitation occurs, in vent proximal and vent distal locations, from a stratified, euxinic water column. (**c**) Schematic model by Magnall et al. (2016) [23] for the diagenetic formation of sulfide and barite mineralization at Macmillan Pass, Selwyn Basin. Inferred key geochemical parameters ($Fe^{2+}$, $SO_4^{2-}$, $CH_4$, and $H_2S$) of pore water profiles are shown to the left. The sulfate–methane transition zone (SMTZ) occurs where diffusional gradients of sulfate and methane meet, resulting in peak concentrations of reduced sulfur associated with pyrite precipitation and $Ba^{2+}$ remobilization. Figures (**b**,**c**) reprinted from [23] under the CC BY-NC-ND license, Elsevier 2016.

Barite itself is a valuable indicator of depositional and diagenetic processes due to its varying mineral chemistry and stable isotope composition ($\delta^{34}S$, $\delta^{18}O$, and $^{87}Sr/^{86}Sr$) [1,6,21,29,30]. Provided that oxic conditions prevail, crystals of barite are not prone to diagenetic alteration after burial [31] because barite has an extremely low solubility in such environments [1,32]. However, barite is soluble under reducing conditions, especially in the presence of sulfate-reducing microbes and organic matter [20]. Therefore, dissolution of barite can occur during diagenesis, where conditions of low redox and low alkalinity prevail. Jewell (2000) [3] remarked that diagenetic alteration of fine-grained barite is an expected consequence of any early sediment diagenesis that includes sulfate reduction.

Important factors when considering pre-Phanerozoic marine environments are the dramatic changes in ocean chemistry and biota that occurred throughout this period of

Earth's history, especially accompanying global glaciations ('Snowball Earth' episodes) and changes in oxygenation of the water column (Figure 1a). Consequently, processes occurring in modern ocean sediments and deduced for Phanerozoic deposits are not necessarily relevant to Proterozoic contexts. Differences from the Phanerozoic in the Proterozoic and Archaean include the lack of bioturbation in marine sediments and prevalence of reducing bottom-water conditions [21,25,33,34]. The Cryogenian and Ediacaran periods of the late Proterozoic are marked by changes to the sulfur cycle [35] and a sustained increase in marine sulfate concentrations [36]. As noted by Crockford et al. (2019a) [36], inferring modes of deposition based on isotopic signatures that are diagnostic of different modern environments [37] is tenuous when applied to Proterozoic deposits.

In this paper, we describe regionally metamorphosed (to amphibolite facies) Neoproterozoic (Ediacaran) barite-, sulfide-, and carbonate-rich stratiform mineralization, interbedded with organic-rich marine sediments, outcropping near the town of Aberfeldy in the Grampian Highlands of Scotland, UK. We summarize key aspects of the morphology and petrography of the mineralized beds, and present analytical results from several mineralogical and isotopic investigations that enable a critical evaluation of the relative contributions of seafloor precipitation (the exhalative model) and of microbial- and diffusion-controlled diagenetic replacement processes in the genesis of the mineralization.

## 2. The Aberfeldy Barite Deposits

### *2.1. Geological Setting*

The Aberfeldy deposits, located in a hilly moorland region in the Grampian Highlands (Figure 2a), comprise the largest industrial resource of barite in the UK [38]. They are individually named (from west to east) Foss, Ben Eagach, and Duntanlich, with Foss subdivided into Foss West (where barite was mined) and Foss East (not exploited). The deposits were discovered in the late 1970s by the British Geological Survey, then named the Institute of Geological Sciences [39,40]. Barite production at the Foss Mine and adjacent Open Pits (Figure 2e) commenced in the early 1980s, and in recent years about 40,000 metric tons of barite rock has been extracted annually by M-I SWACO, a Schlumberger company. Before closure in 2021, Foss Mine produced over 1 million tons with a similar resource remaining at depth [41] in a structurally complex, folded, and stretched orebody. In the nearby Duntanlich deposit (Figure 2d), a resource of at least 7.5 million metric tons of barite [42] occurs in a structurally simple, steeply inclined tabular orebody, from which underground extraction commenced in 2022.

The Foss and Duntanlich orebodies are around 4 km apart and hosted in the same metasedimentary unit, the Ben Eagach Schist Formation [43,44] (Figure 2b,c). This formation comprises mainly graphitic quartz muscovite schist, the protolith of which was organic-rich mudstone and siltstone. In the vicinity of the deposits, the formation is enriched in barium, zinc, and lead [39,40,45,46]. Locally, the schists are calcareous and contain beds of graphitic dolostone. The stratigraphically overlying Ben Lawers Schist Formation is calcareous and non-sulfidic and contains bedded barite and chert only in the lowermost strata [39,40,44,45] (Figure 2c).

Pyrite Re-Os dating by Moles and Selby (2023) [44] of samples of stratiform mineralization from the Foss Mine and Duntanlich deposit yield mid-Ediacaran ages (604.0 $\pm$ 7.2 Ma and 612.1 $\pm$ 18.6 Ma, respectively, with two-sigma overlap). The authors interpreted this as the age of sedimentation or early diagenesis. However, other researchers suggest that these dates represent a subsequent event ~20 Ma younger than sedimentation [47].

Volumetrically minor components of both formations are metamorphosed mafic igneous rocks (metabasite), the protoliths of which were contemporaneous pyroclastic sediments and subsequently intruded sills of basaltic rock. In the Foss deposit, a thin (5–40 cm) but laterally extensive metabasite bed directly underlying the lower mineralized bed is a valuable marker horizon for this bed (Figure 2c). Mafic volcanism became prevalent above the Ben Lawers Schist during deposition of the Farragon Beds (Figure 2c). The presence of mafic volcanic components together with the stratiform mineralization has been interpreted

as evidence of high heat flow and convective circulation of hydrothermal fluids in a passive continental margin rifting environment [38,40,48,49]. This continent was Laurentia and rifting eventually resulted in opening of the Iapetus Ocean [50].

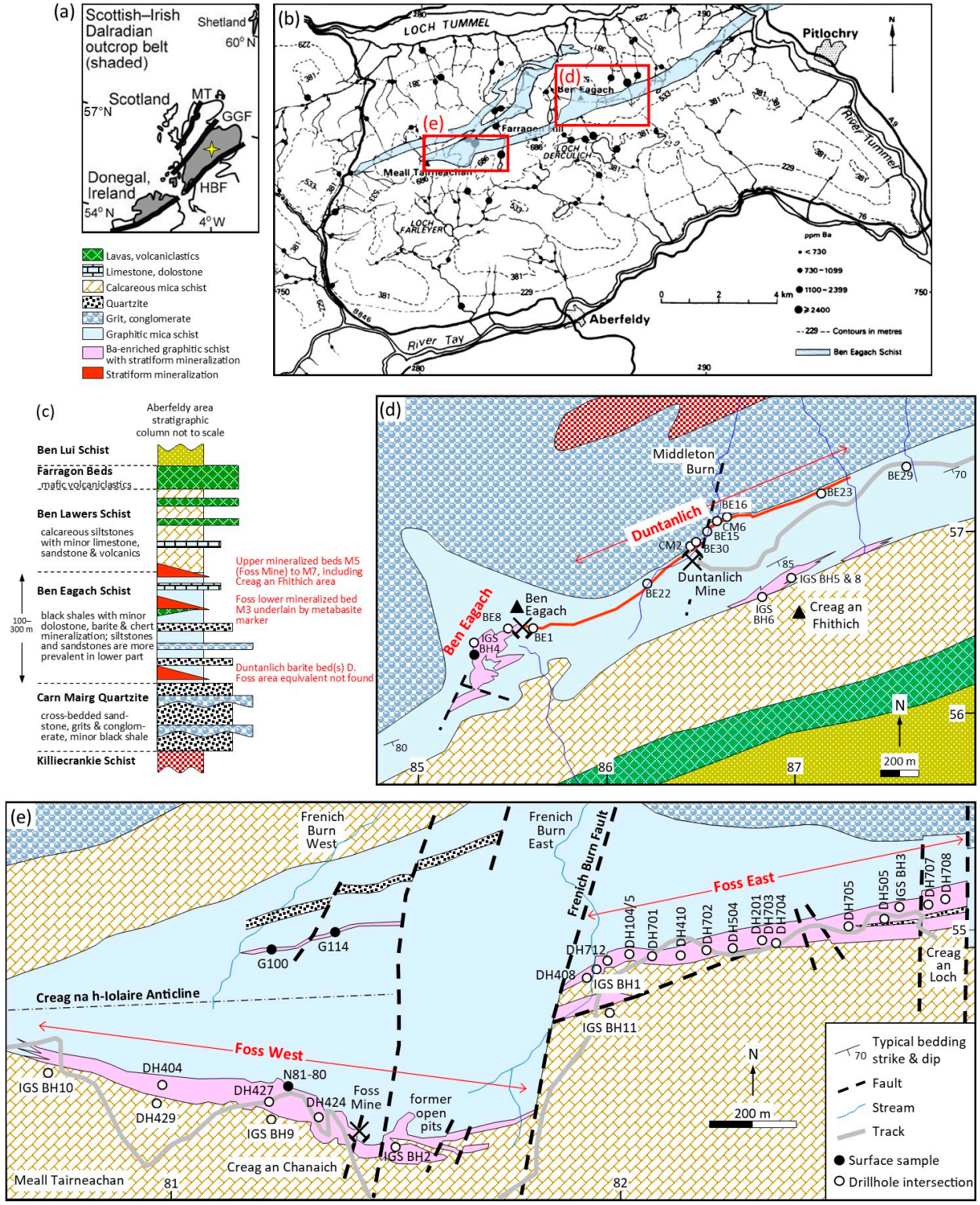


**Figure 2.** (**a**) Location of the Aberfeldy area (yellow star) within the Scottish–Irish Dalradian Supergroup outcrop bounded by the Highland Border Fault (HBF) and Great Glen Fault (GGF). MT = Moine

Thrust. (**b**) Map from Coats et al. (1981) [40] of the area north of Aberfeldy with outcrop of the Ben Eagach Schist formation (pale blue). Black-filled circles are stream sediment sample locations, with the symbol size proportional to the classified barium content. Elevated amounts of barium in these sediments led to the discovery of the barite deposits by the IGS (now BGS). Red boxes indicate locations of the maps in (**d**,**e**). (**c**) Stratigraphy of the Easdale Subgroup of the Dalradian Supergroup in the Aberfeldy area, adapted from Ruffell et al. (1998) [51], indicating the locations of stratiform mineralization. (**d**) Geological map of the Ben Eagach–Duntanlich deposit area with locations of samples. (**e**) Geological map of the Foss deposit area with locations of samples. Maps incorporate information from IGS (Coats et al., 1981) [40] and Dresser Minerals. Bedding is close to vertical, and strata young southwards, except in Foss West to the north of the Creag na h-Iolaire Anticline, where strata young northwards.

### *2.2. Stratabound Mineralization*

Marble-like, granoblastic-textured barite rock occurs in beds up to several meters thick where it is mined. The barite rock usually shows zebra-like banding with white, pure barite rock alternating with darker barite rock that contains minor disseminated pyrite and other minerals (Figure 3a,b,e). The mineralized beds have sharp boundaries with the enclosing metasediments, and clastic sediment is rarely incorporated into barite rock [45,52]. These features suggest rapid deposition of the barite during hydrothermal exhalative episodes that were vigorous but short-lived and episodic. Seven such episodes are represented in the Foss deposit (labeled M1 to M7) and possibly three episodes formed the Duntanlich mineralized bed. Occasionally, barite clasts can be discerned within conglomeratic barite rock (Figure 3c), which has been interpreted [44,52] as indicating localized reworking of cemented barite sediment in a shallow-water environment.

The barite beds are usually enveloped in chert-like rocks that are rich in quartz and the barium aluminosilicates cymrite, celsian, Ba-K-Na feldspar, and mica [45,53]. These lithologies extend laterally further than the barite, such that chert is dominant in parts of the deposits distal from the locations of presumed hydrothermal vents where the barite beds are thickest. In some parts of the deposits, carbonate rocks (calcite, dolomite) and sulfide rocks (mainly pyrite, with less sphalerite and galena) occur within the mineralized beds (Figure 3f,g). Occasionally, all of these components occur together, forming laminated beds (Figure 3d). Disseminated magnetite locally occurs within thicker beds of barite [40]. Pyrrhotite is a rare component of chert and carbonate rocks close to presumed hydrothermal vent sites (Figure 3f) [54]. However, proximal discordant vent complex mineralization (Figure 1b) is absent, or at least has not been preserved, in the Aberfeldy deposits.

The graphitic schist, which is the main host rock for the bedded mineralization, is cryptically enriched in barium (hosted in micas) in the vicinity of the mineralization [45,46,53]. In a lithogeochemical study of the Ben Eagach Schist in the central Scottish Highlands, Willan (1996) [46] found that the formation is regionally enriched in Bi, Sb, As, Mo, Ni, and Ba, which he attributed to hydrothermal point sources, but not enriched in trace metals, such as Co, Cr, V, Zn, Cd, and U, which are typically elevated in organic-rich black shales [55]. Moles (1985b) [45] found instances of hydrothermally silicified sediment (Figure 3h) in two contexts: stratigraphically below the mineralized beds at a few localities, and as lateral equivalents of the mineralized beds located distal from the main locus of hydrothermal activity.

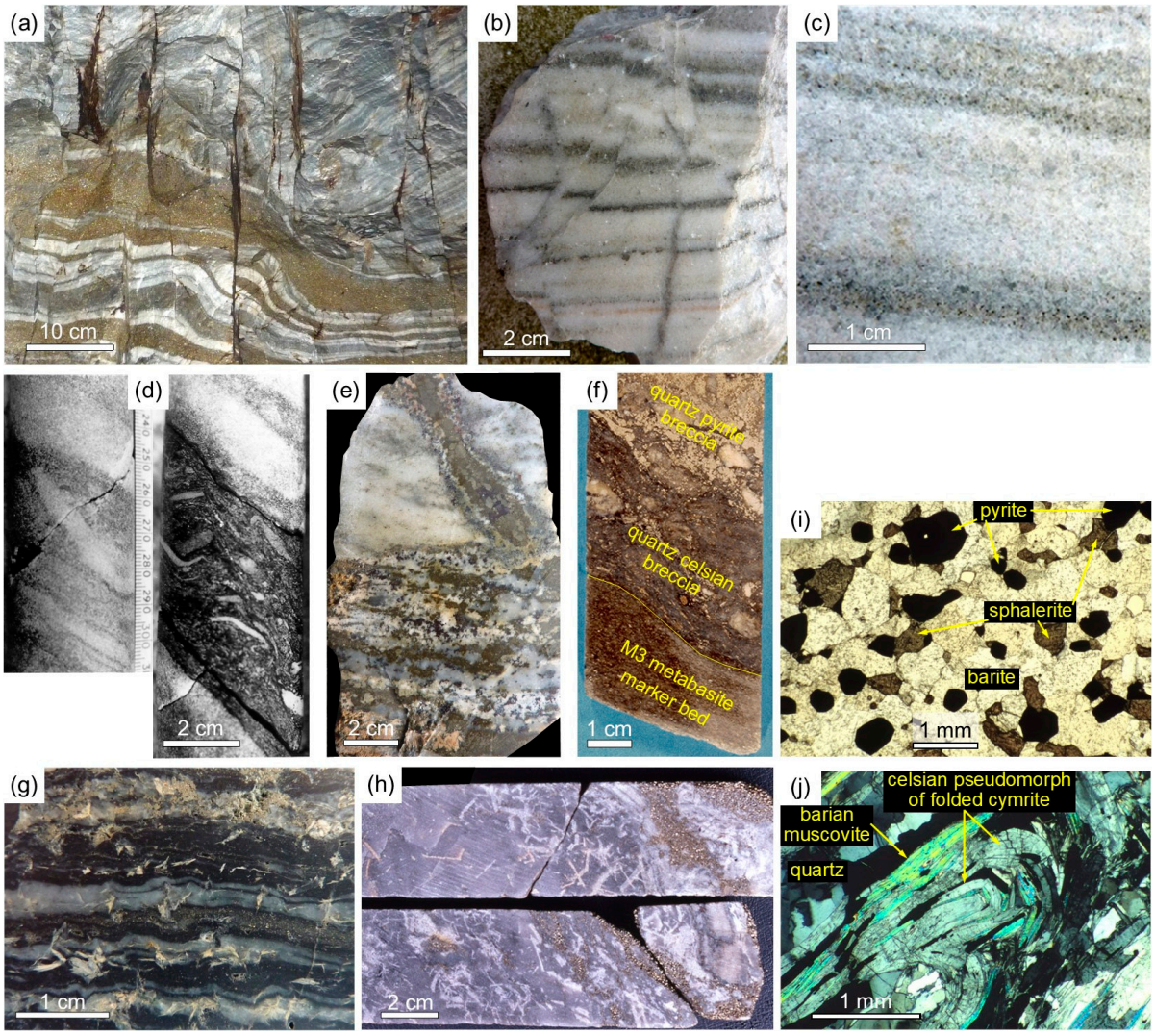


**Figure 3.** Textural features of Aberfeldy mineralization. Sample locations are shown on Figure 2d,e. (**a**) Basal contact of banded barite rock with granular pyrite rock containing folded beds of barite and celsian chert, Foss Mine. (**b**) Foss Mine banded barite rock with annealed fractures. (**c**) Closeup of typical Foss Mine barite rock cut perpendicular to banding. Light bands are pure granoblastic barite, while darker bands contain pyrite, sphalerite, carbonates, quartz, and barium silicates. (**d**) Conglomeratic barite rock in drillcore from Frenich Burn, Foss East (correct way up). Left: Dresser Minerals DH104. Right: IGS BH1. (**e**) Foss Open Pits sample (original way up not known) of quartz-sulfide-carbonate rock (lower half in photo) and barite rock intersected by a 2 cm-wide vein of sulfides. The sulfides comprise pyrrhotite, pyrite, sphalerite, and galena. (**f**) Cut drillcore (correct way up) from Foss East DH705, showing the metabasite marker bed immediately underlying the M3 mineralized bed, here comprising breccia-textured, celsian-, and pyrite-rich lithologies. (**g**) Laminated chert representing silicified sediment, containing fine and coarse pyrite and lenticular/wispy aggregates of Ba-K-Na feldspar that cross-cut bedding. Sample G114 from a distal outcrop of the M3 mineralized bed north of Foss Mine. (**h**) Cut drillcore from Dresser Minerals drillhole CM5, Duntanlich orebody, comprising pyritic chert (dark grey) containing tabular-shaped calcite aggregates (lighter color), which appear to be pseudomorphs of 1–2 cm sulfate crystals that grew in random orientations before lithification. (**i**) Photomicrograph (in plane polarized light) of granoblastic-textured sulfidic barite rock. (**j**) Micro-folded cymrite-muscovite-quartz schist (crossed polarized light) in which, following deformation, celsian has pseudomorphed foliated cymrite [53]. Foss West sample 429-15.

### *2.3. Metamorphic Alteration*

In the mid-Ordovician Grampian Orogeny, some 120–130 Ma after deposition, the sedimentary beds were tilted and distorted by several phases of folding and faulting, and subjected to medium-grade, amphibolite facies regional metamorphism [38,43,45]. Al-though rock textures and structure have been strongly modified, there is no evidence that substantial chemical change occurred within the mineralization during metamorphism. Previous studies [40,48,56,57] agree that the current mineralogy of barite, sulfides, carbonates, iron and titanium oxides, and barium aluminosilicates probably reflects the primary mineralogy of the chemical sediment, as this assemblage is typical of non-metamorphosed SEDEX/CD-type barite–base metal deposits globally. The barium aluminosilicates are predominantly celsian, with lesser amounts of 'hyalophane' (Ba-K-Na feldspar) and cymrite. These are considered to have formed through largely isochemical processes from hydrated barium aluminosilicate precursors [53].

Within the host metasediments, sulfur-phase chemistry has been modified during metamorphism through replacement of diagenetic pyrite by pyrrhotite [58] (often partially retrograde altered to pyrite), and the iron content of sphalerite has equilibrated with associated iron sulfides [45,56]. In contrast, sphalerite in the stratiform mineralization exhibits a wide range of compositions, interpreted by Moles (1983) [56] as of 'primary' exhalative origin (discussed further below).

To test for the presence of barium carbonates, Coats et al. (1980) [39] used staining solutions on carbonate-rich mineralized beds in drillcore from IGS BH3 in Foss and BH4 on Ben Eagach (Figure 2d) and reported no positive result. However, subsequent petrographic studies using cathodoluminescence [45] found trace amounts of the barium carbonates barytocalcite, norsethite, and witherite in 6 thin sections from Ben Eagach BH4 and in 15 samples from the Foss deposit. The barium carbonates are preserved as small (tens of micron diameter) inclusions within millimetric crystals of pyrite and other minerals. Cathodoluminescence also revealed complex zonation and retrograde/post-metamorphic crystallization histories in (non-barian) carbonates in mineralized rocks and in some metasediments. Moles (1985a,b) [45,59] determined carbonate Mg and Fe contents for application of the calcite–dolomite geothermometer and concluded that calcite–dolomite equilibration occurred at regional metamorphic temperatures in the range of 450 to 550 °C. As discussed later, the C and O isotope composition of carbonates has also been altered during metamorphism and, consequently, does not inform on pre-metamorphic processes in the mineralization and host rocks.

In regionally metamorphosed terrains, it is important to establish that stable isotope ratios have been preserved through metamorphism, using evidence such as significant isotopic variations on a millimeter scale within individual samples and in decimeter to meter scales in stratigraphic profiles. Several studies [28–30] have demonstrated preservation of sub-millimeter-scale sulfur isotope heterogeneity through amphibolite-grade metamorphism in rocks that lack evidence of intense fluid–rock interactions or of sulfur mobilization during metamorphism. Previous sulfur isotope studies of the Aberfeldy mineralization and host rocks have used conventional bulk sample analysis methods, whereas in the current study, we also used laser ablation to analyze individual, millimetric crystals in order to establish if isotopic heterogeneity on this scale is preserved.

### *2.4. Stable Isotope Compositions of Aberfeldy Deposit Barite, Sulfides, and Oxides*

The sulfur isotopic composition of Aberfeldy barite and sulfides has been studied extensively [52,54,57]. Willan and Coleman's 1983 study [57] included $\delta^{34}S$ analyses of 20 barite and 56 sulfide samples from surface and shallow borehole samples. Hall et al. (1991) [54] presented $\delta^{18}O$ and $\delta^{34}S$ analyses of barite from the Foss Open Pits. Moles et al. (2015) [52] presented further analyses of samples from the Foss deposit and the first isotopic analyses of samples from the Duntanlich orebody, totaling 88 analyses of barite $\delta^{34}S$. They demonstrated that $\delta^{34}S$ values of +36.5 ± 1.5‰ are typical of the barite beds (Figure 4) regardless of the stratigraphic position within individual beds or across the geographical

and stratigraphic extent of the mineralization. Although some profiles appear to show stratigraphic trends of increasing or decreasing $\delta^{34}S$ values, these variations are small (1‰–2‰) in the central parts of the barite beds, and do not support the preliminary findings of systematic $\delta^{34}S$ variation reported by Willan and Coleman (1983) [57] that were mainly due to pyrite impurities in their barite samples. However, Moles et al. (2015) [52] found that within approximately 1 m of the upper and lower boundaries of barite beds, both atypically low (+32 to +35‰) and atypically high (+37 to +41‰) $\delta^{34}S$ values are present, varying over distances of centimeters to tens of centimeters (Figure 4a). The DH104 profile through four stacked barite beds in Foss East shows high $\delta^{34}S$ values at bed margins, increasing up to 7‰ relative to the central part. Other profiles show both positive and negative couplets or triplets at the top and bottom margins. In Foss West DH424, a deeper intersection of the stacked barite beds M5 and M7 (Figure 4a), zig-zag isotopic excursions were found through an interval of >1 m at the base of M5 and over a thinner interval of ~0.2 m at the top of M7, but not between the M5 and M7 stacked beds.

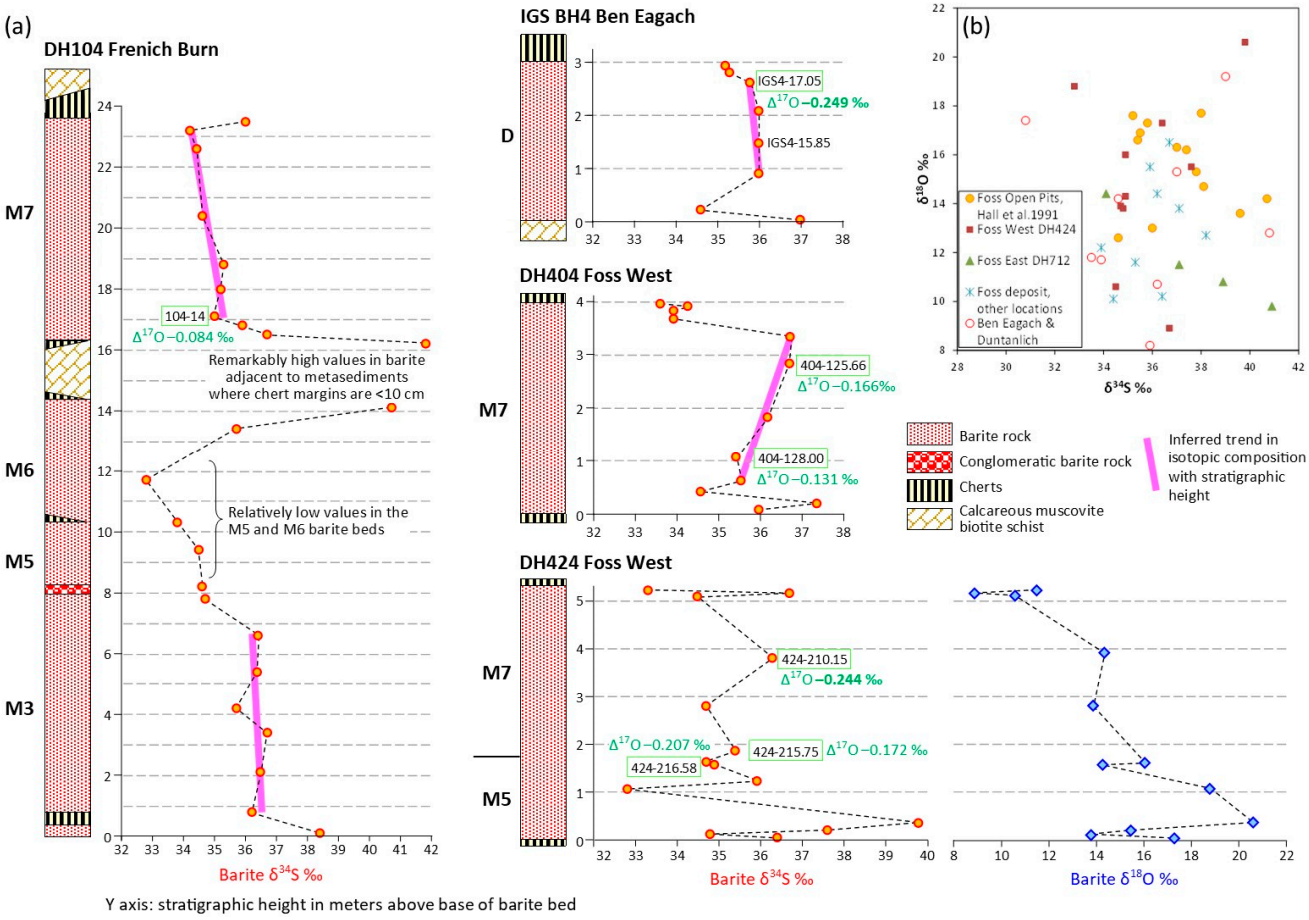


**Figure 4.** (**a**) Stratigraphic profiles of barite $\delta^{34}S$ and (for the DH424 profile) barite $\delta^{18}O$ in drillhole intersections of Aberfeldy barite beds (located in Figure 2d,e) using data reported by Moles et al. (2015) [52]. Numbers/letters adjacent to profiles are the mineralized bed label: D = Duntanlich deposit; M1 to M7 = Foss deposit (explained in Section 4.1). The central parts of most barite beds have relatively constant isotope ratios, whereas bed margins show isotopic perturbations. Labeled samples in green boxes were analyzed (this study) for $\Delta^{17}O$, with the result alongside (explained in later sections). (**b**) Cross-plot of $\delta^{34}S$ against $\delta^{18}O$ in barite samples analyzed for both isotopes, showing no overall correlation [52,54].

Considering the pronounced variations in barite $\delta^{34}S$ values in the DH424 profile, the samples were also analyzed for $\delta^{18}O$. Barite $\delta^{18}O$ shows similar positive and negative trends to $\delta^{34}S$ in the basal margin, whereas at the top of the M7, barite $\delta^{18}O$ and $\delta^{34}S$ show

opposing trends. Similar opposing trends in $\delta^{18}O$ and $\delta^{34}S$ were found [52] at the top of the M7 barite bed in Foss East DH712 (data in [52]).

$\delta^{18}O$ and $\delta^{34}S$ analyses of barite samples from a wide geographical and stratigraphical range within the Aberfeldy deposits, reported by Moles et al. (2015) [52], show no overall association on an isotope cross-plot (Figure 4b). This is contrary to a previous finding by Hall et al. (1991) [54] of a negative correlation between $\delta^{18}O$ and $\delta^{34}S$ in barite, based on a small number of samples from a geographically restricted area, namely the Foss Open Pits. However, samples from Foss East DH712 [52] do show a negative trend on the cross-plot (Figure 4b).

Hall et al. (1991) [54] reported magnetite $\delta^{18}O$ values of 7.1‰–7.6‰ in four samples of magnetite-bearing barite rock, and quartz $\delta^{18}O$ values of 11.0‰–19.5‰ in six samples of chert and quartz-barite rock from the Foss Mine Open Pits. Quartz in chert samples had lower values (11.0‰–13.4‰) than quartz in barite and quartz-dolomite rock samples (18.0‰–19.5‰). Dolomite $\delta^{18}O$ and quartz $\delta^{18}O$ values were identical in the quartz-dolomite rock. The authors noted that their quartz $\delta^{18}O$ values fell within the range +11.2 to +14.5‰ recorded by Fisk (1986) [60] for quartz from quartz–celsian rock and "cherty quartzites" (possibly clastic in origin) from the Aberfeldy deposits. Although few in number, these analyses hint at the presence of spatial variability in oxygen isotope ratios. Hall et al. (1991) [54] attributed the difference in oxygen isotope composition of quartz in chert and in barite rock to different temperatures during precipitation from the hydrothermal fluids, invoking relatively higher temperatures for chert precipitation. This seems counterintuitive, as chert is commonly the distal equivalent of the proximal barite beds.

Based on analyses of four samples of barite rock from the Foss Open Pits, Hall et al. (1991) [54] derived initial $^{87}Sr/^{86}Sr$ ratios in the range 0.7134–0.7150. These values are far removed from contemporaneous seawater, which would have been in the range 0.707–0.709 [61]. Hall et al. (1991) interpreted the relatively high $^{87}Sr/^{86}Sr$ values of Aberfeldy barite as due to radiogenic Sr (and Ba) being leached from the feldspathic basement at depth by the ore-forming hydrothermal fluids [43,49,62]. As noted by Hall et al. (1991) [54], this is consistent with a mean initial $^{87}Sr/^{86}Sr$ ratio of $0.715 \pm 0.007$ ($1\sigma$) for the Dalradian rocks that stratigraphically underlie the Ben Eagach Schist.

For the current study, a number of the barite separates previously analyzed for $\delta^{18}O$ and $\delta^{34}S$ [52] were analyzed for triple-oxygen isotopes (Figure 4a). It is useful here to explain the purpose of measuring the triple-oxygen isotope $\Delta^{17}O$ compositions. In the Earth's atmosphere, oxygen isotope mass-independent fractionation (O-MIF) occurs because of the continuous photochemical breakdown and recombination of oxygen ($O_2$) and ozone ($O_3$) in the ozone layer during the 'Chapman reactions' [63]. The triple-oxygen isotope $\Delta^{17}O$ signal is altered during these reactions, as $^{17}O$ is preferentially incorporated into $O_3$. As a result, $O_3$ inherits a positive $\Delta^{17}O$ value and $O_2$ a negative $\Delta^{17}O$ value [63]. The resulting magnitude of the $\Delta^{17}O$ value in $O_2$ also depends on the concentration of $O_2$ and carbon dioxide ($CO_2$) present: the higher the $CO_2$ concentration, the more negative the $\Delta^{17}O$ in $O_2$ can be driven as a result of increased molecular collisions and, therefore, more $^{17}O$ enrichment of $O_3$ [64]. The $\Delta^{17}O$ value of tropospheric $O_2$ is a function of this downwardly mixing stratospheric value ($\Delta^{17}O < 0$), as well as the proportion of the tropospheric $O_2$ reservoir that derives from gross primary productivity ($\Delta^{17}O = 0$) [36]. Marine sulfate ions incorporate atmosphere-derived $O_2$, and sulfate minerals precipitated from seawater can, therefore, preserve a record of atmospheric chemistry at the time of sulfate formation, provided that subsequent processes do not alter this signal. Many studies have shown that at any given point in Earth's history, the $\Delta^{17}O$ measured from sedimentary sulfates can be highly variable within a succession. Consequently, usually only the most negative $\Delta^{17}O$ value measured is taken as representative of oceanic and atmospheric compositions [36].

## 3. Materials and Methods

### *3.1. Drillcore Logging and Sampling*

Mineralized intervals intersected in all Foss and Duntanlich deposit drillholes were logged, recording lithologies and bedding orientations to enable graphical construction of true vertical distance profiles. Care was taken to identify, and compensate for, fold and fault repetitions that were encountered in some intersections. Representative drillcore obtained by Dresser Minerals from the Foss and Duntanlich deposits, together with samples analyzed in this study, are stored at the British Geological Survey's National Geoscience Repository (NGR) at Keyworth, England.

The majority of samples used in the study are from un-weathered drillcore, with some Foss deposit samples from outcrop. Samples from the British Geological Survey (formerly the Institute of Geological Sciences, IGS) Mineral Reconnaissance Programme boreholes (BH1–BH11) are referred to here by 4-digit numbers, e.g., 3915, corresponding to the sample identification scheme used by Coats et al. (1981) [40]. Samples from Dresser Minerals drillholes (coded DH, BE, and CM) incorporate the drillhole 3-digit number, e.g., 705-xx, according to the scheme used by Moles (1985b) [45].

### *3.2. Mineral Chemistry*

Moles (1985b) [45] undertook a detailed study of the petrography and mineral chemistry of a wide range of lithologies from the Foss deposit using outcrop and drillcore samples. Barite and sphalerite compositions reported here were determined by wavelength-dispersive electron microprobe analyses (WDS-EMPA) at University of Edinburgh, UK.

For the current study, trace element compositions of approximately 30 pyrite crystals from each of 10 samples, representative of proximal to distal mineralization in the Foss and Duntanlich deposits, were determined using laser ablation inductively coupled plasma mass spectrometry (LA-ICP-MS) by Claire Geel at University College Dublin, Ireland. The equipment was a Teledyne Photon Machines Analyte G2 193 nm excimer Ar-F laser with a HelEx II active 2-volume ablation cell attached to a Thermo Fisher Scientific iCAP-Qc quadrupole mass spectrometer. Laser spot size was 20 μm. Standards used were MASS1 [65], MUL-ZnS-1 [66], and the quality-control standard UQAC-FeS-1 [67]. Data reduction was undertaken in Iolite 4.19 using the 'TraceElements' data reduction scheme [68]. Concentrations were calculated using the internal standardization method [69], and iron was used as the internal standard, assuming a stoichiometric concentration of Fe = 46.55 wt%.

The barium carbonates described here are tiny crystals (usually <20 μm) encapsulated within pyrite and occasionally other minerals. They were initially found in polished blocks and thin sections by cold-source optical cathodoluminescence (CL) low-magnification microscopy, which revealed distinctive luminescence colors in the inclusions. The intensity and color of CL in carbonates is sensitive to small variations in composition, with $Mn^{2+}$ as the main activator, whereas $Fe^{2+}$ quenches the luminescence. Chemical compositions of ca. 50 inclusions of the barium carbonates were determined by WDS-EMPA at the University of Edinburgh [45]. Additional semi-quantitative energy-dispersive (EDAX) analyses were obtained using SEM facilities at the University of Brighton.

### *3.3. Stable Isotope Analysis*

Both conventional (bulk sample) and laser ablation (in situ) methods were employed at the Scottish Universities Environmental Research Centre (SUERC) for isotopic analyses of sulfur-bearing mineral phases. For conventional analysis, polymineralic rock samples approximately 2 $cm^3$ in volume were disaggregated and sieved, and pure mineral separates were obtained by using heavy liquid and magnetic separation techniques. Monomineralic grains in the size range 125–250 μm were hand-picked, and the purity of each sample was confirmed by binocular microscopy. $SO_2$ gas was produced from sulfides and sulfates following established methods [70,71] and analyzed on multi-collector mass spectrometers. The sulfate–oxygen extraction procedure used was that described by Hall et al. (1991) [54].

Laser ablation under vacuum was used to obtain $SO_2$ for sulfur isotope analyses of individual pyrite crystals ~1 mm in diameter within polished blocks. Standard corrections were applied to raw data [72] and the results are reported in standard notation ($\delta^{18}O$ and $\delta^{34}S$) as per mil (‰) variation relative to, respectively, the Vienna Cañon Diablo Troilite (V-CDT) and Vienna Standard Mean Ocean Water (V-SMOW). Based on repeat analysis of internal and international standards (NBS 127, IAEA-S-3, and NBS 123), analytical uncertainty (1σ) was better than ±0.3‰ for $\delta^{34}S_{sulfide}$ and better than ±0.8‰ for both $\delta^{18}O_{barite}$ and $\delta^{34}S_{barite}$.

For $\Delta^{17}O$ isotopic analysis, selected 1–2 $cm^3$ samples of barite rock were disaggregated, sieved, and hand-picked under a binocular microscope to remove sulfides, silicates, and oxides. Barite separates were then purified to remove any soluble salts, carbonate, and occluded nitrate using a protocol [73] based on established purification techniques [36,74]. Purified barite samples were analyzed at Louisiana State University (LSU). The procedure for $\Delta^{17}O$ analysis by laser fluorination is described by Pettigrew et al. (2021) [73]. The $\delta^{17}O$ and $\delta^{18}O$ composition of purified liberated $O_2$ was measured on a dual-inlet MAT 253 isotope-ratio mass spectrometer (IRMS) using the formula:

$$\delta\ ^{1X}O = 1000 * [\ ((^{1X}O/^{16}O)_{sample}/(^{1X}O/^{16}O)_{SMOW}) - 1] \quad (1)$$

where 'Xx' can equal 7 or 8, as appropriate. All $\delta^{17}O$ and $\delta^{18}O$ values were calibrated relative to internal laboratory standards and V-SMOW, and the long-term analytical uncertainty was better than ±0.05‰ (1σ). $\Delta^{17}O$ values were calculated from $\delta^{17}O$ and $\delta^{18}O$ values using the formula:

$$\Delta^{17}O = 1000 * [\ln(1 + \delta^{17}O/1000) - (0.528 * \ln(1 + \delta^{18}O/1000))] \quad (2)$$

## 4. Results

### *4.1. Deposit Morphology*

Drillcore logging showed that the mineralization is characterized by discrete beds with sharp internal boundaries between lithologies (e.g., barite rock, chert, and carbonate ± sulfide rock) and sharp external boundaries with the enclosing metasediments. Mineralized beds (in the Foss deposit, numbered consecutively upwards from M1) are continuous often over distances of a kilometer or more (Figure 2d,e) and are concordant with stratigraphy, as demonstrated by the base-M3 metabasite marker bed found throughout the Foss deposit (Figures 2c and 3f) [45]. Indeed, this metabasite bed, typically 0.2–0.4 m thick, provides a useful guide to the location of distal equivalents of the M3 mineralized bed in areas of the deposit where the M3 horizon is represented by an inconspicuous thin bed of chert or of barium-enriched muscovite schist, e.g., deep intersection DH201 (Figure 5a), and in outcrops on the northern limb of the Creag na h-Iolaire Anticline (Figure 2e). This gives us confidence in deducing that each mineralized bed represents a time-equivalent horizon.

In Foss West, two mineralized beds outcrop near the stratigraphic top of the Ben Eagach Schist formation (Figure 2e). The uppermost (M5) is more extensive and was worked for barite in Foss Mine, whereas barite worked in the Open Pits belongs to both M3 and M5 beds. In Foss East, thick barite (up to 25 m true thickness) in the vicinity of the Frenich Burn comprises a composite bed of M3 to M7 inclusive, which splits at depth and along strike eastwards into discrete mineralized beds separated by wedges of metasediment (Figure 5a). Toward the eastern extremity of the Foss deposit, the same mineralized beds become widely separated within a package of sedimentary strata up to 100 m in thickness.

The Duntanlich mineralized bed, consisting of barite rock where currently mined, lies near the stratigraphic base of the Ben Eagach Schist formation (Figure 2d) and is absent, or not exposed, in the Foss deposit area. Conversely, the M3 mineralized bed and its underlying metabasite marker bed have not been found in the Ben Eagach–Duntanlich area, despite a comprehensive examination of drillcore. However, the closely spaced M5, M6, and M7 beds of the Foss deposit, which lie at the stratigraphic top of the Ben Eagach

Schist, may be correlated with chert and thin barite beds exposed on Creag an Fhithich (Figure 2d) investigated in IGS boreholes 5 to 7 [39,40].

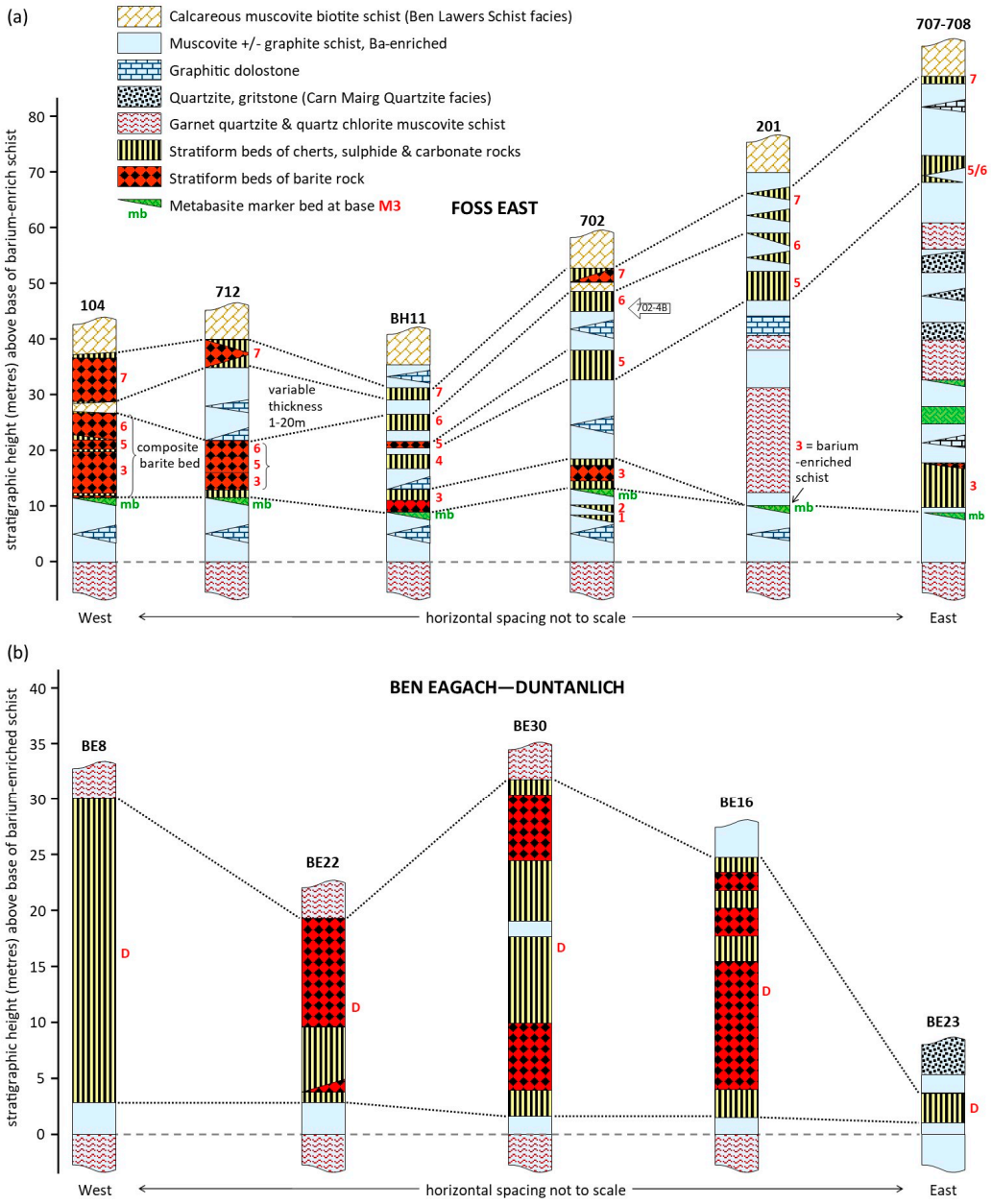


**Figure 5.** Representative stratigraphic (interpreted true thickness) sections of mineralized intervals in (**a**) Foss East and (**b**) Ben Eagach–Duntanlich, showing lateral continuity of mineralized beds with variations in facies and thickness in mineralization and host sediments. Red numbers/letters alongside profiles are the mineralized bed label (D; M1 to M7). Drillhole locations are labeled in Figure 2d,e.

Both the Foss and Ben Eagach–Duntanlich deposits exhibit areas with relatively thick (>2 m, up to ~20 m) barite beds and adjoining areas in which the barite is thinner (<2 m), or the mineralized bed is represented instead by sulfidic cherts and carbonate rocks (Figure 5). Sulfidic carbonate rocks occur widely, but in a limited number of areas these form decimeter-thick lenses, namely, in and around the sites of IGS BH3 in eastern Foss East and BH4 on Ben Eagach (Figure 2e). These locations, plus around IGS BH1 (Frenich Burn East) and BH2 (Foss Mine Open Pits) where the barite is unusually thick, are considered to be proximal to where the hydrothermal fluids entered the marine basin or sediment substrate.

### *4.2. Petrography: Sulfate Pseudomorphs and Barium Carbonate Inclusions*

#### 4.2.1. Sulfate Pseudomorphs

Close to the thicker mineralized beds, the graphitic schist is often more siliceous than usual and enriched in sulfides. This may be due to either impregnation by hydrothermal fluids or to later diagenetic alteration. Occasionally, footwall silicification has preserved the original finely laminated sediment, in which there is no evidence of bioturbation (Figures 3g and 6a–c), but there is evidence of millimetric gypsum and barite crystals that cut across and distort the laminae (Figures 3h and 6d–f). As discussed later, these are considered to be early diagenetic in origin, pre-dating lithification of the host sediment.

Porphyroblast-like structures of similar size, up to 1.5 cm, occur in bedded mineralization and mineralized sediments in all of the Aberfeldy deposits. The host rocks range from graphitic quartz-mica-feldspar schists to quartz-rich cherts and quartz-carbonate rocks within the stratiform mineralization. The structures now comprise aggregates of crystals of Ba-K-Na feldspar, quartz, calcite, or pyrite, suggesting pseudomorphic replacement of former crystals. They range in shape from lenticular and wispy (as in Figure 3h), to V- or Y-shaped intersecting blades (Figure 3i), to tabular with hourglass-shaped internal features (Figure 6). The tabular forms appear similar to experimentally produced pseudomorphs of celestite after gypsum [75], in which the replacement crystals are oriented perpendicular to the [010] surfaces. Some relict barite is present within the tabular pseudomorphs, as revealed by barite's distinctive luminescence under CL (Figure 6f). Morphologically, the lenticular and wispy structures resemble diagenetic anhydrite crystals, similar to those illustrated by Fu et al. (2002) [76]. The acute angle, V-, and Y-shaped bladed structures resemble the shapes of twinned gypsum crystals.

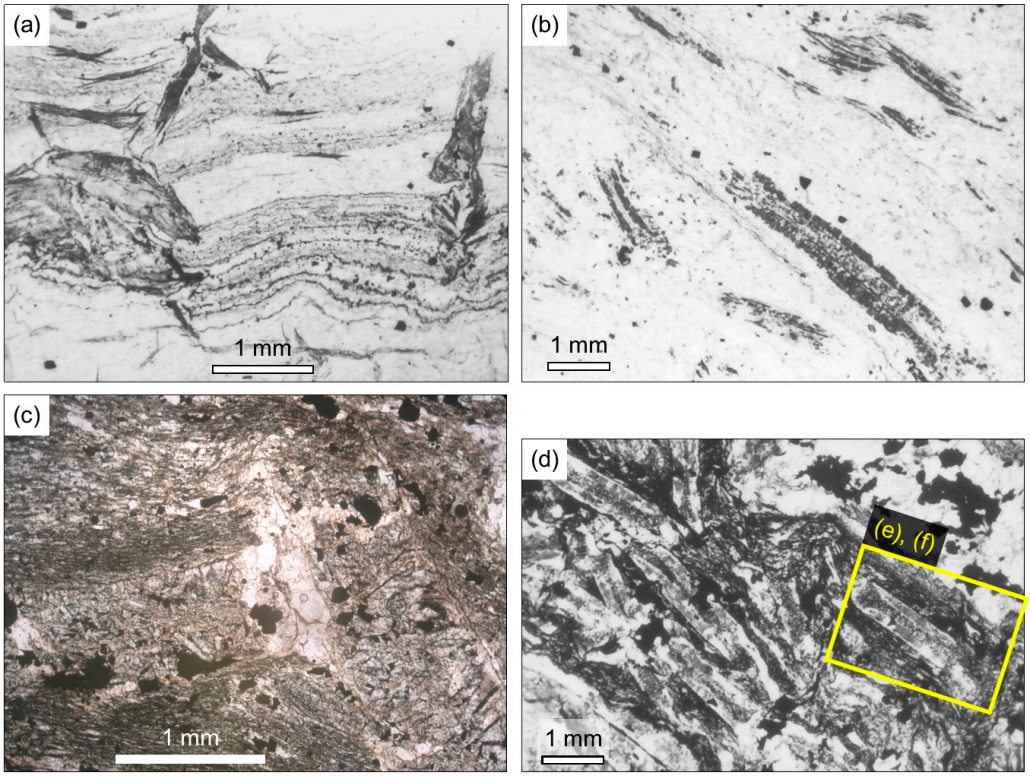


**Figure 6.** *Cont.*

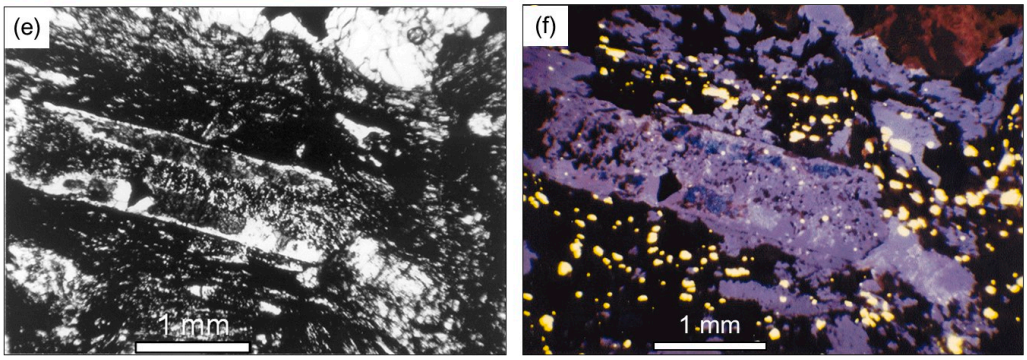


**Figure 6.** Photomicrographs of thin sections of Foss deposit mineralized metasediment samples (located in Figure 2e) containing tabular features comprising Ba-K-Na feldspar, quartz, barite, and pyrite, considered to be pseudomorphs of diagenetic sulfate crystals. (**a**) Quartz chert (PPL) finely laminated with pyrite and with lenticular, laminar, and wispy celsian structures. The celsian is weathered to a clouded mixture of barite, clay minerals, and quartz, but unaltered areas retain a foliated internal structure, which suggests that the celsian replaced cymrite. Sample G114, distal M3 on the northern limb of Creag na h-Iolaire Anticline, Foss West. (**b**) Foss West outcrop sample N81-80, plane polarized light. Quartz-mica-hyalophane chert with wispy and tabular hyalophane structures and disseminated sulfides (pyrite, sphalerite). The wispy/tabular structures are clouded in transmitted light due to fine barite and kaolinite inclusions. Some have an hourglass structure of clear hyalophane rich in fine-grained quartz and mica inclusions. (**c**) Foss East sample N81-43c from immediately below the M3 outcrop near IGS BH3 at Creag an Loch, PPL, showing relatively large tabular structures that displace bedding lamination and have internal crystal growth approximately perpendicular to the long axes. The mineralogy is predominantly hyalophane, with quartz, muscovite, and pyrite (opaque). (**d**) Foss West drillcore sample 09-06 from IGS BH9, PPL [45]. Graphitic muscovite hyalophane quartz chert showing tabular hyalophane structures, which have hourglass-shaped inclusions, at various angles to the bedding and D1/2 foliation. Opaque material comprises finely dispersed graphite and sulfides (pyrite, pyrrhotite, and ferroan sphalerite). Yellow rectangle shows area of enlarged views in (**e**,**f**). (**f**) Viewed under cathodoluminescence: bright yellow = apatite, dull red at upper right = quartz segregation, purple = Ba-K-Na feldspar, blue within tabular feature = barite, and pink within tabular feature = clay mineral (product of recent weathering). The non-luminescent matrix comprises muscovite, quartz, and graphite, with purple-luminescent Ba-K-Na feldspar that appears to occur as an authigenic cement phase.

The pseudomorphic structures appear to have survived metamorphism because they are hosted by quartz- and/or feldspar-rich rocks, which resisted orogenic deformation that caused rocks that are rich in micas and cymrite to develop a penetrative cleavage and micro-folding (Figure 3j). As discussed later, we suggest that the pseudomorphic structures represent diagenetic sulfate crystals and that, prior to metamorphism, such crystals were common within the sediments and within the silica- and carbonate-rich lithologies in the mineralized beds.

#### 4.2.2. Barium Carbonate Inclusions

The $BaCa(CO_3)_2$ polymorph barytocalcite occurs as bright-yellow to orange–red luminescent grains encapsulated by pyrite in carbonate- and sulfide-rich stratiform mineralization (Figure 7a,b). The yellow luminescence may be attributed to a longer wavelength emission activated by $Mn^{2+}$ ions within the relatively large $Ba^{2+}$ site, and variations in color and intensity reflect variations in the Mn and Fe contents. Where several grains of barytocalcite occur as discrete inclusions within a single pyrite crystal, their luminescence varies due to differences in the composition of each inclusion (Figure 7b). The encapsulated crystals are typically 10–100 µm in diameter, but can be as small as 1 µm, whereas the host pyrite crystals are typically 1–2 mm in diameter. In some samples, the pyrite contains dozens of small inclusions (Figure 7c).

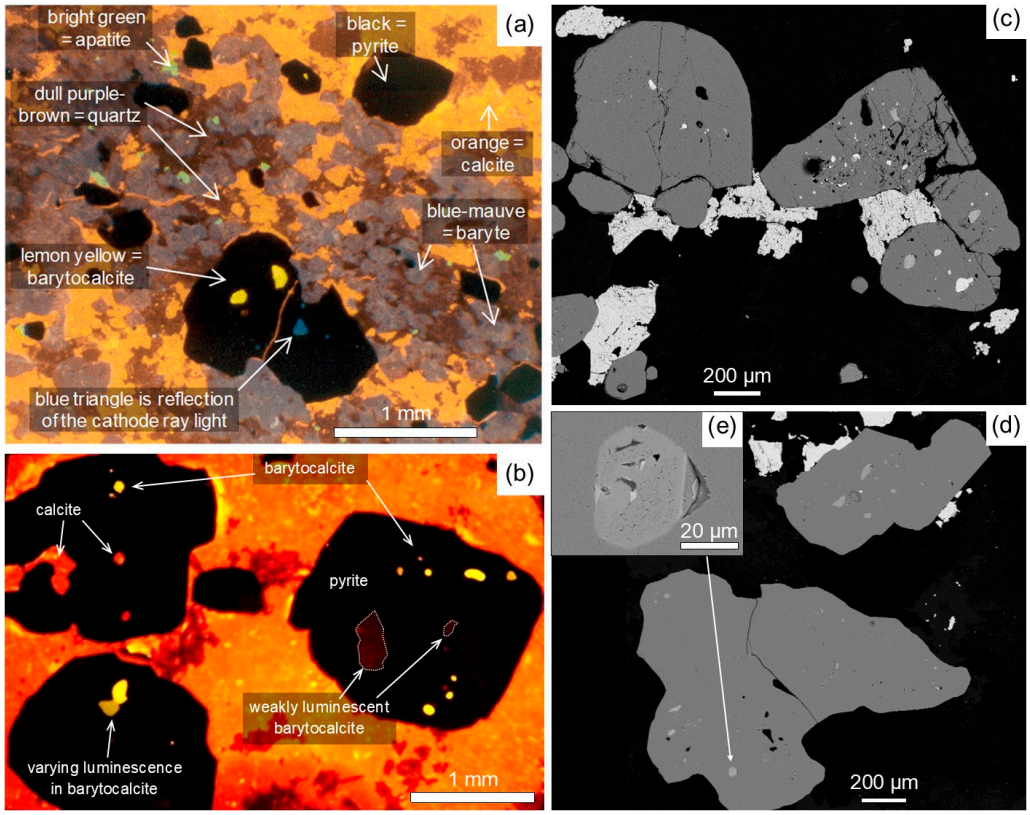


**Figure 7.** (**a**,**b**) Cathodoluminescence photomicrographs of pyrite-barite-calcite rocks showing inclusions of yellow-luminescent barytocalcite within pyrite (black, non-luminescent) and orange-luminescent matrix calcite. Annotations indicate luminescence colors of other minerals. (**a**) Sample 702-4B. (**b**) Sample from DH105 (Figure 2e). (**c**–**e**) Back-scattered electron images of barium carbonate inclusions (mid-grey) within pyrite crystals (darker grey) in matrices of barite (white), calcite, and quartz (both black). (**c**) Sample 702-4B. (**d**) Sample 505-15. (**e**) Sample 505-15 higher-magnification image of a composite inclusion comprising intergrown witherite, barytocalcite, and norsethite.

Barytocalcite occurs in samples of the bedded mineralization in which calcite and barite are the principal matrix phases. Norsethite, $BaMg(CO_3)_2$, occurs in a similar mode but tends to be found in rocks in which dolomite and barite are the principal matrix phases. In five samples, inclusions of both norsethite and barytocalcite were found in the same pyrite crystals. Unlike barytocalcite, norsethite does not have a distinctive luminescence, presumably because $Mn^{2+}$ ions are located in the $Mg^{2+}$ site (as in dolomite), and it is, therefore, likely that further occurrences of norsethite have been overlooked.

Witherite, $BaCO_3$, was positively identified in only 4 of approximately 160 Aberfeldy ore samples examined using electron microscopy. The samples are calcareous sulfidic barite rocks from the Foss deposit. Again, the occurrence is exclusively as small (tens of microns) inclusions within millimeter-sized crystals of pyrite, and witherite is absent from the external matrix, which comprises barite and calcite. In one sample, Foss East 702-4B (Figure 2e), witherite, barytocalcite, and norsethite all occur as inclusions in pyrite: these often occur together in the same host crystal, and in some cases, in mutual contact or intimately intergrown (Figure 7e).

### *4.3. Mineral Chemistry: Pyrite, Sphalerite, Barite, and Barium Carbonates*

#### 4.3.1. Pyrite Trace Element Composition

Preliminary LA-ICP-MS analyses of pyrite microchemistry (Figure 8) indicated that iron sulfide in the host metasediment is enriched in Co, Ni, Cu, and Pb, and poor in As, relative to pyrite in the stratiform mineralization. Samples selected as representing mineralization deposited proximal to hydrothermal vents, indicated by relatively thick

barite, had mostly low concentrations of Co, Ni, Cu, and Se. An exception is sample 712-41.40 (labeled C in Figure 8), a quartz-barite rock from the base of the relatively thick M3 barite bed at Frenich Burn (Figure 2e). The pyrite in this sample had the highest median Se concentration of the analyzed set, and Co and Ni values similar to pyrite in samples of distal mineralization.

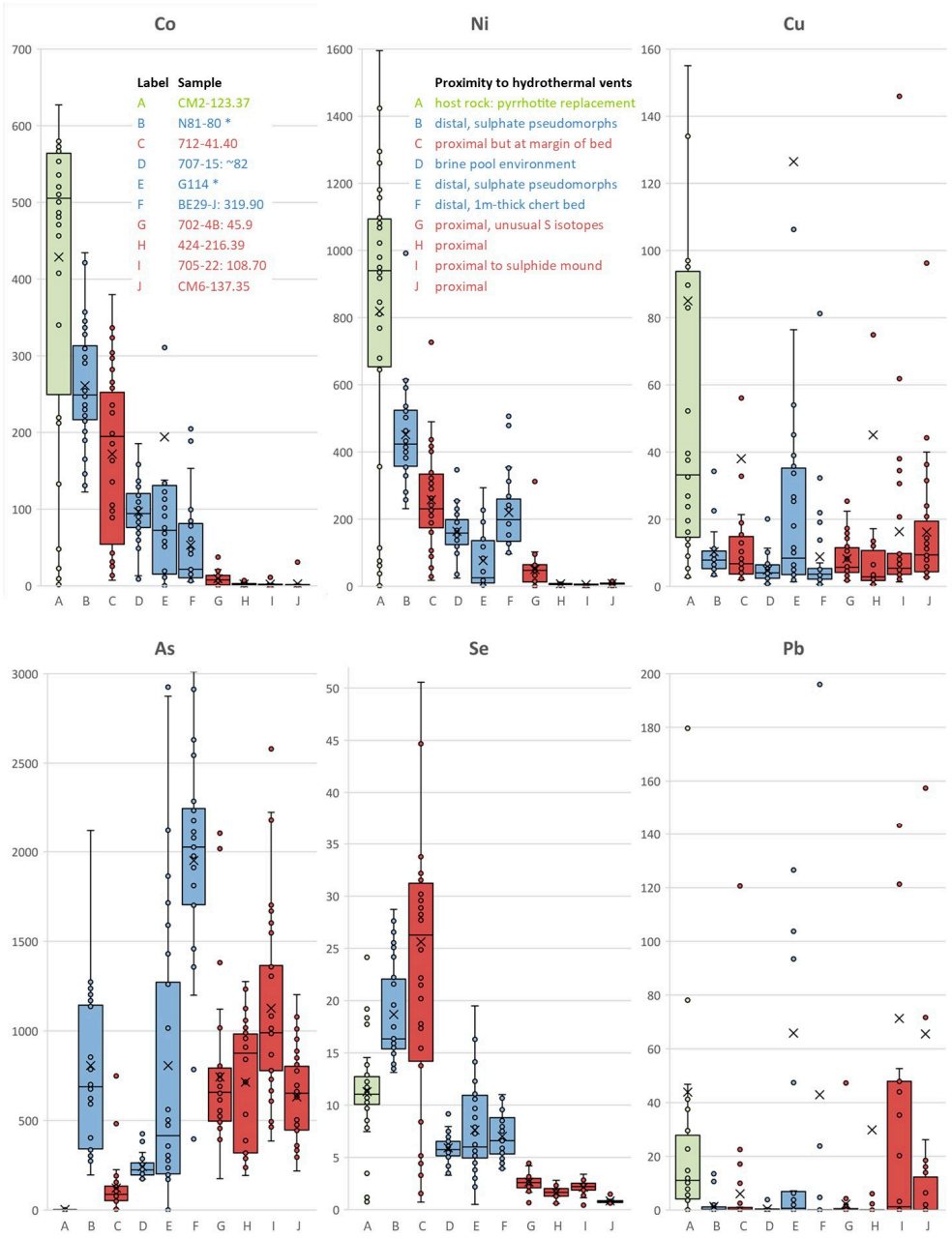


**Figure 8.** Box and whisker diagrams of pyrite microchemistry measured by LA-ICP-MS (analyses by Claire Geel, iCRAG). Vertical scales in ppm. Samples are arranged left-to-right in order of decreasing median cobalt values. * Indicates outcrop samples, the remainder are drillcore samples named by drillhole number (Figure 2d,e) and downhole depth, in meters. Sample A (box colored green) is pyrite replacement of pyrrhotite in host graphitic quartz-muscovite schist. The remaining samples are of Aberfeldy stratiform mineralization: B and D–F from comparatively distal locations (colored blue), C and G–J from proximal-to-vent locations (colored red). Vertical scale is cropped above the highest quartile value, and high outliers probably due to mineral inclusions are not shown. "o" Indicates individual analyses within the ranges shown. "×" Indicates the arithmetic average value for each sample/element.

Samples representing mineralization that is distal from the locus of hydrothermal vents, indicated by the dominance of chert, had pyrite trace element concentrations intermediate between the proximal samples and the host metasediment. Sample 707-15 (D in Figure 8) from the M3 distal chert-sulfide-sediment sequence at Creag an Loch (Figures 2e and 5) showed less compositional variation (i.e., a narrow interquartile range) than other samples.

Arsenic did not show a substantial difference between proximal and distal mineralization but showed a wide variation between samples, with a particularly low concentration in the aforementioned sample, 712-41.40, and a particularly high concentration in pyrite from a distal chert sample, BE-29J (labeled F in Figure 8), from BE29 east of the main Duntanlich deposit (Figure 2d).

#### 4.3.2. Sphalerite Composition

In an extensive study of sphalerite chemical compositions using thin-section petrography and EMPA, Moles (1983; 1985b) [45,56] distinguished between sphalerite that had retained 'primary' (pre-metamorphic) compositions and sphalerite with 'secondary' compositions altered during metamorphism by equilibration with pyrite-pyrrhotite (increasing the Fe content) and/or exsolution or diffusion processes (decreasing the Fe contents). Here, we consider only the sphalerite that represented primary compositions.

EMPA analyses of typically fine-grained sphalerite in Aberfeldy mineralization showed a wide range in minor element content, with 0–17 mol% FeS and 0–3 mol% MnS (these showed no overall correlation). Disseminated sphalerite crystals of contrasting composition frequently coexist within individual samples (Figure 9a). Individual crystals tend to be homogeneous, apart from coarse sphalerite crystals within carbonate rocks, which display zonation with low iron content toward the crystal rims. In sulfidic barite and chert rocks, sphalerite crystals are commonly encapsulated within larger (millimeter-size) pyrite crystals (Figure 9a). The presence of encapsulated sphalerites that are more variable in composition than sphalerite in the rock matrix (non-encapsulated) suggests homogenization of the matrix sphalerite due to crystal coalescence during grain coarsening. Mutual grain contacts between sphalerites of contrasting composition are rarely seen. However, in some samples, a bimodal distribution of sphalerite compositions is observed with the iron-poor fraction usually volumetrically predominant (Figure 9b). Primary iron-rich sphalerites are commonly finer grained (maximum diameter ~200 μm), more equant in shape, and more often encapsulated in pyrite than the iron-poor sphalerite occurring in the same rock (Figure 9a,b).

An extensive study was previously undertaken [45] of sphalerites occurring in the M3 mineralized bed in Foss East, which showed pronounced lateral facies' variations potentially related to the proximity of exhalative vents. The mol% FeS contents of >250 sphalerites, which are considered to have retained primary compositions, are plotted against stratigraphic height in seven intersections of this bed (Figure 9c). Within each profile, a wide range of sphalerite compositions was found, and a simple east to west pattern did not emerge. However, systematic variations in sphalerite iron content with stratigraphic height could be discerned in two profiles, namely, DH105 and DH708. Primary sphalerite showed a trend of decreasing iron content with height in DH708, the easternmost intersection of M3 in Foss East. Sphalerite with the lowest iron contents occurred in a short (~10 cm) barite interval near the top of the 7.5 m profile, but rose abruptly in the overlying cherts. A contrasting trend of increasing iron content in sphalerite with increasing stratigraphic height was seen in DH105, which intersects the thick, stacked barite beds in the vicinity of the Frenich Burn headwater (Figure 2e). Here, the composition of the Fe-rich sphalerite fraction in samples near the base of the profile (Figure 9c) was similar to the bulk of sphalerite occurring higher in the profile, where sulfides become subordinate to quartz and magnetite impurities in the barite rock.

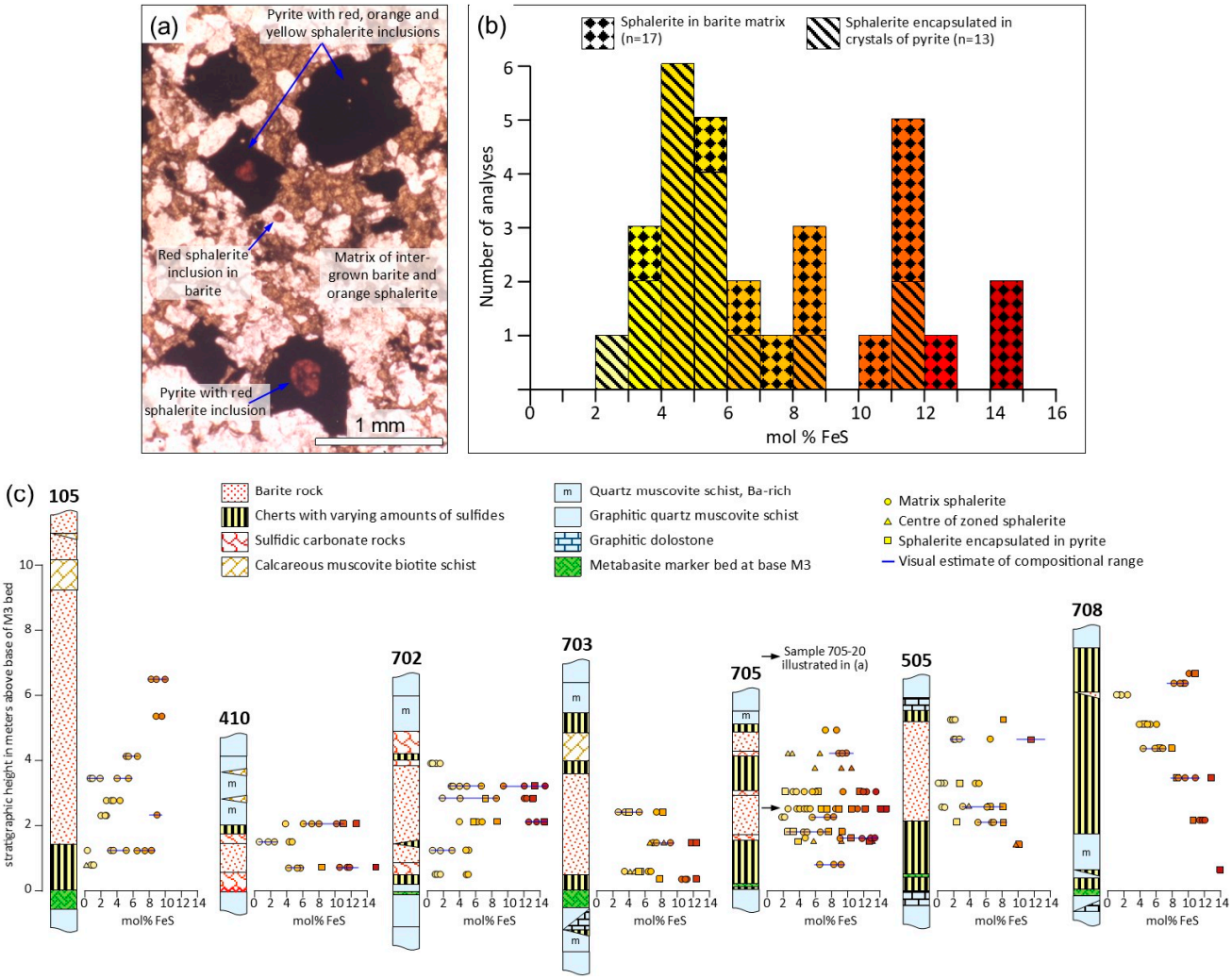


**Figure 9.** (**a**) Transmitted light photomicrograph of sulfidic barite rock sample 705-20 (Foss East DH705). (**b**) Histogram of Fe contents of 30 sphalerite crystals analyzed by EMPA in sample 705-20. (**c**) Vertical and lateral variation in sphalerite Fe contents in Foss East drillhole intersections of the M3 bed. Spacing of drillholes is not to scale: the total lateral extent is approximately 1 km (see Figure 2e). In (**b**,**c**), colors approximately match those of the sphalerites viewed in transmitted light in the thin sections. Figures adapted from Moles (1985b) [45].

#### 4.3.3. Barite Composition

Strontium and other elements often occur in minor amounts within barite, although most barite worldwide contains less than 7 mol% $SrSO_4$ [1]. Strontium is a minor but ubiquitous constituent of barite in the Aberfeldy deposits, ranging from <0.2 to ~2.0 mol% $SrSO_4$ (Figure 10a). Small grains of barite encapsulated within pyrite had widely differing Sr contents, even within a single thin section, ranging up to 6.2 mol% $SrSO_4$. Further unpublished EMPA analyses by Andy Tindle (personal communication, 2010) of drillcore samples of barite from Foss and Duntanlich found some evidence of systematic stratigraphic variation in strontium content. Two samples of typical sulfide-banded granoblastic barite rock from the M5 barite bed, intersected in Foss West DH424 at depths of 220.00 and 220.50 m, had notably higher strontium contents than other samples in this profile (Figure 10b). In the sample with the highest median strontium content (424-220.50), EMPA transects showed that marginal parts of clouded (inclusion-rich) barite crystals contained exceptionally high Sr, up to 10 mol% $SrSO_4$ (Figure 10c).

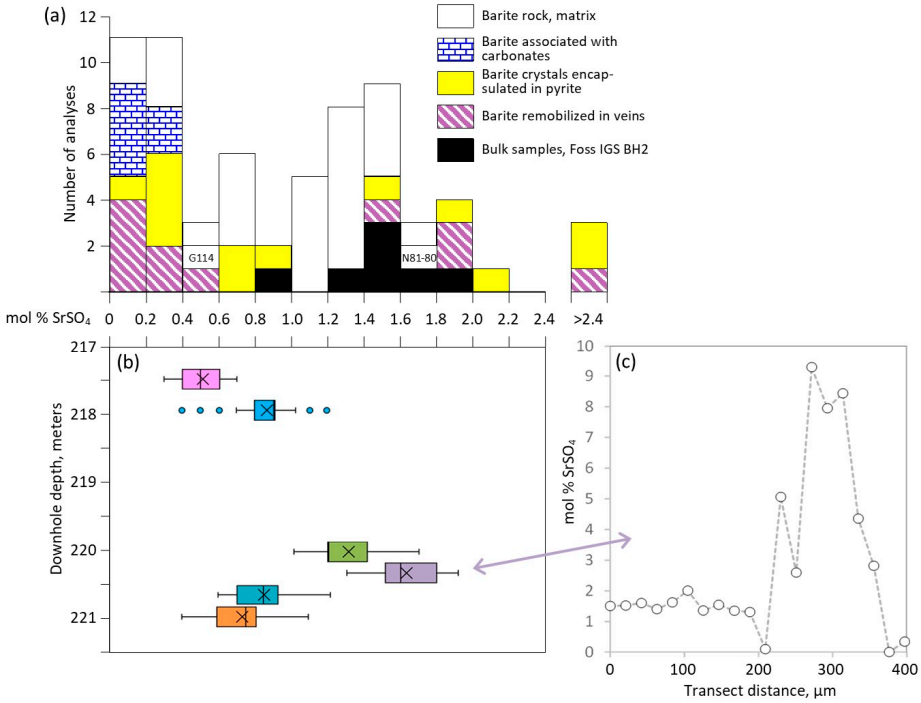


**Figure 10.** (**a**) Histogram of mol% $SrSO_4$ in 59 electron microprobe analyses (EMPA) by Moles (1985b) [45] of barite from a variety of lithologies at Foss. Those labeled G114 and N81-80 are analyses of barite in sulfate pseudomorphs in these specimens (Figure 2e). Also plotted are Sr contents of seven bulk samples of barite rock from IGS BH2 (Foss Open Pits area), recalculated to mol% $SrSO_4$ in pure barite, from data reported by Coats et al. (1981) [40]. (**b**) Stratigraphic profile (true vertical distance) of the M5 barite bed in Foss West drillhole DH424 with boxplots of mol% $SrSO_4$ in barite from EMPA of 10–25 crystals in each of 6 specimens ("×" indicates the arithmetic average values). (**c**) EMPA transect, 0.4 mm in length, across barite crystals in specimen 424-220.50, showing anomalously high $SrSO_4$ in one area. EMPA analyses in (**b**,**c**) were by Andy Tindle (personal communication, 2010).

#### 4.3.4. Barium Carbonate Compositions

Electron microprobe analyses of over 30 barytocalcite inclusions in 10 samples revealed considerable substitution by $MgCO_3$ and $SrCO_3$ (up to 7.3 and 6.0 mol%, respectively; Figure 11) and a corresponding variation in both $CaCO_3$ and $BaCO_3$ components (Table 2). The minor element composition of barytocalcite inclusions is typically similar to that of the matrix carbonate. For example, in a mineralized carbonate rock from Dresser Minerals borehole BE1 near Ben Eagach (Figure 2d), yellow-luminescent barytocalcite contained approximately 6 mol% $MnCO_3$ (Table 2), similar to the Mn content of the matrix calcite forming the bulk of the carbonate in this rock. Based solely on chemical composition, it is possible that some of the grains are of the polymorphs alstonite or paralstonite or the structurally distinct mineral species benstonite, $(Ba,Sr)_6(Ca,Mn)_6Mg(CO_3)_{13}$ [77]. However, these phases were not found in laser Raman analyses (unpublished data), and it is likely that the polymorph is indeed barytocalcite. A likely explanation for the compositional variation is the partial solid solution between barytocalcite and both dolomite and norsethite (Figure 11).

Twenty microprobe analyses, of which four are included in Table 2, revealed a considerable range of substitution for the $MgCO_3$ component by $FeCO_3$ (0–9.5 mol%) and $MnCO_3$ (0–12 mol%; Figure 11c). One inclusion of norsethite had 17.6 mol% $MnCO_3$, and this may be a distinct mineral species. More limited ranges were observed for $CaCO_3$ (0.4–4 mol%) and $SrCO_3$ (0–1.2 mol%). $SrCO_3$ appeared to substitute for $BaCO_3$, as the total of these components remained constant (Table 2). The three inclusions that fell outside the compositional fields of barytocalcite and norsethite in this diagram are likely to be calcite–norsethite and barytocalcite–norsethite mixtures. This was confirmed by back-scattered

electron images (Figure 7e) that showed crystals intergrown on a micron scale within the inclusions, which was smaller than the spatial resolution of the electron microprobe.

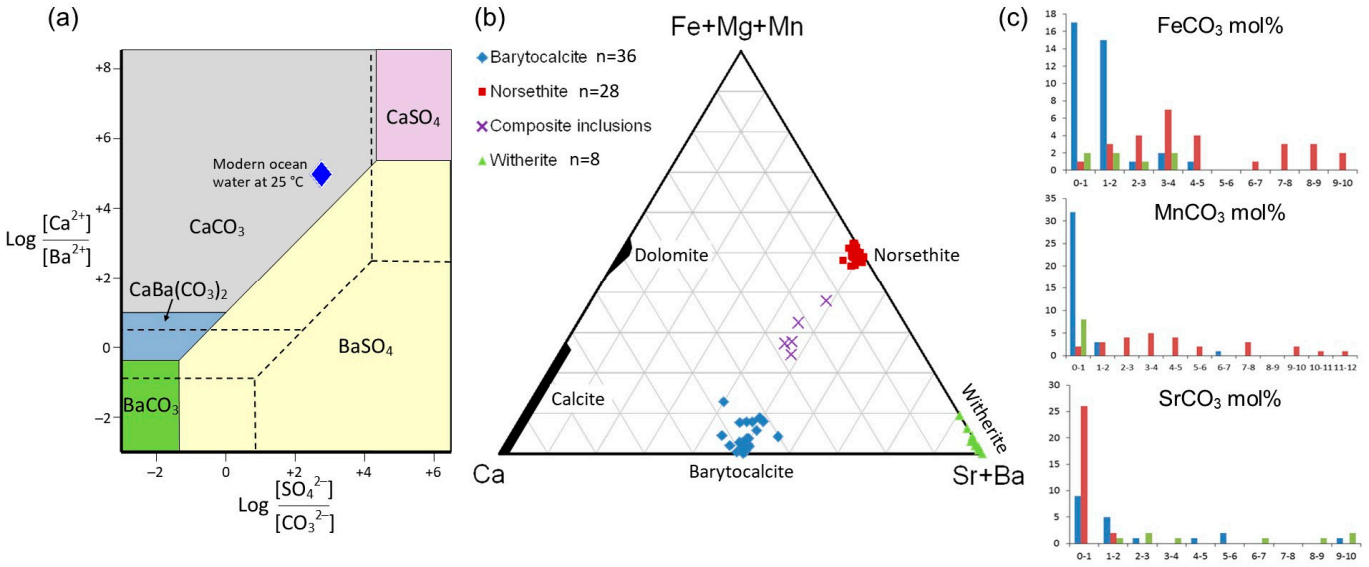


**Figure 11.** (**a**) Activity diagram of part of the system CaO–BaO–$H_2O$–$CO_2$–$SO_4$ at 1 atmospheric pressure, adapted from Maynard and Okita (1991) [78]. Solid lines show boundaries at 25 °C, while dashed lines show boundaries at 200 °C. A field for barytocalcite $CaBa(CO_3)_2$ has been inserted, although its upper boundary is speculative. (**b**) Ternary plot of molecular proportions of Ca, Fe + Mg + Mn, and Ba + Sr in Aberfeldy deposit carbonates. 'Composite inclusions' are micron-scale intergrowths of barytocalcite and norsethite. (**c**) Histograms of mol% $FeCO_3$, $MnCO_3$, and $SrCO_3$ in the analyzed barium carbonates, showing their compositional diversity. In (**b**,**c**), colors indicate the mineral species: Red, norsethite. Blue: barytocalcite. Green: witherite.

**Table 2.** Representative EMPA analyses of barium carbonates occurring as inclusions in Aberfeldy mineralization. Data from Moles (1985b) [45]. Samples 3915 and 3921 are from IGS BH4 (Coats et al., 1981) [40] (Figure 2d).

| | **Barytocalcite** | | | | **Norsethite** | | **Witherite** | |
|---|---|---|---|---|---|---|---|---|
| **Sample** | **BE1-138** | **703-8** | **3915** | **3921** | **408-28** | **702-9** | **410-29** | **701-19** |
| FeO wt% | 0.34 | 0.27 | 0.10 | 0.75 | 1.63 | 4.96 | 0.29 | 0.64 |
| MnO wt% | 3.09 | 0.21 | 0.79 | 4.75 | 2.10 | 0.76 | - | 0.02 |
| MgO wt% | 0.50 | 1.93 | 0.66 | 11.37 | 12.69 | 11.40 | 0.03 | 0.04 |
| CaO wt% | 16.13 | 17.62 | 15.73 | 1.01 | 0.59 | 0.20 | 0.08 | 0.17 |
| BaO wt% | 51.27 | 44.43 | 45.61 | 55.35 | 54.77 | 53.79 | 73.73 | 69.83 |
| SrO wt% | 0.80 | 4.24 | 9.55 | - | 0.04 | 0.91 | 1.50 | 5.25 |
| *total* | *72.13* | *68.70* | *72.44* | *73.23* | *71.82* | *72.02* | *75.63* | *75.95* |
| $FeCO_3$ mol% | 0.69 | 0.54 | 0.20 | 1.41 | 3.09 | 9.51 | 0.81 | 1.72 |
| $MnCO_3$ mol% | 6.31 | 0.42 | 1.59 | 9.07 | 4.03 | 1.48 | - | 0.05 |
| $MgCO_3$ mol% | 1.80 | 6.85 | 2.34 | 38.20 | 42.83 | 38.98 | 0.15 | 0.19 |
| $CaCO_3$ mol% | 41.67 | 44.93 | 40.13 | 2.44 | 1.43 | 0.49 | 0.28 | 0.58 |
| $BaCO_3$ mol% | 48.42 | 41.42 | 42.54 | 47.87 | 48.58 | 48.33 | 95.87 | 87.69 |
| $SrCO_3$ mol% | 1.12 | 5.85 | 13.19 | - | 0.05 | 1.21 | 2.89 | 9.76 |
| *total* | *100.00* | *100.00* | *100.00* | *100.00* | *100.00* | *100.00* | *100.00* | *100.00* |

Witherite contained about 3 mol% $SrCO_3$ in samples 3965 and 410-29, whereas in 701-19 and 702-4B, the witherite contained up to 10 mol% $SrCO_3$ (Table 2, Figure 11c). Ca, Mg, and Mn contents were low, and $FeCO_3$ varied from 0.6 to 4 mol%, although the higher values may be partly due to analytical interference from enclosing pyrite.

### *4.4. Stable Isotope Geochemistry*

#### 4.4.1. $\delta^{34}S$ Values in Samples with Either Sulfate Pseudomorphs or Barium Carbonates

Table 3 and Figure 12a–c present the results of new sulfide $\delta^{34}S$ analyses of samples of calcite-barite-sulfide mineralization containing barium carbonate inclusions, and of mineralized sediments containing sulfate pseudomorphs. In Figure 12a, the new results are compared with previous analyses of sulfides in the host metasediments ('Sed') and those in the stratiform mineralization ('Min'). Whereas the simple two-fold division proposed by Hall et al. (1991) [54] of lower $\delta^{34}S$ values in metasediment sulfides and higher values in mineralization sulfides is broadly true, it is apparent that $\delta^{34}S$ values varied widely in both lithological groups. A third category of mineralized sediments ('MinSed') are laminated chert-like rocks, rich in silica and/or Ba-K-Na feldspar, representing clastic sediment impregnated with mineral material derived from the hydrothermal solutions. The mineralized sediments showed a range of sulfide $\delta^{34}S$ values that overlapped the ranges of the other two categories. These samples include some containing sulfate pseudomorphs.

Barite and pyrite were separated from the carbonate-sulfide-barite rock sample 702-4B. in which pyrite crystals contained relatively abundant inclusions of barium carbonates (Figures 4a and 7a,c). In contrast to the typical granoblastic texture of barite rock (Figure 3i), in 702-4B, barite occurred as irregular areas within a calcite matrix (Figure 12d), which we consider to be evidence of retrograde metamorphic recrystallization. The barite had $\delta^{34}S$ values of 14‰–16‰. This is exceptionally low compared to normal barite rock at Aberfeldy, for which the range is 30‰–42‰, but it is comparable to the isotopic composition of sulfides in the metasediments (Figure 12a). Conversely, pyrite in sample 702-4B incorporated sulfur with exceptionally high $\delta^{34}S$ values of 29‰–32‰. This is outside the range of previously reported sulfides but overlaps the $\delta^{34}S$ range of Aberfeldy barite (Figure 12a). These results may indicate that in 702-4B, the barite-sulfur was derived from oxidation of pre-existing sulfide, and pyrite-sulfur from reduction of pre-existing sulfate, as discussed below.

**Table 3.** Sulfur isotope data ($\delta^{34}S$ values in ‰) from samples with barium carbonate inclusions (top) or sulfate pseudomorphs (bottom). 'MinSed' and 'Min' are abbreviations for mineralized sediment and stratiform mineralization, respectively. Included are barite $\delta^{34}S$ values for sample 702-4B (by conventional analysis).

| Sample, Location | Deposit | Lithology, Interpretation | Min/Sed | $\delta^{34}S$ Pyrite | $\delta^{34}S$ Barite | Analysis Type/Number |
|---|---|---|---|---|---|---|
| 702-4B, Frenich Burn | Foss East | Calcareous pyrite-quartz-barite rock with barium carbonate inclusions in pyrite | Min | 30.2–32.1 | 16.0 | Range in 5 pyrite laser analyses |
| 702-4B subsample B | " | As above, barite-rich subsample | " | 29.2–29.4 | 15.0–15.8 | Conventional analysis (duplicates) |
| 702-4B subsample C | " | As above, carbonate-rich subsample | " | 31.0–31.2 | 13.8–14.7 | Conventional analysis (duplicates) |
| 505-15, Creagan Loch | " | Calcareous pyrite-quartz-barite rock with barium carbonate inclusions in pyrite | Min | 21.1–26.8 | | Range in 6 pyrite laser analyses |
| BE01-138, Ben Eagach | Ben Eagach/Duntanlich | Pyritic calcite barite rock with barium carbonate inclusions in pyrite | Min | 28.0 | | Average, 2 pyrite analyses |

**Table 3.** *Cont.*

| Sample, Location | Deposit | Lithology, Interpretation | Min/Sed | $\delta^{34}$S Pyrite | $\delta^{34}$S Barite | Analysis Type/Number |
|---|---|---|---|---|---|---|
| BE 001, Ben Eagach barite quarry | Ben Eagach/Duntanlich | Quartzose chert with minor pyrite containing carbonate pseudomorphs of gypsum | MinSed | 27.8–28.3 | | Range in 2 pyrite laser analyses |
| 09-06, IGS BH9 | Foss West | Graphitic quartz Ba-K-feldspar schist with disseminated sulfides and barite pseudomorphs | MinSed | 17.7 | | Conventional analysis |
| N81-80, Creag an Chanaich | " | Quartz Ba-K-feldspar schist with disseminated sulfides and barite pseudomorphs | MinSed | 26.8–27.6 | | Range in 4 pyrite laser analyses |
| G114, north limb of anticline | " | Quartz pyrite rock and laminated chert with sulfate pseudomorphs, M3 bed distal from vent | MinSed | 28.9 | | Conventional analysis |
| G100, ~150m west of G114 | " | Laminated quartz-pyrite rock, M3 bed distal from vent | MinSed | 28.1 | | Conventional analysis |

Sample 505-15 is a laminated pyritic chert containing carbonates and minor barite (insufficient for isotopic analysis), again with abundant barium carbonates occurring as inclusions in pyrite (Figure 7d,e). Within an area of <2 $cm^2$, individual dispersed crystals of pyrite had $\delta^{34}$S values ($n$ = 6) ranging from 21.1‰ to 26.8‰ (Figure 12b). This wide range confirmed that sulfur isotope heterogeneity existed in the precursor sedimentary rock and, at least in some rocks, this small-scale heterogeneity has survived regional metamorphism.

Sample BE01-138 is a pyritic calcite-barite rock from Dresser Minerals drillhole BE1 (Figure 2d), in which coarse pyrite crystals contain inclusions of barytocalcite (Table 3). Laser analyses of a pyrite crystal in this sample yielded a $\delta^{34}$S value of 28.0‰. The same value was obtained for pyrite in the nearby sample BE 001, a quartzose chert with disseminated pyrite and pseudomorphs of gypsum, from exposures near IGS BH4 on Ben Eagach. Disseminated galena in BE 001 yielded a $\delta^{34}$S value of 29.0‰.

Pyrite was analyzed in five samples of cherty mineralized sediments ('MinSed' in Table 3) that have retained textural evidence of diagenetic sulfate crystals. Sample 09-06 from the IGS BH9 downhole depth 28.7 m is the bladed porphyroblastic-textured rock described by Fortey and Beddoe-Stephens (1982) [53] (Figure 6d–f). Minor pyrite occurs both within the barium feldspar 'porphyroblasts' and in the matrix. A conventional analysis of pyrite in this sample yielded a $\delta^{34}$S value of 17.7‰, which is typical of the Ben Eagach Schist. However, contrasting isotopic results were obtained for the texturally similar sample N81-80 collected at the surface from a stratigraphic position similar to 09-06 (Figure 2e). Laser analyses of individual pyrite crystals ($n$ = 4) in N81-80 yielded a $\delta^{34}$S range of 26.8 to 27.6‰, similar to a previous conventional analysis of 27.1‰ [45]. Willan and Coleman (1983) [57] reported a similarly $^{34}$S-rich pyrite (26.9‰) in a sample from a depth of 130 m in IGS BH8 (Creag an Fhithich; Figure 2d) [40] of 'graphitic celsian-bearing schist' with probable barite pseudomorphs. $\delta^{34}$S values of 28.1 and 28.9‰ were obtained by conventional analyses of pyrite in sulfidic chert samples G100 and G114 (distal M3 bed: Figure 2e), which contained sulfate pseudomorphs, as illustrated in Figures 3g and 6a. These $\delta^{34}$S values are at the upper end of the 'normal' range for Aberfeldy sulfides (Figure 12a).

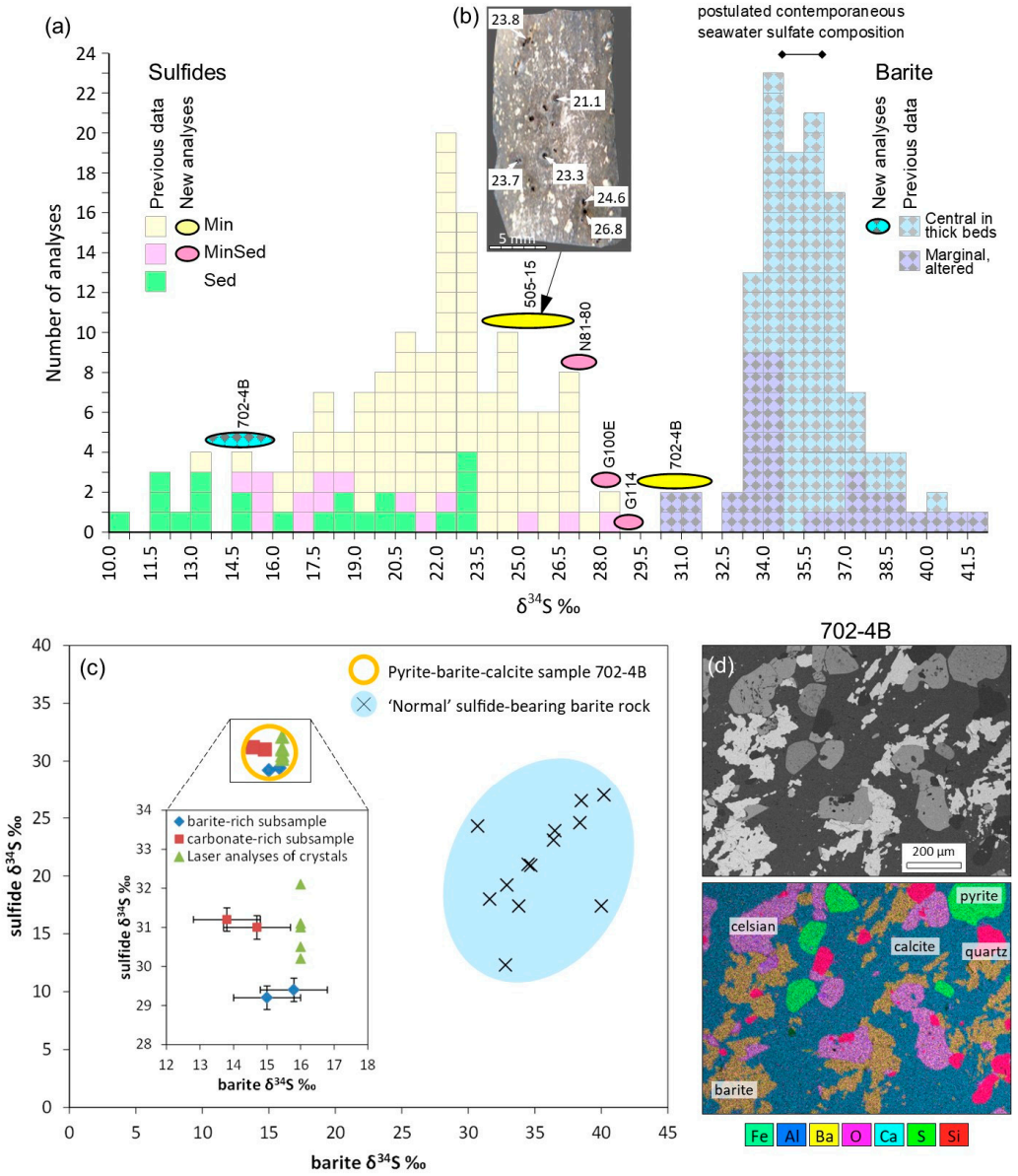


**Figure 12.** Sulfur isotope data for samples from the Aberfeldy deposits. (**a**) Histogram comparing new $\delta^{34}S$ results (ovals) with previously published values (squares) [52]. Barite indicated by diamond-pattern infill. For sulfides, the color infill is according to host lithology: Min, stratiform mineralization; MinSed, mineralized clastic sediments (mostly footwall adjacent to mineralization); Sed, (meta)-sedimentary. (**b**) Polished block of pyritic Ba-K-Na feldspar chert sample 505-15, showing pyrite crystals analyzed by laser ablation and the obtained $\delta^{34}S$ values in per mil. (**c**) Cross-plot of $\delta^{34}S$ values in barite and in coexisting sulfide in normal sulfide-bearing barite rock (blue oval encompasses the range), and in Foss East calcareous sulfidic barite sample 702-4B. Inset plot shows analyses of 702-4B subsamples of barite and pyrite, and laser analyses of individual pyrite crystals (within a 1 cm × 2 cm block) plotted against the bulk $\delta^{34}S$ of barite (16.0‰). Error bars show one standard deviation error based on repeat analyses of standards. (**d**) Back-scattered electron image (**top**) and EDS composite map (**bottom**) of a typical part of a polished section of sample 702-4B, showing the spongy intergrowth of calcite and barite (see also Figure 7a).

#### 4.4.2. Barite $\Delta^{17}O$

Six analyses of Foss deposit barite, sampled from a variety of locations and stratigraphic levels, and one from IGS BH4 on Ben Eagach, yielded $\Delta^{17}O$ values ranging from −0.084 to −0.249 (Table 4). Further analyses (unpublished data) of barite samples from IGS BH4 and the Duntanlich deposit yielded $\Delta^{17}O$ values less than −0.103‰. All samples had $\delta^{34}S$ values in the range 34.9‰–37.2‰, which is typical of barite in thicker beds (Figure 4a). Sampling was avoided from bed margins where post-depositional isotopic modification was evident, as discussed above.

**Table 4.** Barite samples analyzed for $\Delta^{17}O$ (see Figure 2 for drillhole locations), with information on their position within mineralized beds and $\Delta^{17}O$ values obtained in this study. $\delta^{34}S$ values in these samples were previously reported by Moles et al. (2015) [52].

| Deposit/Area | Drillhole Depth | Bed # | Height, m † | Position/Fe Mineral in Barite | $\delta^{34}S$‰ | $\Delta^{17}O$‰ |
|---|---|---|---|---|---|---|
| Ben Eagach | IGS BH4-17.05 | D | ~3.0 | Upper central in barite bed | 35.8 | −0.249 |
| Foss East | '104-14' 104-16.12 | 7 | 17.1 | Upper barite bed in thick stack | 35.0 | −0.084 |
| Foss West | 404-125.66 | 7 | 2.8 | Pyrite-bearing barite rock | 36.5 | −0.166 |
| " | 404-128.00 | 7 | 1.0 | Pyrite-bearing barite rock | 35.3 | −0.131 |
| " | 424-210.15 | 7 | 3.8 | Pyrite-bearing barite rock | 36.3 | −0.244 |
| " | 424-215.75 | 7 | 1.85 | Magnetite-bearing barite rock | 35.4 | −0.172 |
| " | 424-216.58 | 5 | 1.55 | Magnetite-bearing barite rock | 34.9 | −0.207 |

# Mineralized bed letter/number (see Figure 4 and Section 4.1). † Estimated vertical height, in meters, above the base of the mineralized bed.

In this dataset, the most negative $\Delta^{17}O$ was −0.249‰ in sample BH4-17.05 from Ben Eagach (Figure 2d). Similarly, low values of −0.244 and −0.207, respectively, were obtained for Foss West samples 424-210.15 from the M7 barite bed and 424-216.58 from the M5 barite bed (Figure 4a). Although the dataset is small, this similarity in the most negative values from three different barite beds suggests that the $\Delta^{17}O$ signal is not specific to a particular stratigraphic level but is a general feature of the Aberfeldy barite deposits.

#### 4.4.3. Carbonate $\delta^{13}C$ and $\delta^{18}O$

The isotopic composition of carbonates in the Foss deposit mineralization and metasediments was measured using outcrop and drillcore samples [45]. In nine samples, $\delta^{13}C$ ratios ranged from −5‰ to −12‰ and $\delta^{18}O$ ratios from +11‰ to +22‰ (Figure 13a). Indistinguishable isotopic compositions were obtained in carbonate samples of metasediments, of mineralization, and of metasomatically altered metabasite, suggesting that carbonate isotopic ratios had equilibrated with pervasive $CO_2$-bearing metamorphic fluids. One sample analyzed, of Ben Lawers Schist, yielded a lower $\delta^{13}C$ than the Ben Eagach Schist samples (Figure 13a). Weathered samples yielded higher $\delta^{18}O$ ratios (17‰–22‰) than fresh drillcore samples (range 11.6‰–13.6‰), a feature attributed to a late-metamorphic or geologically recent interaction with isotopically heavier meteoric waters.

Hall et al. (1991) [54] reported $\delta^{13}C$ and $\delta^{18}O$ ratios of −5.3‰ and +18.4‰, respectively (Figure 13a), for dolomite in a sample of banded quartz-dolomite rock from the Foss Mine Open Pits. Their result is similar to our values for weathered samples of calcareous metabasite (the M3 marker bed) and Ben Lawers Schist.

In the present study, we analyzed calcite in sample 702-4B from Foss East DH702 and obtained $\delta^{13}C$ and $\delta^{18}O$ ratios of −8.7‰ and +18.3‰, respectively (Figure 13a). The $\delta^{13}C$ ratio is typical of Ben Eagach Schist-hosted carbonate, and the $\delta^{18}O$ ratio is typical of weathered samples, suggesting that meteoric fluids interacted with this rock.

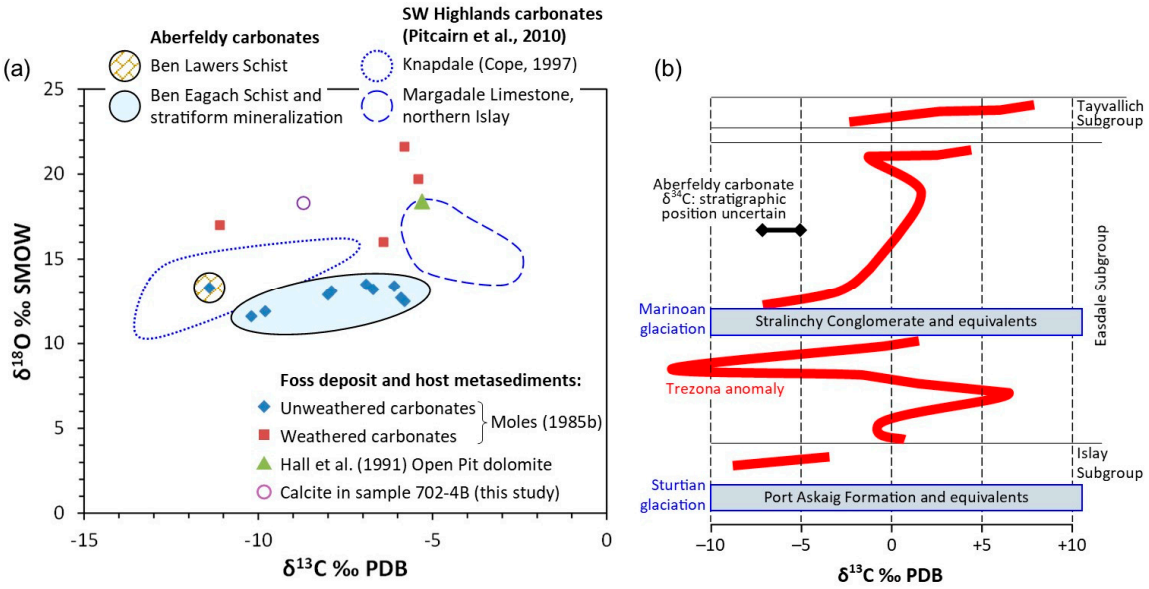


**Figure 13.** (**a**) Carbonate $\delta^{13}C$ and $\delta^{18}O$ isotope data (from [45,54] and this study) for samples from the Aberfeldy deposits compared with those for metamorphic-fluid–equilibrated carbonate metasediments in the Southwest Highlands of Scotland [79]. Also shown is the compositional field of calcite in samples from Knapdale of micro-veins of metamorphic origin [80]. (**b**) Comparison of Aberfeldy carbonate $\delta^{13}C$ range with the seawater-derived chemo-stratigraphic trends (red lines) of carbonate strata in the Argyll Group of the Dalradian Supergroup in the SW Highlands of Scotland, from Prave et al. (2009) [81].

## 5. Discussion

In presenting the results from a range of stratigraphical, mineralogical, and isotopic investigations, our objective was to undertake a critical evaluation of the contributions to the formation of the stratiform mineralization of seafloor precipitation (the SEDEX model) and of subsurface diagenetic replacement processes.

### *5.1. Spatial Variation in Facies and Thickness Proximal and Distal to Inferred Vent Sites*

A remarkable feature of the deposits is the pronounced lateral facies and thickness variations within mineralized beds (Figure 5), which is associated with facies and thickness variations in the host metasediments. This has been interpreted [44,45,52] to indicate that mineralization comprising predominantly barite and carbonate rocks precipitated in relatively shallow-water, oxic areas of the depositional basin, while synchronously, cherts and sulfides precipitated in deeper parts of the basin, where anoxic conditions prevailed at the sediment–water interface (Figure 14). Variations in the rates and types of sediment input are attributed to localized basinal down-warping and uplift associated with syn-sedimentary faulting, a feature commonly associated with SEDEX-type deposits [8]. This, together with stratification of oxygen levels in the seawater, is suggested to account for the lateral facies' variation in the mineralized beds.

In the central part of the Foss deposit (Frenich Burn East), vertical stacking of multiple barite beds and sedimentary reworking forming baritic conglomerates (Figures 3d and 5a) suggest a relatively high-energy shallow-water environment, in which the only sediments to survive reworking were precipitates of barite. Further east, in the vicinity of IGS BH3 and Dresser Minerals DHs 505 and 705, a localized lens of barite rock overlying carbonate-sulfide rocks with high Pb/Zn + Pb ratios (Figure 14b) was interpreted as a vent site located in deeper water, below the oxic/anoxic chemocline, with barite precipitated during vigorous discharge of hydrothermal fluids into the upper oxic seawater.

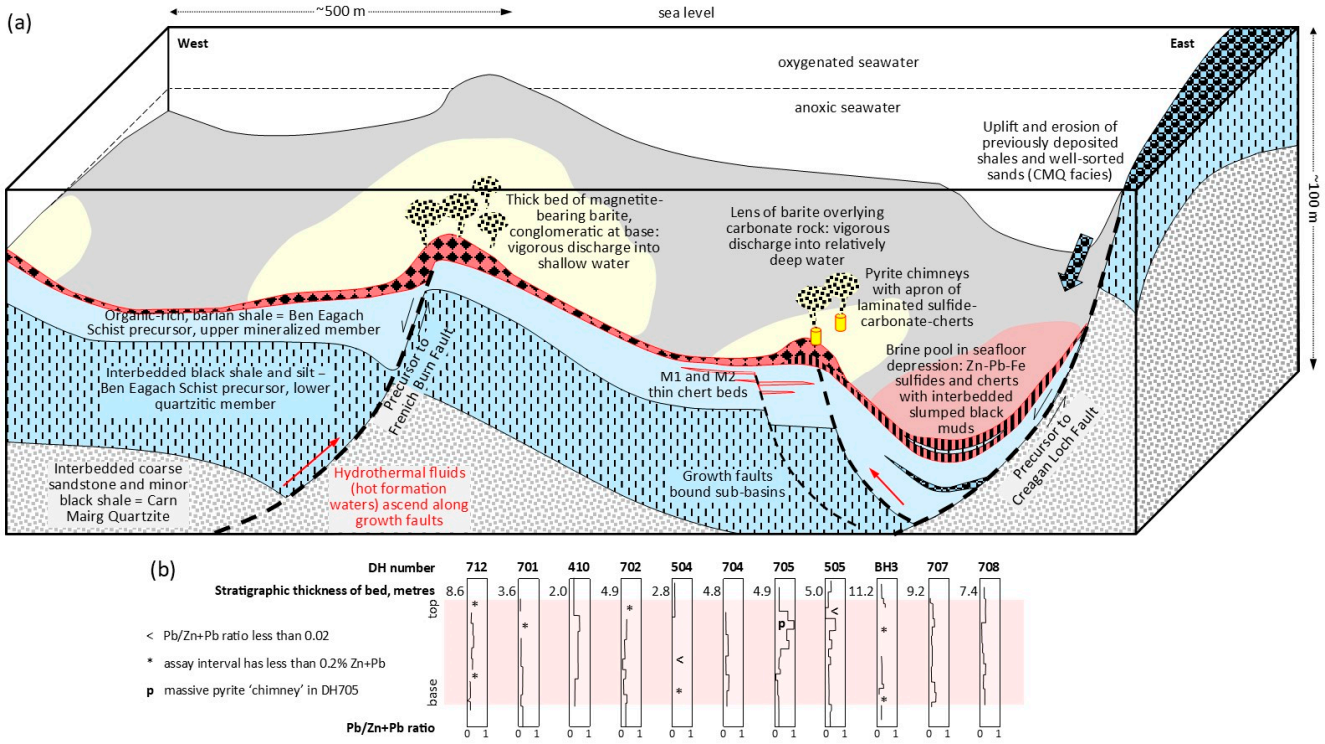


**Figure 14.** (**a**) Conceptual representation of the marine environment during deposition of the first extensive mineralized bed (M3) in the Foss deposit, from Moles and Selby (2023) [44]. Approximately 5 times exaggeration of the vertical scale relative to the horizontal scale. Variations in the rates and types of sediment input are attributed to localized basinal down-warping and uplift associated with syn-sedimentary extensional faulting and rotation of fault blocks. This, together with stratification of oxygen levels in the seawater, accounts for the synchronous precipitation from the same hydrothermal fluids of barite in shallow water, and of chert, carbonate rock, and sulfides in deeper water. Fault uplift and erosion of previously deposited black shales and coarse sands produced debris flows interbedded with the mineralization in a deep-water brine pool at the eastern edge of the deposit. CMQ = Carn Mairg Quartzite. Red arrows indicate the postulated flow of hydrothermal fluids associated with growth faults. (**b**) Pb/Zn + Pb ratios in assay intervals of drillcore through the M3 bed in Foss East, arranged to approximately align with the cross-section above (data from M–I SWACO (unpublished), Coats et al. (1981), and Moles (1985b) [40,45]). The vertical scale varies: the numbers at the top left of each plot represent stratigraphic thickness in meters of each intersection. Pb/Zn + Pb ratios approach 1 in upper parts of the DH705 and DH505 drillhole intersections proximal to a postulated hydrothermal vent location. Figure reprinted from [44] under the CC BY license 4.0, Elsevier.

Sulfide- and chert-rich mineralization with only traces of barite (DHs 707/708; Figure 5a) in the M3 bed at the easternmost extremity of the Foss deposit (Creag an Loch; Figure 2e) may be the product of precipitation from a brine pool [82] in a seafloor depression formed by syn-sedimentary extensional faulting (Figure 14a) [44,52]. The graphitic schist is unusually thick beneath the M3 bed in this area, and this is the only part of the Aberfeldy deposits where substantial amounts of clastic sediment were incorporated into the stratiform mineralization (Figure 5a). Our interpretation is that submarine avalanches of reworked sediment entered the sub-basin before, and during, the M3 exhalative event while the brine pool was precipitating chert and sulfides. This area is also unusual in that the metasediments deposited between M3 and M5/6 include beds of well-sorted sandstone and gritstone, similar to the Carn Mairg Quartzite. We interpreted this as sediment eroded from Carn Mairg Quartzite sediment (not yet lithified) that was uplifted east of the seafloor depression and brine pool (Figure 14). East of the Creag an Loch faults, for a distance of

>2 km, stratiform mineralization is absent in the Ben Eagach Schist until it reappears in outcrops near the summit of Ben Eagach (Figure 2b).

### *5.2. Variation in Mineral Chemistry*

#### 5.2.1. Pyrite

Our preliminary study of Aberfeldy pyrite microchemical compositions showed that these are diverse (Section 4.3.1). We interpreted this diversity as due to chemical features inherited from precipitation of the stratiform mineralization in varied depositional environments (proximal/distal to vent locations, oxic/anoxic bottom waters, or a brine pool). The clear contrast in pyrite composition between proximal and distal mineralization (Figure 8) does not favor a genetic model involving pyrite formation by sub-seafloor replacement processes, as such processes would not be significantly influenced by the redox chemistry of the overlying marine environment.

Unlike sulfide-dominant stratiform ore deposits described in recent studies [83,84], pyrite associated with proximal mineralization in the Aberfeldy deposits has relatively low trace element contents compared with pyrite in distal mineralization and non-mineralized host rocks. In proximal samples (excluding bed-marginal 712-41.40), pyrite Co/Ni ratios ranged 0.16 to 0.34, whereas two distal samples had Co/Ni ratios similar to the host rock ratio of 0.54. One Ni-poor sample (G114) of distal mineralization had a Co/Ni ratio of 2.85. (Ratios are of the median concentrations of Co and Ni in each sample.) Yesares et al. (2022) [83] reported a relatively high Co/Ni ratio > 1 in diagenetically formed pyrite in the Tara Deep part of the Carboniferous, Irish-type, Navan Zn–Pb deposit in Ireland. In the Proterozoic George Fisher massive sulfide Zn–Pb–Ag deposit, Mount Isa, Australia, Reigar et al. (2023) [84] found that in different ore stages, the pyrite is compositionally distinct, consistent with a multi-stage system. Early formed (stage 1) pyrite exceeds background contents of Co, Cu, Zn, As, Ag, Sb, Tl, and Pb and has elevated Co/Ni ratios, whereas only Ni and Co are above background abundances in stage 2 and 3 pyrite, of which only stage 3 has high Co/Ni ratios.

The relatively high concentrations of several elements in the metasediment-derived pyrite (sample CM2-123.37, labeled as A in Figure 8) is typical of early diagenetic iron sulfides in organic-rich sediments [85,86], and may be attributed to transition metal substitution into the pyrrhotite crystal lattice and retention in pyrite during retrograde metamorphic replacement [26,85].

#### 5.2.2. Sphalerite

Through variations in minor element composition, sphalerite has the capacity to record physical and chemical characteristics of the environment of precipitation or metamorphism [87,88]. The lack of evidence for depositional growth zoning, characterized by abrupt and often oscillatory variations in minor element content (e.g., [89]), suggests that zoning, if originally present in Aberfeldy deposits sphalerite, has been erased by recrystallization and intra-crystalline diffusion during prograde metamorphism [85,90]. However, the coexistence on a sub-millimeter scale of discrete sphalerite crystals with contrasting Fe (and Mn) contents indicates that equilibrium domains have been minute and disequilibrium commonly retained, despite regional metamorphism. Concurring with previous studies [45,56,59], we infer that at least some of the observed variation in sphalerite composition has been retained from the time of deposition and/or diagenesis.

Textural features described in Section 4.3.2 (red, Fe-rich sphalerite preferentially encapsulated in pyrite crystals) suggest that, in samples that have a range of sphalerite Fe contents, relatively Fe-rich varieties precipitated earlier than both the Fe-poor sphalerite and much of the pyrite. Moles (1983) [56] suggested that Fe-rich sphalerite (or a Zn-Fe-sulfide precursor, such as wurtzite) was precipitated during the expulsion of hot, weakly acidic, and sulfur-poor metalliferous fluids at the exhalative vents, and was transported in the laterally flowing brine to the site of ore deposition, where more sphalerite with a lower iron content was precipitated in situ. This scenario suggests that (i) primary Fe-rich

sphalerite should be most prominent close to the exhalative vents, and (ii) the iron content of the Fe-poor sphalerite fraction should decrease with distance from the vent area, but the composition of the Fe-rich fraction should be unrelated to this parameter.

However, the detailed study of the Foss East M3 bed described above did not reveal a simple spatial pattern in sphalerite Fe contents, and Fe-rich sphalerite was found in many samples regardless of proximity to the inferred vent sites. Both relatively Fe-rich and Fe-poor sphalerite fractions (where clearly distinguished) were highly variable in composition between samples, and where the matrix sphalerite contained <3 mol% FeS, the coexisting more iron-rich sphalerite contained only 4–6 mol% FeS (Figure 9c). In a SEDEX model, these features could reflect episodic variations in the sulfur content or the rate of discharge of the hydrothermal fluids, or in the oxygen fugacity of the entrained basinal seawater.

A finding significant to the discussion of a syn-sedimentary versus diagenetic replacement origin is the contrasting trend in sphalerite composition with stratigraphic height in the Frenich Burn (DH105) and Creag an Loch (DH708) areas, at opposing ends of the Foss East deposit (Figure 2e). In DH105, the trend of increasing iron content (Figure 9c) with time, if we adopt the SEDEX model and assume progressive stratigraphical deposition of the barite forming the M3 bed, is consistent with a decrease in concentration of sulfur ions due to the restriction of bacterial activity in the relatively shallow, oxidizing environment. These environmental conditions are suggested by the thick accumulation of barite and evidence in this area of mechanical reworking of both the deposited barite (forming barite conglomerate) and of the sediments deposited between the successive hydrothermal events that generated M3 to M7 (Figure 5a). Conversely, if we adopt a diagenetic replacement model, the upward trend of increasing Fe content in sphalerite may be explained by gradients in geochemical parameters, such as $Fe^{2+}$, $SO_4{}^{2-}$, and $H_2S$, in pore water associated with the sulfate-methane transition zone (Figure 1c) [23] during mineralization of a precursor to the barite rock.

In contrast to other intersections examined, bimodal sphalerite populations were absent from the DH708 profile at the eastern extremity of the Foss deposit (Figure 9c). Here, adopting the SEDEX model, this feature may be explained by zinc sulfide precipitation in a stagnant brine pool, comprising a mixture of seawater and hydrothermal fluid that was ponded in a seafloor depression [82] (Figure 14a). A similar decrease in sphalerite Fe content with stratigraphic height was observed in some Kuroko-type VMS deposits [91] and has been attributed largely to a decline in temperature of the ore-forming fluids. However, this trend may also be related to increases in the total sulfur concentration and oxygen fugacity in the brines [92], which also favor the formation of barite. These physicochemical changes may have occurred in the eastern Foss East area (DHs 707 and 708) as the uppermost part of the brine pool mixed with overlying seawater, eventually resulting in precipitation of a small amount of barite (Figure 9c).

As discussed previously, metamorphism has obscured micron-scale textural information that could have provided insights to the paragenesis of Zn and Fe sulfides [24,93–95] in relation to their barite and chert host rocks of the Aberfeldy deposits. In a detailed textural study involving in situ sulfur isotope analyses, Kelley et al. (2004) [93] established the paragenesis of Fe-Zn-Pb mineralization in the Red Dog CD-type deposit complex in northern Alaska. They divided the mineralization into four temporal stages characterized by different colors of sphalerite. Stage 1 brown sphalerite, associated with pyrite, barite, and rare galena, was formed by MSR in unconsolidated organic matter-rich muds. Stage 2 mineralization comprises yellow–brown sphalerite and pyrite, formed by TSR and accompanied by the dissolution of pre-existing barite. The Red Dog sphalerite colors and paragenetic sequence (red preceding yellow–brown) is comparable to that of Foss East M3 sulfide-bearing barite (Figure 9c), although we did not observe evidence of barite dissolution. Moles (1985b) [45] separated red and yellow sphalerite in one barite sample for bulk analysis but found no difference in $\delta^{34}S$, perhaps because of metamorphic equilibration. However, in situ $\delta^{34}S$ analyses (by laser ablation) of encapsulated sphalerite would be

useful in future research. If primary variations in $\delta^{66}Zn$ are preserved on a micron scale, coexisting grains of Fe-rich and Fe-poor sphalerite may yield contrasting values, which would support our hypothesis of their contrasting origin proximal and distal to vents.

In the Aberfeldy stratiform mineralization, primary depositional textures have been modified by grain coarsening during diagenesis, lithification, and subsequent metamorphism, but these processes appear to have not radically changed the diverse primary compositions of sphalerite and pyrite. We contend that the systematic spatial variations in sphalerite Fe content, as with pyrite chemistry, strongly reflect physicochemical variations in the marine environment and, therefore, we favor a syn-depositional origin in preference to formation by post-depositional diagenetic replacement processes.

#### 5.2.3. Barite

The strontium content of Aberfeldy barite varies on scales ranging from meters to microns (Figure 10). The diverse Sr content of barite in inclusions suggests that, as with sphalerite, diagenetic pyrite growth trapped barite grains, which have retained compositional diversity though metamorphism, whereas the comparatively restricted compositional range in the rock matrix may be due to coalescence and equilibration during grain coarsening [45]. The low Sr content of barite associated with carbonate-bearing lithologies (Figure 10a) suggests that, during diagenesis/lithification and/or regional metamorphism, strontium partitioned into carbonates in preference to coexisting barite [1].

Systematic patterns in barite Sr content were not discerned in previous studies of the Aberfeldy deposits [40,45], but more recent work has shown an apparent systematic variation with stratigraphic height in one of several sampling profiles through barite beds (Figure 10b). Paragenetic small-scale (within crystal) variations in Sr contents of barite crystals have been recorded [96] in a barite bed associated with the Kuroko-type VMS deposit at Fukazawa Mine in northern Honshu, Japan. The highest Sr contents are associated with fine-grained, dusty-looking barite. The authors deduced that the barite bed was formed by replacement of an unconsolidated pyritic tuff, with temporal fluctuations in rates of hydrothermal fluid discharge and seawater ingress contributing to the vertical and within-crystal variations in barite Sr content and $^{87}Sr/^{86}Sr$ ratios [96].

### *5.3. Textural Evidence of Diagenesis: Barium Carbonates and Sulfate Pseudomorphs*

The precipitation of barium carbonates requires high carbonate ion activities coupled with very low activities of sulfate ions, much lower than the activity of sulfate in modern seawater (Figure 11a). Finlow-Bates (1980) [92] commented that the occurrence within SEDEX deposits of barium aluminosilicate and barium carbonate minerals may be an indication of low-sulfate depositional environments. However, in the case of the Aberfeldy deposits, sulfate was evidently abundant during deposition of the barite beds [52] and was prevalent in the sediments, as evidenced by abundant disseminated iron sulfides with $\delta^{34}S$ values that are consistent with formation by microbial sulfate reduction, MSR ($\Delta^{34}S_{sulfate\text{-}sulfide}$ ~20‰), as discussed in the following Section 5.4. The conditions necessary for barium carbonates to precipitate are likely to occur during early diagenesis. At this time, pore waters are depleted in $SO_4$ due to MSR, and enriched in $CO_3$ from organic fermentation processes (Figure 1). Consequently, we attribute the formation of barium carbonate minerals in the Aberfeldy mineralization to post-depositional processes involving microbial activity and sediment–porewater interactions (Figure 15A).

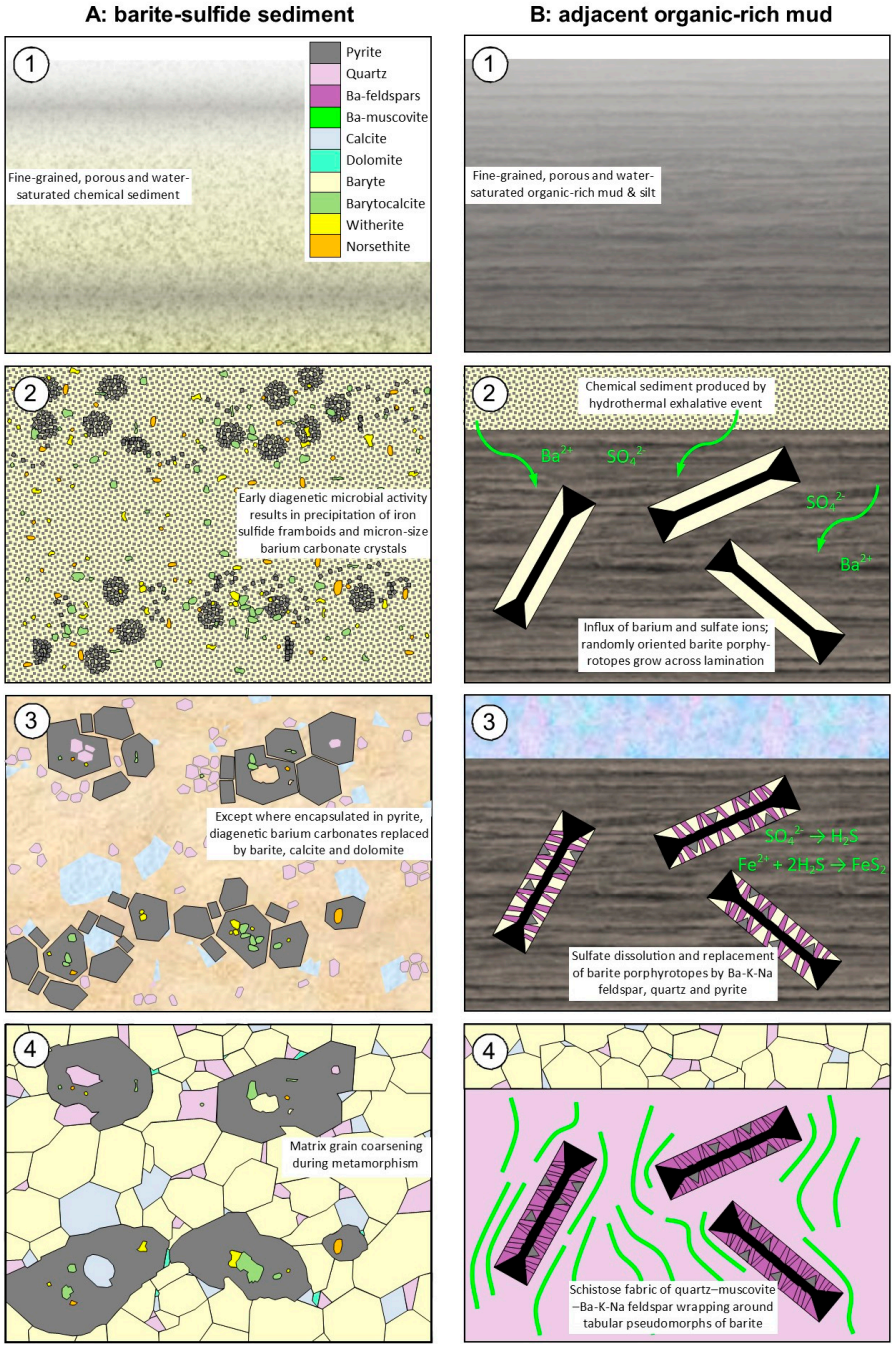


**Figure 15.** Interpretative reconstructions of textures and mineralogy during ① deposition, ② early diagenesis, ③ late diagenesis and lithification, and ④ regional metamorphism of (**A**) barite-sulfide-carbonate mineralization, and (**B**) adjacent mineralized clastic sediment in the Aberfeldy deposits. Sketches represent vertical sections of sediment/rock approximately 3 mm tall and 4 mm wide. Throughout the figure, mineral species are color-coded according to the key in A①.

The occurrence of barium carbonates only as grains encapsulated in crystals of non-reactive minerals, such as pyrite, appears to be due to their preservation in this textural context, and it is probable that barium carbonates were formerly widespread within these sediments. This implies that, later in the diagenetic/lithification sequence, matrix barium carbonates were replaced by barite + calcite or dolomite (i.e., non-barian carbonates), as shown in Figure 15A③. The replacement reactions are represented as follows, with water acting as a solute for ionic species:

(1) barytocalcite + sulfate ions = barite + calcite + bicarbonate ions

$$BaCa(CO_3)_2 + SO_4^{2-} = BaSO_4 + CaCO_3 + CO_3^{2-}$$

(2) norsethite + calcite + sulfate ions = barite + dolomite + bicarbonate ions

$$BaMg(CO_3)_2 + CaCO_3 + SO_4^{2-} = BaSO_4 + CaMg(CO_3)_2 + CO_3^{2-}$$

(3) witherite + sulfate ions = barite + bicarbonate ions

$$BaCO_3 + SO_4^{2-} = BaSO_4 + CO_3^{2-}$$

The sulfate ions required for these reactions may have infiltrated the chemical sediments from porewater in adjoining sediments or may have evolved in situ from the dissolution of sulfate minerals (barite, anhydrite, or gypsum) or from the oxidation of sulfides in the chemical sediments (though a source of the required oxygen is not apparent). These potential sources of sulfate may be constrained by sulfur isotope compositions, discussed in the following section.

Several samples of mineralized sediment adjacent to the stratiform mineralized beds in the Aberfeldy deposits contain bladed 'porphyrotopes', approximately 1 mm wide and 4–7 mm in length, of Ba-K-Na feldspars with complex internal structures and inclusions of quartz, pyrite, and occasionally barite [45]. A coarsely crystalline outer part sandwiches a fine-grained central zone, which has an hourglass shape in the longitudinal section (Figure 6). Fortey and Beddoe-Stephens (1982) [53] illustrated a sample of mineralized sediment from IGS BH9 (Foss West; Figure 2e) that contains the same features. The tabular structures are interpreted as pseudomorphs of barite crystals that formed in the sediments during diagenesis, displacing fine lamination within the sediment. The proximity of the occurrences to stratiform barite beds suggests that the tabular barite crystals formed during an influx of barium and sulfate ions, probably sourced from the adjacent mineralization, as indicated in Figure 15B②. The complex internal structure hints at subsequent replacement processes during which the original barite was dissolved and replaced by Ba-K-Na feldspar, quartz, and pyrite, the crystals of which often show growth approximately perpendicular to the long edges of the tabular shape (Figure 6b–f), as illustrated in Figure 15B③. These features have survived through regional metamorphism because of the replacement of the original sediment by feldspar, which is resistant to deformation, in contrast to unaltered clay-rich sediments, which were transformed into foliated micaceous schists (e.g., Figure 3j), thereby destroying fine textural features.

The presence of early diagenetic mineral products preserved within relatively coarsely crystalline matrices suggests that cementing of the mineralized beds occurred soon after deposition. Intraformational conglomerates within barite (Figures 3d and 4a) and chert beds [45,52] are also evidence of early lithification. The host mudstones probably remained plastic and ductile, except where impregnated and cemented by mineralizing fluids close to the stratiform mineralization. The contrasting rheology of the mineralized beds and host sediments influenced subsequent deformation of the orebodies and accounted for some of the complex structures encountered during mining of barite at Foss (Nick Butcher, personal communication, 2017).

### *5.4. Stable Isotope Evidence for Barite and Sulfide Formation and Post-Depositional Alteration*

Previously, it was mentioned that the sulfur isotope compositional difference between contemporary seawater and sulfide minerals ($\Delta^{34}S$) is often used to interpret whether sulfate reduction was by biologically mediated processes or by thermochemical processes. Sulfide $\delta^{34}S$ values of +12‰ to +16‰ in the Ben Eagach Schist metasediments, although variable, are commonly around 20 ± 4‰ lower than the unmodified $\delta^{34}S$ of seawater sulfate, if this is equated with that of the thicker barite beds, i.e., 36.5 ± 1.5‰ (Figure 12a) [52]. While acknowledging that sulfide $\delta^{34}S$ values, in isolation, do not provide sufficient information

to determine isotopic fractionation processes, we noted that a $\Delta^{34}S$ of ~20‰ could be explained by fractionation during open-system MSR, during which sulfides precipitated within the water column or porewater sulfate was continually replenished by ingress of unmodified seawater. Closed-system MSR is known to generate major to extreme sulfur isotope fractionation in sedimentary sulfides and is commonly observed in carbonate- and shale-hosted Zn-Pb sulfide deposits formed by diagenetic replacement processes, such as those in the Selwyn Basin [22,23,95] and in Ireland [83,97]. Sulfide $\delta^{34}S$ values in samples of Aberfeldy mineralization ranged from around +16‰ to +29‰, peaking at around +23‰ (Figure 12a). $\Delta^{34}S$ values of <20‰ may suggest that sulfur sources other than seawater (e.g., hydrothermal fluids) and/or other isotopic fractionation processes contributed to the formation of these sulfides [98]. Potentially, this could include thermochemical sulfate reduction (TSR) in hot hydrothermal fluids or during deep burial, as invoked for the Selwyn Basin SEDEX-type deposits [99].

In the carbonate-sulfide-barite rock sample 702-4B, in which pyrite crystals contain inclusions of barium carbonates (Figure 7a), the $\delta^{34}S$ of barite (+14‰ to +16‰) and pyrite (+29‰ to +32‰) seem to be the reverse of the 'normal' isotopic compositions of Aberfeldy barite and sulfides (Figure 12a). This may be explained if much of the pyrite-sulfur in this rock was derived from reduction of pre-existing sulfate, and the secondary barite-incorporated sulfur was derived from a sulfide source via an oxidation mechanism. To account for this, we proposed a two-stage process, as illustrated in Figure 16:

1. $^{34}S$-enriched sulfur was incorporated into pyrite from fluids generated during dissolution of primary (hydrothermal) barite, which had incorporated seawater sulfate with a $\delta^{34}S$ value of ~36‰. Barite dissolution and the precipitation of barium carbonates and pyrite (probably as framboids) occurred when low Eh redox conditions were developed in the pore water of the chemical sediment during early diagenetic microbial processes involving sulfate reduction and methanogenesis.
2. Subsequently, perhaps during deep burial diagenesis and/or metamorphism, $^{34}S$-depleted sulfur was incorporated into the matrix barite during sulfidation of barium carbonate in the bulk rock, as discussed in the previous section. This sulfidation involved fluids that were in isotopic equilibrium with sulfides in the $^{32}S$-enriched (meta-) sediments that host the stratiform mineralization.

Barium carbonate-bearing samples 505-15 and BE01-138 also show $^{34}S$ enrichment in pyrite (Table 3). While these values are not exceptional for sulfides in the mineralized beds (Figure 4a), the isotopic heterogeneity may indicate that, as in sample 702-4B, some pyrite incorporated $^{34}S$-enriched sulfur during early diagenetic dissolution of primary barite with formation of barium carbonates.

Isotopic perturbations close to the top and bottom of barite beds are likely to have been fluid-mediated, though it is not immediately apparent as to when the marginal alteration took place. The similar shape of the $\delta^{34}S$ and $\delta^{18}O$ profiles (Figure 4a, DH424) suggests that the same processes simultaneously affected the isotopes of both elements. Moles et al. (2015) [52] attributed the variations to either (i) infiltration of $^{34}S$- and $^{18}O$-enriched pore fluids that interacted with the barite sediment when it was fine-grained and porous or (ii) $^{34}S$ enrichment of the marginal barite during partial dissolution when the lighter $^{32}S$ isotope would likely be preferentially partitioned into the fluid phase and be transported away from the barite bed. Dissolution of barite is enhanced by increases in temperature and salinity [100] and by recrystallization accompanying moderate to high tectonic strain [101] associated with the $\delta^{34}S$ and $\delta^{18}O$ isotopic perturbations. Such evidence might be expected if the alteration occurred during metamorphism. Therefore, our preferred interpretation is that the isotopic anomalies are predominantly related to diagenetic processes (Figure 16). These isotopic alterations were then 'sealed in' during lithification and have survived subsequent metamorphism [1].

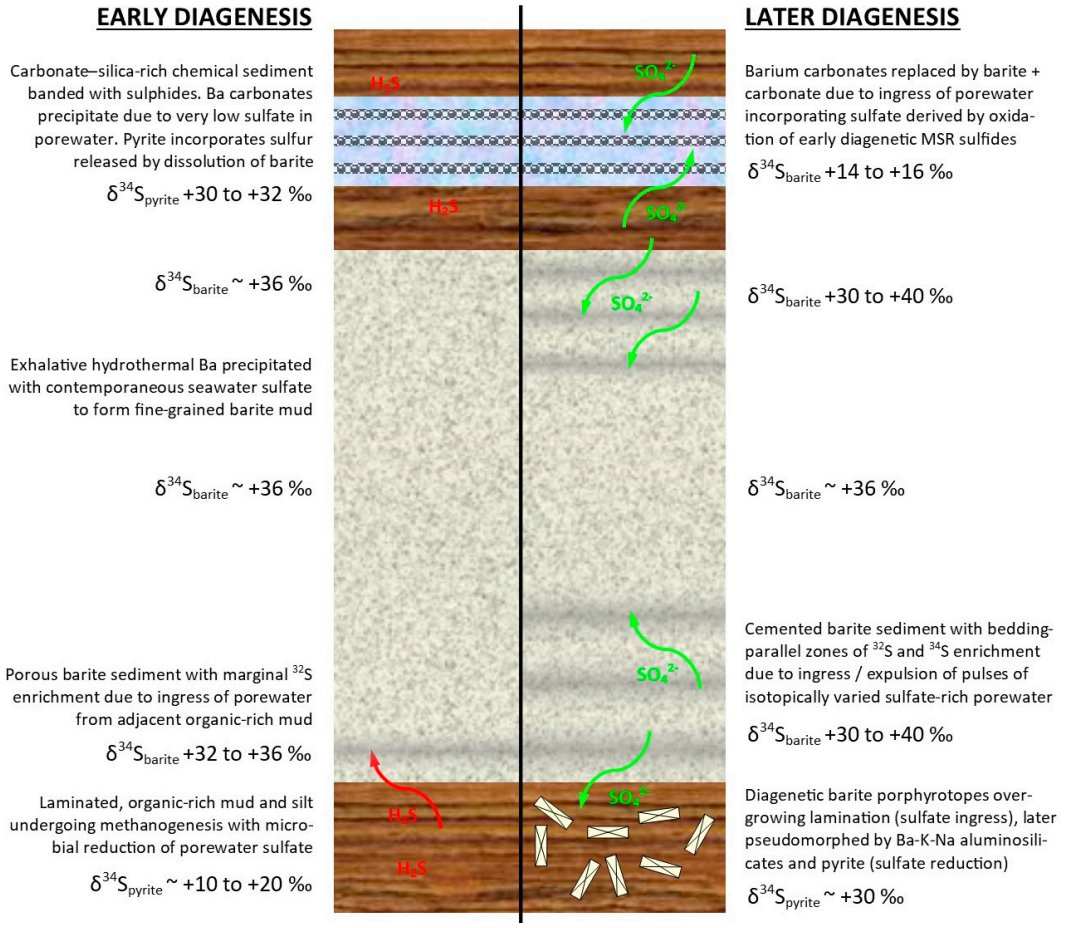


**Figure 16.** Schematic illustration of an Aberfeldy deposit barite bed showing postulated evolution of barite $\delta^{34}S$ and $\delta^{18}O$ associated with early diagenesis and late diagenetic/metamorphic processes.

Isotopic alteration of the bed-marginal barite during early diagenesis is supported by the petrological and isotopic evidence within adjoining cherts and silicified metasediments of sulfate crystallization, followed by replacement by pyrite and Ba-K-Na feldspars (Figure 16). Fluid-mediated transfer of dissolved barium into the adjacent sediments may have generated, or at least enhanced, the barium enrichment observed in these rocks. Similarly, the transfer of sulfur ions into the sediments may have partially obliterated pre-existing contrasts in the isotopic composition of sulfides in the sediments and the stratiform beds, accounting for their overlapping ranges in $\delta^{34}S$ compositions (Figure 12a).

Non-hydrothermal sediment-hosted bedded barite deposits worldwide show marked isotopic variation, with barite $\delta^{34}S$ and $\delta^{18}O$ values far removed from contemporaneous seawater (e.g., [102,103]). The isotopic profiles often resemble those of pore water sulfate observed in modern ocean sediments, implying that barite precipitated from a restricted reservoir of sulfate that had undergone modification during MSR, typically coupled with anaerobic oxidation of methane (Figure 1c) [23,104–106]. Elevated $\delta^{34}S$ values in barite can be derived from sediment porewater in which sulfate has been consumed by oxidation of organic matter or anaerobic oxidation of methane in a closed-system context [14,102,107]. During the fermentation of organic matter in sediments, pyrite formation can generate differential isotope concentration gradients for $^{32}S$- and $^{34}S$-containing solutes [20,23,106–110]. The $\delta^{34}S$ and $\delta^{18}O$ patterns preserved in the margins of Aberfeldy barite beds resemble those of porewater sulfate observed in modern ocean sediments (e.g., [102]), and we suggest that similar processes may account for the perturbations of isotope ratios (Figure 16).

Barite dissolution under the highly reducing conditions associated with diagenesis of organic-rich sediment also allows for extensive migration of barium in the unconsolidated

sediment. This is one explanation for the 'halo' of cryptic barium enrichment in the mica schists hosting the stratiform mineralized beds, as opposed to a process of background discharge (leakage) of hydrothermal fluids into the marine environment between the exhalative events that formed the laterally extensive mineralized beds.

The $\delta^{18}O$ values of Aberfeldy barite range from 8‰ to 18‰ [45,52,54], with the majority in the range 10‰ to 15‰, which is compatible with other Ediacaran-Cambrian sulfates [102,111,112]. Based on analyses of 50 barite samples (incorporating data previously reported by Hall et al., 1991 [54]), we found no consistent spatial patterns in $\delta^{18}O$ or trends in plots of $\delta^{34}S$–$\delta^{18}O$ (Figure 4a). Furthermore, the absence of an overall positive correlation between these isotope values (Figure 4b) suggests that MSR has not been a major influence on barite isotope composition, as MSR typically results in strong positive correlations [102,113,114]. However, barite $\delta^{18}O$ values showed variations of several per mil over short distances near bed margins where barite $\delta^{34}S$ perturbations were evident (Section 4.4.1, Figure 4a). These observations led Moles et al. (2015) [52] to conclude that barite $\delta^{18}O$ had been affected by similar fluid-mediated diagenetic and/or metamorphic alteration processes to those that altered bed-margin barite $\delta^{34}S$, but rather than affecting only the margins, oxygen isotope ratios had been reset throughout the barite beds. If such resetting had taken place, we would not expect to see preservation of an O-MIF signal in any samples of barite rock. The $\Delta^{17}O$ signals we report here (Table 4) imply that, contrary to the previous interpretation, oxygen isotope compositions of non-bed-marginal barite have in fact been preserved and represent original depositional values (Figure 16).

The modification of sulfate oxygen isotope compositions by MSR tends to erase the O-MIF signal inherited from the atmosphere and would drive any negative $\Delta^{17}O$ values in sulfate toward zero [115]. As MSR is very common in the marine realm, this would mean that any $\Delta^{17}O$ value preserved in sedimentary sulfate from this setting should be considered a conservative estimate of the tropospheric $\Delta^{17}O$ value of the period [36]. Additionally, if barite formation involved some incorporation of sulfate from oxidation of sulfide in the water column or in the sediment during diagenesis, this would dilute the bulk-rock O-MIF signal. However, the consistency of $\delta^{34}S$ and $\delta^{18}O$ values in the (non-marginal) barite from which the most negative $\Delta^{17}O$ analyses were obtained in our study (Figure 4a) argues against significant incorporation of oxidized sulfide or modification by MSR processes.

While acknowledging that the Ediacaran environment was characterized by rapid change, we noted that $\Delta^{17}O$ values compiled by Crockford et al. (2019) [36] from deposits at 580 Ma (maximum −0.26‰) and 560 Ma (maximum −0.22‰) were very similar to the value presented here for ~605 Ma (maximum −0.25‰) [44]. This consistency adds to our confidence that the Aberfeldy barite most-negative $\Delta^{17}O$ value is an atmospherically derived signal that is representative of global marine sulfate at this time in Earth's history. This $\Delta^{17}O$ value does not approach that of the pronounced negative $\Delta^{17}O$ excursion, reaching −1.64‰ at the end of the Marinoan glaciation at ~635 Ma (the Marinoan Oxygen-17 Depletion (MOSD) event) [116,117], providing further support for the Aberfeldy deposits not originating in this immediate post-glacial period [44].

Conversely, Aberfeldy carbonate $\delta^{13}C$ values of −5‰ to −10‰ do not reflect contemporaneous global seawater values, unless it is argued that the carbonates were deposited immediately after the Marinoan glaciation at ~635 Ma (Figure 13b), which is inconsistent with geochronological studies [44]. A more plausible explanation for the negative $\delta^{13}C$ values of Aberfeldy carbonates is isotopic homogenization with metamorphic fluids containing carbon derived from oxidation of organic matter, represented by graphite in the host metasediments. This would explain the consistency in $\delta^{13}C$ values of carbonate metasediments and of metamorphic-generated carbonates within metabasites and carbonate-rich mineralization. Carbonate $\delta^{13}C$ and $\delta^{18}O$ values in un-weathered samples from Aberfeldy are similar to those of carbonate rocks that have been strongly affected by metamorphic fluid flow in the axial zones of major anticlinal structures in the Southwest Highlands of Scotland [79] (Figure 13a). We conclude that, at least on a scale of tens of meters, carbonate C and O isotopes have homogenized during regional metamorphism of the Aberfeldy

mineralization and host rocks, and thus do not retain isotopic spatial variations or heterogeneity associated with depositional or diagenetic processes. For this reason, we have not undertaken further carbonate C and O isotope analyses.

### *5.5. Comparisons with Other Stratiform Barite (and Carbonate) Deposits*

Mineral assemblages and textures similar to those described in the Aberfeldy mineralization are reported from other less metamorphosed bedded barite deposits. For example, Moro et al. (2001) [118] describe celsian, cymrite, Ba-K-Na feldspars, and Ba-rich muscovite associated with barite, apatite, and pyrite within Silurian-Devonian SEDEX-type barite deposits in the Zamora Province, Spain. They present textural and isotopic evidence for barite dissolution in reducing conditions associated with MSR during early diagenesis and the subsequent re-precipitation of barite and barium aluminosilicates.

In their description of barite-barytocalcite-witherite stratiform deposits up to 40 m-thick within black chert and shales of Lower Cambrian age in South China, Wang and Li (1991) [119] reported that carbon isotope values of the witherite and barytocalcite were light (average −16‰ $_{PDB}$) relative to contemporaneous seawater, indicating that the carbonate-carbon was derived from organic matter decomposition, and thus, that these minerals formed during early diagenesis.

Ansdell et al. (1989) [120] identified barytocalcite, norsethite, and witherite in the Tom Pb-Zn-Ba deposit in the Macmillan Pass area of Yukon Territory, Canada, and observed that celsian crystals of diagenetic origin are often partially replaced along cleavage planes by barium carbonates. Gardner and Hutcheon (1985) [121] described barytocalcite, benstonite, norsethite, and witherite occurring in lenses parallel to the sedimentary lamination and in cross-cutting veins in the Jason deposit, along strike from Tom. The laminae were deformed around the barium carbonate crystals, suggesting that these minerals developed during diagenesis of the mineralized sediment. Turner and Goodfellow (1990) [122] described barium carbonates of diagenetic origin occurring within a hydrothermal vent complex associated with the Walt stratiform barite deposit, also in the Selwyn Basin of Yukon. As noted above, Magnall and co-authors [23,24] concluded that diagenetic replacement processes were dominant during barite and sulfide mineralization in the Macmillan Pass area. Their in situ micro-analyses demonstrated small-scale isotopic heterogeneities (3‰–4‰ over <50 μm) between individual barite crystals, which the authors attributed to transient changes in the rates of sulfate diffusion and consumption within pore fluid micro-niches. They found widespread evidence of barite replacement by barium carbonates and sulfides. In their paragenetic stage 2a, the $\delta^{34}S$ ratios of pyrite and barite are identical, indicating near-quantitative sulfate reduction to sulfide associated with anoxic oxidation of methane (AOM-SR). The relatively narrow range in $\delta^{34}S$ and $\delta^{18}O$ values of barite in all paragenetic stages of the Macmillan Pass mineralization, and absence of a positive correlation between the isotopes, suggests open-system diffusional exchange with the overlying water column.

Lyons et al. (2006) [123] speculated that high methane availability in the mid-Proterozoic Ocean may have supported high rates of MSR, which in combination with lower overall sulfate concentrations, basin restriction, and strong hydrogen sulfide retention, favored high $\delta^{34}S$ values for metal sulfides in SEDEX-type mineralization. They noted that petrographic evidence for a microbial role in sulfide formation, specifically "crinkly-wavy" laminated pyrite beds, are widespread in the northern Australian Zn-Pb SEDEX-type deposits and have been interpreted as pyritized microbial mats. Some distal mineralized sediment at Aberfeldy has retained similar textures and associated high $\delta^{34}S$ values in pyrite (samples G100 and G114; Figures 11a and 16b).

As the main purpose of this paper was to review evidence for the formation mechanism of the Aberfeldy barite deposits, it is useful to compare isotopic features with modern anoxic marine environments and barite deposits. Johnson et al. [102] noted that in the anoxic water of Framvaren Fjord, Norway, sulfate concentrations decrease with depth, associated with large increases in $\delta^{34}S$ and $\delta^{18}O$ with a positive slope of about 4:1. Conversely, the

Valdivia and Suakin Deeps in the Red Sea, and the Orca Basin in the Gulf of Mexico, contain anoxic hypersaline brines that differ in isotopic composition from modern seawater sulfate due to sulfate addition from the dissolution of underlying Miocene evaporites. In modern cold-seep barite-carbonate deposits in the Sea of Okhotsk, Greinert et al. (2002) [113] found wide ranges in the S and O isotope compositions of barite (range of 18‰ in $\delta^{34}S$, and range of 9‰ in $\delta^{18}O$), which they attributed to the mixing of 'normal' seawater sulfate with porewater sulfate that is residual after biological sulfate reduction and isotopic fractionation. In their barite samples, $\delta^{18}O$ and $\delta^{34}S$ were positively correlated with a slope of 2:1, similar to cold seeps in the Gulf of Mexico, which Greinert et al. [113] interpreted as residual sulfate isotopically changed during microbial sulfate reduction, without any temperature-related equilibration. In the Gulf of Mexico deep marine sediment porewaters, Aharon and Fu (2003) [114] demonstrated a wider range in the slope, from 1.4 to 3.5 in $\delta^{18}O$ vs. $\delta^{34}S$ plots, and they explained the deviation in the ratio as reflecting kinetic fractionation effects rather than elevated temperatures. They noted that MSR and bacterial disproportionation processes result in substantial increases in the values of $\delta^{18}O_{porewater}$ (up to 13‰) and $\delta^{34}S_{porewater}$ (up to 50‰) relative to seawater, i.e., $\Delta^{18}O$ and $\Delta^{34}S$ of up to 13‰ and 50‰, respectively.

### *5.6. Were the Aberfeldy Deposits Syn-Sedimentary Exhalative or Diagenetic Replacement?*

Concurring with Moles et al. (2015) [45], we conclude from the relative homogeneity of isotopic compositions that the Aberfeldy barite beds incorporated Neoproterozoic seawater sulfate in an open-system marine environment rather than in a sub-seafloor porewater environment. The narrow range in $\delta^{18}O$ and $\delta^{34}S$ of (non-marginal) barite and overall absence of a positive association between these isotopes argues against formation in a cold seep environment or through subsurface remobilization of biogenic barium (Table 1). In thicker barite beds, the preservation of an atmospheric $\Delta^{17}O$ signal also supports the hypothesis of barite precipitation in the water column or on the seafloor. This is because an origin by diagenetic replacement processes would preclude the incorporation of atmospheric oxygen and/or would destroy a pre-existing atmospheric $\Delta^{17}O$ signal.

Subsequent to precipitation of the barite sediment, fluxes of sulfate-bearing porewater, derived from the nearby organic-rich sediments, diffused into the margins of the barite beds and modified the primary seawater sulfate isotope composition of marginal barite. These fluxes had alternating enrichments in the light and heavy isotopes of sulfur and oxygen, creating layers of isotopically distinct barite rock parallel to bed margins. Marginal increases in $\delta^{34}S$ were pronounced in barite adjacent to sediments that lacked organic carbon (calcareous mica schist; Figure 4a) and, therefore, would have retained more dissolved sulfate than organic-rich sediments. To some extent, the isotopic perturbations may preserve a record of the microbially mediated porewater sulfate reduction and sulfate replacement processes that took place in the adjoining sediments, as also evidenced by the growth in unconsolidated sediment of diagenetic sulfate porphyrotopes and their subsequent replacement by sulfide-bearing composite pseudomorphs (Figures 15 and 16).

Interestingly, the barite-bed-marginal isotopic perturbations, and occurrences of sediment-hosted sulfate porphyrotopes, were not restricted to the base of barite beds but also occurred at the tops of beds and associated with sediment intercalations within stacked barite beds (Figures 11a and 16). This suggests that organic-rich clastic sediment was deposited quickly following each exhalative event, before pore-sealing of the underlying chemical sediment, such that microbial activity in the overlying clastic sediment generated isotopically diverse porewaters that infiltrated downwards into the barite. From the profiles analyzed, it appears that the infiltration distance from the stratigraphic top down (<0.5 m in lithified chemical sediment) was less than from the bottom up (~1 m).

Barium carbonates within the Aberfeldy ore deposits also formed during diagenetic modification of the chemical sediments, prior to grain coarsening during lithification and/or early metamorphism (Figures 15 and 16). These carbonates precipitated within the sediments from porewaters that had very low sulfate ion activities due to MSR and, there-

fore, did not precipitate barite. Under the highly reducing conditions, barium mobilized in the porewater infiltrated the adjoining sediments, where it was fixed by the precursors to barium muscovite and Ba-K-Na feldspars. Subsequent sulfidation reactions, probably associated with deep burial diagenesis, replaced the non-encapsulated barium carbonates and produced the matrix assemblage of calcite and/or dolomite plus secondary barite, the latter inheriting an isotopic composition very different to that of the primary barite.

Taken together, the mineralogical and sulfur isotope characteristics of the Neoproterozoic chemical and detrital sediments at Aberfeldy confirm that MSR processes were prevalent during both early and late diagenesis and modified the textures and geochemistry of primary sediments. This contrasts with older SEDEX-type deposits, such as the Mesoproterozoic Urquhart Shale, which hosts the Mount Isa Cu-Pb-Zn deposit, in which thermochemical sulfate reduction appears to have been the dominant sulfide-forming process [124]. However, it also contrasts with Phanerozoic SEDEX-/CD-type deposits, such as those in the Macmillan Pass, Yukon, in which diagenetic microbial processes and open-system diffusional exchange with overlying seawater appear to have completely altered the primary mineralogy and resulted in the formation of stratiform barite and Zn-Pb sulfide mineralization [23,24,94]. In the Aberfeldy mineralization, the thicker beds of barite appear to retain primary $\delta^{34}S_{seawater}$ values, with diagenetic influences altering these values mainly at the margins of thick beds and in thinner barite beds.

### *5.7. Proposed Further Research*

Several analytical approaches could potentially provide more nuanced interpretation of the genesis of the Aberfeldy mineralization. Sphalerite trace element analyses by LA-ICP-MS would greatly increase the number of elements available for comparisons with databases of sphalerite chemistry in various ore deposit types globally [88,125,126]. Co-crystallization of sphalerite and pyrite (and other sulfides) can affect the trace element composition of each mineral [127]. Therefore, the trace element compositions of sphalerite and pyrite, coupled with their textural features, are a powerful tool to decipher characteristics of the ore-depositing fluids [126,128].

Zinc isotope analyses would be a valuable follow-up to our sphalerite microchemistry study. $\delta^{66}$Zn is sensitive to Rayleigh fractionation processes and negative kinetic Zn (and Fe) isotope fractionation during sphalerite precipitation [129] and shows significant variation in sediment-hosted deposits. Studies of the Irish Zn-Pb ore-field deposits [130] and the Red Dog (Alaska) sediment-hosted Zn-Pb deposits [131] have found lower $\delta^{66}$Zn closer to the principal hydrothermal fluid conduits and higher $\delta^{66}$Zn in shallower and/or more distal parts of the flow path. We predict that in the Aberfeldy deposits, sphalerite in thick barite beds regarded as proximal to vents could have lower $\delta^{66}$Zn than sphalerite in thinner, distal beds and in the sulfide-chert bed at Creag an Loch.

Barium isotope analyses offer another proxy approach. Crockford et al. (2019b) [6] published a Ba isotope survey of nearly 100 modern and ancient barite deposits, including samples from pelagic (or 'marine'), hydrothermal, terrestrial, Proterozoic stratiform, and cold seep environments. They found that hydrothermal barite (albeit only 3 samples) exhibited the lowest mean $\delta^{138}/^{134}Ba_{NIST}$ value of $-0.07 \pm 0.02$‰, whereas modern marine pelagic barites ($n$ = 61) had a mean $\delta^{138}/^{134}Ba_{NIST}$ value of $+0.04 \pm 0.06$‰. The authors noted that future Ba isotope studies should prove fruitful in identifying depositional processes, particularly when combined with data from more established isotope systems (S, O, Ca, and Sr) [5,32]. A representative set of barite samples from the Aberfeldy mineralization awaits analysis (Peter Crockford, personal communication, 2024).

## 6. Conclusions

We present aspects of the mineralogy and mineral chemistry in relation to local stratigraphy and facies' variations of the Aberfeldy barite deposits that provide useful insights on the genesis of the mineralization, and have not been altered by regional metamorphism. Regional metamorphism, and in particular permeation by metamorphic fluids, has homog-

enized carbon and oxygen isotope compositions in carbonates and overprinted primary fluid inclusions, such that these compositions do not provide insights on the genesis of the mineralization. This may also apply to the strontium content of barite, although some evidence for stratigraphic variation in barite-Sr may be preserved.

S and O isotope compositions in profiles through barite beds provide clear evidence for the formation of barite in the Aberfeldy deposits. Aside from perturbations near bed margins and in beds <1 m-thick, barite beds show generally constant $\delta^{34}S$ and $\delta^{18}O$ values vertically and laterally. This implies barite precipitation from a substantial reservoir of sulfate ions and, therefore, in an open-system marine environment, rather than in a sub-seafloor porewater environment. The atmospheric $\Delta^{17}O$ signal that is typical of global marine sulfate at this time in Earth's history also argues for barite precipitation in the water column or on the seafloor.

It is clear that diagenetic processes contributed to the mineralogical evolution of some lithologies, in particular, carbonate-rich sediments and carbonate-bearing mineralization. In samples of the latter, the preservation of micron-size grains of barium carbonates, encapsulated within millimeter-size crystals of pyrite and other minerals, provides evidence for low-sulfate fluids that likely permeated the chemical sediment during early burial diagenesis. Barium carbonates in the matrix of these sediments (i.e., not encapsulated) were subsequently replaced by barite and non-barian carbonates due to sulfidation by subsequent permeating fluids. This could have been during later diagenesis and lithification, or during prograde metamorphism—with at least one sample (702-4B) showing evidence of retrograde metamorphic recrystallization. In mineralized sediments adjacent to some barite beds, pseudomorphs of millimetric crystals of barite and gypsum that grew across sedimentary lamination also indicate early diagenetic mobility of Ba, Ca, and sulfate ions before sediment lithification.

Nonetheless, pronounced lateral facies' variations in the stratiform mineralization were clearly associated with proximity to hydrothermal vents and water depth (above/below an oxic/euxinic chemocline). These facies' variations, together with spatially varying pyrite and sphalerite microchemistry, manifest the strong influence of physiochemical conditions in the depositional basin environment, and challenge the hypothesis that the stratiform mineralization was originally formed through diagenetic replacement processes. The sharp external and internal boundaries of the mineralized beds and general absence of incorporated sediment also argue against their formation by replacement processes.

In conclusion, it appears that the Aberfeldy barite deposits provide an example of the 'classic' model of SEDEX mineralization. They formed on the Neoproterozoic seafloor from the mixing of exhaled metalliferous hydrothermal fluids with seawater of varying redox chemistry in stratified marine basins. Diagenetic processes modified sulfide- and carbonate-rich laminated mineralization and marginal parts of barite beds but did not alter the primary isotopic composition of thicker barite beds, which retained the characteristic signature of atmosphere-derived oxygen. Although subsequent regional metamorphism and deformation modified ore textures, the detailed studies reported here have uncovered pristine petrographic and geochemical features surviving from initial deposition and early diagenesis of the chemical sediments.

**Author Contributions:** Conceptualization, N.R.M.; methodology, N.R.M., A.J.B. and M.R.W.; resources, A.J.B. and M.W.C.; validation, N.R.M., A.J.B. and M.R.W.; investigation, N.R.M., A.J.B., M.R.W. and M.W.C.; data curation, N.R.M.; writing—original draft preparation, N.R.M.; writing—review and editing, N.R.M., A.J.B., M.R.W. and M.W.C.; visualization, N.R.M.; funding acquisition, M.W.C. All authors have read and agreed to the published version of the manuscript.

**Funding:** This project has received funding from the European Research Council under the European Union's Horizon 2020 Research and Innovation Programme (Grant 678812 to M.W.C.).

**Data Availability Statement:** Drillcore obtained in the late 1970s by the British Geological Survey (then IGS), together with representative drillcore obtained in the 1980s by Dresser Minerals from

the Foss and Ben Eagach–Duntanlich deposits, and samples analyzed in this study, are stored at the British Geological Survey's National Geoscience Repository (NGR) at Keyworth, England.

**Acknowledgments:** For support during the initial research work, N.R.M. is grateful to Colin Graham and Roy Gill, formerly at the Grant Institute of Geology, University of Edinburgh, Steve Laux, Alan Burns, and Mark Boast, formerly of Dresser Minerals, and Graham Smith and the late Mike Gallagher, formerly of the British Geological Survey, Edinburgh. We thank Owen Dickinson and Ian Hughes of M–I Drilling Fluids UK Ltd. (Aberdeen, Scotland) for assistance with mine access and sample collection. N.R.M. thanks Pete Lyons and Magda Grove for support with laboratory work at the University of Brighton. We thank Claire Geel (iCRAG, University College Dublin) for providing pyrite LA-ICP-MS analyses, Andy Tindle for EMPA analyses at the Open University (Milton Keynes, UK) and Tony Fallick and Alison MacDonald for facilitating isotope analyses at SUERC. M.R.W. and M.W.C. thank Huiming Bao and Yongbo Peng for their assistance and expertise in measuring triple-oxygen isotope values at LSU and for their warm hospitability. The authors thank Jake Ciborowski and the referees for their constructive reviews, which helped us to improve the paper.

**Conflicts of Interest:** The authors declare no conflicts of interest.

## References

1. Hanor, J.S. Barite-celestite geochemistry and environments of formation. In *Sulfate Minerals*; Alpers, C.N., Jambor, J.L., Nordstrom, D.K., Eds.; Reviews in Mineralogy and Geochemistry; Mineralogical Society of American: Washington, DC, USA, 2000; Volume 40, pp. 193–275.
2. Clark, S.H.B.; Poole, F.G.; Wang, Z. Comparison of some sediment-hosted, stratiform barite deposits in China, the United States, and India. *Ore Geol. Rev.* **2004**, *24*, 85–101. [CrossRef]
3. Jewell, P.W. Bedded barite in the geologic record. In *Marine Authigenesis: From Global to Microbial*; Glenn, C.R., Prevot-Lucas, L., Lucas, J., Eds.; Society for Sedimentary Geology (SEPM) Spec. Publ.: Tulsa, OK, USA, 2000; Volume 66, pp. 147–161. [CrossRef]
4. Griffith, E.M.; Paytan, A. Barite in the ocean—Occurrence, geochemistry and palaeoceanographic applications. *Sedimentology* **2012**, *59*, 1817–1835. [CrossRef]
5. Horner, T.J.; Pryer, H.V.; Nielsen, S.G.; Crockford, P.W.; Gauglitz, J.M.; Wing, B.A.; Ricketts, R.D. Pelagic barite precipitation at micromolar ambient sulfate. *Nat. Commun.* **2017**, *8*, 1342. [CrossRef]
6. Crockford, P.W.; Wing, B.A.; Paytan, A.; Hodgskiss, M.S.; Mayfield, K.K.; Hayles, J.A.; Middleton, J.E.; Ahm, A.-S.C.; Johnston, D.T.; Caxito, F.; et al. Barium-isotopic constraints on the origin of post-Marinoan barites. *Earth Planet. Sci. Lett.* **2019**, *519*, 234–244. [CrossRef]
7. Eickmann, B.; Thorseth, I.H.; Peters, M.; Strauss, H.; Bröcker, M.; Pedersen, R.B. Barite in hydrothermal environments as a recorder of subseafloor processes: A multiple-isotope study from the Loki's Castle vent field. *Geobiology* **2014**, *12*, 308–321. [CrossRef]
8. Leach, D.L.; Sangster, D.F.; Kelley, K.D.; Large, R.R.; Garven, G.; Allen, C.R.; Gutzmer, J.; Walters, S. Sediment-hosted lead-zinc deposits: A global perspective. In *Economic Geology 100th Anniversary Volume*; Hedenquist, J.W., Thompson, J.F.H., Goldfarb, R.J., Richards, J.P., Eds.; Society of Economic Geologists, Inc.: Littleton, CO, USA, 2005; pp. 561–607.
9. Emsbo, P. Geologic criteria for the assessment of sedimentary exhalative (sedex) Zn-Pb-Ag deposits. *U.S. Geol. Surv. Open-File Rep.* **2009**, *1209*, 21.
10. Sangster, D.F.; Hillary, E.M. SEDEX lead-zinc deposits: Proposed sub-types and their characteristics. *Expl. Min. Geol.* **1998**, *7*, 341–357.
11. Sangster, D.F. Toward an integrated genetic model for vent-distal SEDEX deposits. *Miner. Depos.* **2018**, *53*, 509–527. [CrossRef]
12. Andrew, C.J. The Ballynoe stratiform barite deposit, Silvermines, County Tipperary, Ireland. *Minerals* **2024**, *14*, 498. [CrossRef]
13. Canet, C.; Anadón, P.; González-Partida, E.; Alfonso, P.; Rajabi, A.; Pérez-Segura, E.; Alba-Aldave, L.A. Paleozoic bedded barite deposits from Sonora (NW Mexico): Evidence for a hydrocarbon seep environment of formation. *Ore Geol. Rev.* **2014**, *56*, 292–300. [CrossRef]
14. Gao, J.; Yang, R.; Chen, J.; Zheng, L.; Cheng, W.; Wei, H. Multiple proxies indicating methane seepage as the origin of Devonian large barite deposit in Zhenning-Ziyun, Guizhou, SW China. *Ore Geol. Rev.* **2017**, *80*, 18–26. [CrossRef]
15. Paytan, A.; Mearon, S.; Cobb, K.; Kastner, M. Origin of marine barite deposits: Sr and S isotope characterization. *Geology* **2002**, *30*, 747–750. [CrossRef]
16. Torres, M.E.; Brumsack, H.J.; Bohrmann, G.; Emeis, K.C. Barite fronts in continental margin sediments: A new look at barium remobilization in the zone of sulphate reduction and formation of heavy barites in diagenetic fronts. *Chem. Geol.* **1996**, *127*, 125–139. [CrossRef]
17. Feng, D.; Roberts, H. Geochemical characteristics of the barite deposits at cold seeps from the northern Gulf of Mexico. *Earth Planet. Sci. Lett.* **2011**, *309*, 89–99.
18. Magnall, J.M.; Hayward, N.; Gleeson, S.A.; Schleicher, A.; Dalrymple, I.; King, R.; Mahlstadt, N. The Teena Zn-Pb Deposit (McArthur Basin, Australia). Part II: Carbonate Replacement Sulfide Mineralization during Burial Diagenesis—Implications for Mineral Exploration. *Econ. Geol.* **2021**, *116*, 1769–1801. [CrossRef]

19. Jewell, P.W. Paleoredox conditions and the origin of bedded barites along the Late Devonian North American continental margin. *J. Geol.* **1994**, *102*, 151–164. [CrossRef]
20. Torres, M.E.; Bohrmann, G.; Dubé, T.E.; Poole, F.G. Formation of modern and Paleozoic stratiform barite at cold methane seeps on continental margins. *Geology* **2003**, *31*, 897–900. [CrossRef]
21. Han, T.; Peng, Y.; Bao, H. Sulfate-limited euxinic seawater facilitated Paleozoic massively bedded barite deposition. *Earth Planet. Sci. Lett.* **2022**, *582*, 117419. [CrossRef]
22. Fernandes, N.A.; Gleeson, S.A.; Magnall, J.M.; Creaser, R.A.; Martel, E.; Fischer, B.J.; Sharp, R. The origin of Late Devonian (Frasnian) stratiform and stratabound mudstone-hosted barite in the Selwyn Basin, Northwest Territories, Canada. *Mar. Pet. Geol.* **2017**, *85*, 1–15. [CrossRef]
23. Magnall, J.M.; Gleeson, S.A.; Stern, R.A.; Newton, R.J.; Poulton, S.W.; Paradis, S. Open system sulphate reduction in a diagenetic environment—Isotopic analysis of barite ($\delta^{18}O$ and $\delta^{34}S$) and pyrite ($\delta^{34}S$) from the Tom and Jason Late Devonian Zn–Pb–Ba deposits, Selwyn Basin, Canada. *Geochim. Cosmochim. Acta* **2016**, *180*, 146–163. [CrossRef]
24. Magnall, J.M.; Gleeson, S.A.; Creaser, R.A.; Paradis, S.; Glodny, J.; Kyle, J.R. The mineralogical evolution of the Clastic Dominant-Type Zn-Pb + Ba deposits at Macmillan Pass (Yukon, Canada)—Tracing subseafloor barite replacement in the layered mineralization. *Econ. Geol.* **2020**, *115*, 961–979. [CrossRef]
25. Carne, R.C.; Cathro, R.J. Sedimentary exhalative (sedex) zinc-lead-silver deposits, northern Canadian Cordillera. *Can. Min. Metall. Bull.* **1982**, *75*, 66–78.
26. Alirezaei, S.; Cameron, E.M. Variations of sulfur isotopes in metamorphic rocks from Bamble Sector, Southern Norway: A laser probe study. *Chem. Geol.* **2001**, *181*, 23–45. [CrossRef]
27. Giacometti, F.; Evans, K.A.; Rebay, G.; Cliff, J.; Tomkins, A.G.; Rossetti, P.; Vaggelli, G.; Adams, D.T. Sulfur isotope evolution in sulfide ores from Western Alps: Assessing the influence of subduction-related metamorphism. *Geochem. Geophys. Geosyst.* **2014**, *15*, 3808–3829. [CrossRef]
28. Muller, E.; Philippot, P.; Rollion-Bard, C.; Cartigny, P.; Assayag, N.; Marin-Carbonne, J.; Mohan, R.R.; Sarma, D.S. Primary sulfur isotope signatures preserved in high-grade Archean barite deposits of the Sargur Group, Dharwar Craton, India. *Precambrian Res.* **2017**, *295*, 38–47. [CrossRef]
29. Xu, L.; Lehmann, B.; Mao, J.; Zheng, W.; Ye, H.; Li, H. Strontium, sulfur, carbon, and oxygen isotope geochemistry of the Early Cambrian strata-bound barite and witherite deposits of the Qinling-Daba Region, northern margin of the Yangtze Craton, China. *Econ. Geol.* **2016**, *111*, 695–718. [CrossRef]
30. Griffith, E.M.; Paytan, A.; Wortmann, U.G.; Eisenhauer, A.; Scher, H.D. Combining metal and nonmetal isotopic measurements in barite to identify mode of formation. *Chem. Geol.* **2018**, *500*, 148–158. [CrossRef]
31. Averyt, K.B.; Paytan, A. Empirical partition coefficients for Sr and Ca in marine barite: Implications for reconstructing seawater Sr and Ca concentrations. *Geochem. Geophys. Geosyst.* **2003**, *4*, 1043. [CrossRef]
32. Monnin, C.; Galinier, C. The solubility of celestite and barite in electrolyte solutions and natural waters at 25 °C: A thermodynamic study. *Chem. Geol.* **1988**, *71*, 283–296. [CrossRef]
33. Canfield, D.E.; Farquhar, J. Animal evolution, bioturbation, and the sulfate concentration of the oceans. *Proc. Natl. Acad. Sci. USA* **2009**, *106*, 8123–8127. [CrossRef]
34. Lyons, T.W.; Anbar, A.D.; Severmann, S.; Scott, C.; Gill, B.C. Tracking euxinia in the ancient ocean: A multiproxy perspective. *Annu. Rev. Earth Planet. Sci.* **2009**, *37*, 507–534. [CrossRef]
35. Kunzmann, M.; Bui, T.H.; Crockford, P.W.; Halverson, G.P.; Scott, C.; Lyons, T.W.; Wing, B.A. Bacterial sulfur disproportionation constrains timing of Neoproterozoic oxygenation. *Geology* **2017**, *45*, 207–210. [CrossRef]
36. Crockford, P.W.; Kunzmann, M.; Bekker, A.; Hayles, J.; Bao, H.; Halverson, G.P.; Peng, Y.; Bui, T.H.; Cox, G.M.; Wing, B.A.; et al. Claypool continued: Extending the isotopic record of sedimentary sulfate. *Chem. Geol.* **2019**, *513*, 200–225. [CrossRef]
37. Antler, G.; Turchyn, A.V.; Herut, B.; Sivan, O. A unique isotopic fingerprint of sulfate-driven anaerobic oxidation of methane. *Geology* **2015**, *43*, 619–622. [CrossRef]
38. Treagus, J.E. *The Solid Geology of the Schiehallion District*; British Geological Survey: Edinburgh, UK, 2000.
39. Coats, J.S.; Smith, C.G.; Fortey, N.J.; Gallagher, M.J.; May, F.; McCourt, W.J. Stratabound barium-zinc mineralization in Dalradian Schist near Aberfeldy, Scotland. *Trans. Inst. Min. Metall.* **1980**, *89*, B110–B122.
40. Coats, J.S.; Smith, C.G.; Gallagher, M.J.; May, F.; McCourt, W.J.; Parker, M.E.; Fortey, N.J. Stratabound Barium-Zinc Mineralization in Dalradian Schist near Aberfeldy, Scotland: Final Report; Institute of Geological Sciences Mineral Reconnaissance Programme Report No. 40; 1981; 128p. (WF/MR/81/040) (Unpublished). Available online: https://nora.nerc.ac.uk/id/eprint/11896 (accessed on 21 August 2024).
41. BGS/ODPM. *Minerals Planning Factsheet—Barytes*; British Geological Survey and Office of the Deputy Prime Minister: Nottingham, UK, 2006; p. 5.
42. M-I SWACO. *Duntanlich Mine Plan*; Dalgleish Associates Limited: Dunblane, Scotland, 2014.
43. Treagus, J.E.; Tanner, P.W.G.; Thomas, P.R.; Scott, R.A.; Stephenson, D. The Dalradian rocks of the central Grampian Highlands of Scotland. *Proc. Geol. Assoc.* **2013**, *124*, 148–214. [CrossRef]
44. Moles, N.R.; Selby, D. Implications of new geochronological constraints on the Aberfeldy stratiform barite deposits, Scotland, for the depositional continuity and global correlation of the Neoproterozoic Dalradian Supergroup. *Precambrian Res.* **2023**, *384*, 21. [CrossRef]

45. Moles, N.R. Geology, Geochemistry and Petrology of the Foss Stratiform Barite–Base Metal Deposit and Adjacent Dalradian Metasediments, near Aberfeldy, Scotland. Ph.D. Thesis, University of Edinburgh, Edinburgh, UK, 1985; Unpublished.
46. Willan, R.C.R. Geochemistry of the Ben Eagach Schist, Dalradian Supergroup: Dispersion haloes from Aberfeldy-type hydrothermal centres? (extended abstract). In Proceedings of the Mineralisation in the Caledonides: Mike Gallagher Meeting, Edinburgh, Scotland, 27–28 June 1996.
47. Rugen, E.J.; Pastore, G.; Vermeesch, P.; Spencer, A.M.; Webster, D.; Smith, A.G.G.; Carter, A.; Shields, G.A. Glacially influenced provenance and Sturtian affinity revealed by detrital zircon U-Pb ages from sandstones in the Port Askaig Formation, Dalradian Supergroup. *J. Geol. Soc. Lond.* **2024**, *181*, 1–10. [CrossRef]
48. Russell, M.J.; Hall, A.J.; Willan, R.C.R.; Allison, I.; Anderton, R.; Bowes, G. On the origin of the Aberfeldy celsian+barite+base-metal deposits, Scotland. In *Prospecting in Areas of Glaciated Terrain Symposium Volume*; Institute of Mining and Metallurgy: London, UK, 1984; pp. 159–170.
49. Hall, A.J. Stratiform mineralization in the Dalradian of Scotland. In *Mineralization in the British Isles*; Pattrick, R.A.D., Polya, D.A., Eds.; Chapman and Hall: London, UK, 1993; pp. 38–101.
50. van Staal, C.R.; Zagorevski, A. Paleozoic tectonic evolution of the rifted margins of Laurentia. In *Laurentia: Turning Points in the Evolution of a Continent: Geological Society of America Memoir*; Whitmeyer, S.J., Williams, M.L., Kellett, D.A., Eds.; Geological Society of America: Boulder, CO, USA, 2023; Volume 220, pp. 487–503. [CrossRef]
51. Ruffell, A.H.; Moles, N.R.; Parnell, J. Characterisation and prediction of sediment-hosted ore deposits using sequence stratigraphy. *Ore Geol. Rev.* **1998**, *12*, 207–223. [CrossRef]
52. Moles, N.R.; Boyce, A.J.; Fallick, A.E. Abundant sulphate in the Neoproterozoic ocean: Implications of constant $\delta^{34}S$ of barite in the Aberfeldy SEDEX deposits, Scottish Dalradian. In *Ore Deposits in an Evolving Earth*; Jenkin, G.R.T., Lusty, P.A.J., McDonald, I., Smith, M.P., Boyce, A.J., Wilkinson, J.J., Eds.; Special Publication of the Geological Society of London: London, UK, 2015; Volume 393, pp. 189–212. [CrossRef]
53. Fortey, N.J.; Beddoe-Stephens, B. Barium silicates in stratabound Ba-Zn mineralization in the Scottish Dalradian. *Mineral. Mag.* **1982**, *46*, 63–72. [CrossRef]
54. Hall, A.J.; Boyce, A.J.; Fallick, A.E.; Hamilton, P.J. Isotopic evidence of the depositional environment of Late Proterozoic stratiform mineralisation, Aberfeldy, Scotland. *Chem. Geol. (Isot. Geosci. Sect.)* **1991**, *87*, 99–114. [CrossRef]
55. Algeo, T.J.; Morford, J.; Cruse, A. New applications of trace metals as proxies in marine paleoenvironments (Editorial). *Chem. Geol.* **2012**, *306–307*, 160–164. [CrossRef]
56. Moles, N.R. Sphalerite composition in relation to deposition and metamorphism of the Foss stratiform Ba-Zn-Pb deposit, Aberfeldy, Scotland. *Mineral. Mag.* **1983**, *47*, 487–500. [CrossRef]
57. Willan, R.C.R.; Coleman, M.L. Sulfur isotope study of the Aberfeldy barite, zinc, lead deposit and minor sulphide mineralization in the Dalradian metamorphic terrain, Scotland. *Econ. Geol.* **1983**, *78*, 1619–1656. [CrossRef]
58. Hall, A.J. Pyrite–pyrrhotine redox reactions in nature. *Mineral. Mag.* **1986**, *50*, 223–229. [CrossRef]
59. Moles, N.R. Metamorphic conditions and uplift history in central Perthshire: Evidence from mineral equilibria in the Foss celsian-barite-sulphide deposit, Aberfeldy. *J. Geol. Soc. Lond.* **1985**, *142*, 39–52. [CrossRef]
60. Fisk, S. An Oxygen Isotope Study of Siliceous Rocks Associated with Stratabound Mineralisation in Scotland and Ireland. Ph.D. Thesis, University of Strathclyde, Glasgow, UK, 1986; Unpublished. p. 270.
61. Veizer, J. Strontium isotopes in seawater through time. *Annu. Rev. Earth Planet. Sci.* **1989**, *17*, 141–167. [CrossRef]
62. Russell, M.J. The evolution of the Scottish mineral sub-province. *Scott. J. Geol.* **1985**, *21*, 513–545. [CrossRef]
63. Thiemens, M.H. History and applications of mass-independent isotope effects. *Annu. Rev. Earth Planet. Sci.* **2006**, *34*, 217–262. [CrossRef]
64. Yung, Y.L.; DeMore, W.B.; Pinto, J.P. Isotopic exchange between carbon dioxide and ozone via O(1D) in the stratosphere. *Geophys. Res. Lett.* **1991**, *18*, 13–16. [CrossRef]
65. Wilson, S.; Ridley, W.; Koenig, A. Development of sulfide calibration standards for the laser ablation inductively-coupled plasma-mass spectrometry technique. *J. Anal. At. Spectrom.* **2002**, *17*, 406–409. [CrossRef]
66. Onuk, P. High-Tech Metal Potential of Sphalerite from Eastern Alpine Lead-Zinc Deposits and Development of a Matrix-Matched Sphalerite (ZnS) Calibration Material (MUL-ZnS-1) for Calibration of In Situ Trace Element Measurements by Laser Ablation Inductively Coupled Plasma Mass Spectrometry (LA-ICP-MS). Ph.D. Thesis, Montanuniversitaet Leoben, Leoben, Austria, 2018.
67. Savard, D.; Bouchard-Boivin, B.; Barnes, S.; Garbe-Schönberg, D. UQAC-FeS: A new series of base metal sulfide quality control reference material for LA-ICP-MS analysis. In Proceedings of the 10th International Conference on the Analysis of Geological and Environmental Materials 2018, Sydney, Australia, 8–13 July 2018.
68. Woodhead, J.D.; Hellstrom, J.; Hergt, J.M.; Greig, A.; Mass, R. Isotopic and elemental imaging of geological materials by Laser Ablation Inductively Coupled Plasma-Mass Spectrometry. *Geostand. Geoanalytical Res.* **2007**, *31*, 331–343. [CrossRef]
69. Ulrich, T.; Kamber, B.S.; Jugo, P.J.; Tinkham, D.K. Imaging element distribution patterns in minerals by laser ablation-inductively coupled plasma-mass spectrometry (LA-ICP-MS). *Can. Mineral.* **2009**, *47*, 1001–1012. [CrossRef]
70. Robinson, B.W.; Kusakabe, M. Quantitative preparation of sulfur dioxide, for $^{34}S$-$^{32}S$ analyses, from sulfides by combustion with cuprous oxide. *Anal. Chem.* **1975**, *47*, 1179–1181. [CrossRef]
71. Coleman, M.L.; Moore, M.P. Direct reduction of sulfates to sulfate dioxide for isotopic analysis. *Anal. Chem.* **1978**, *50*, 1594–1595. [CrossRef]

72. Wagner, T.; Boyce, A.J.; Fallick, A.E. Laser combustion analysis of $\delta^{34}S$ of sulfosalt minerals: Determination of the fractionation systematics and some crystal-chemical considerations. *Geochim. Cosmochim. Acta* **2002**, *66*, 2855–2863. [CrossRef]
73. Pettigrew, R.P.; Priddy, C.; Clarke, S.M.; Warke, M.R.; Stüeken, E.E.; Claire, M.W. Sedimentology and isotope geochemistry of transitional evaporitic environments within arid continental settings: From erg to saline lakes. *Sedimentology* **2021**, *68*, 907–942. [CrossRef]
74. Bao, H. Purifying barite for oxygen isotope measurement by dissolution and reprecipitation in a chelating solution. *Anal. Chem.* **2006**, *78*, 304–309. [CrossRef]
75. Forjanes, P.; Astilleros, J.M.; Fernandez-Diaz, L. The formation of barite and celestite through the replacement of gypsum. *Minerals* **2020**, *10*, 189. [CrossRef]
76. Fu, Q.; Qing., H.; Bergman, K. Petrography of diagenetic anhydrite in the Middle Devonian Winnipegosis and Ratner formations, south-central Saskatchewan. In *Summary of Investigations*; Saskatchewan Geological Survey, Saskatchewan Industry and Resources, Misc. Rep.: Regina, SK, Canada, 2002; Volume 1, pp. 15–23.
77. Back, M.E. *Fleischer's Glossary of Mineral Species*, 13th ed.; Mineralogical Association of Canada: Québec, QC, Canada; Mineralogical Record Inc.: Tucson, AZ, USA, 2022; p. 431.
78. Maynard, J.B.; Okita, P.M. Bedded barite deposits in the United States, Canada, Germany, and China: Two major types based on tectonic setting. *Econ. Geol.* **1991**, *86*, 364–376. [CrossRef]
79. Pitcairn, I.K.; Skelton, A.D.L.; Broman, C.; Arghe, F.; Boyce, A.J. Structurally focused fluid flow during orogenesis: The Islay Anticline, SW Highlands, Scotland. *J. Geol. Soc.* **2010**, *167*, 659–674. [CrossRef]
80. Cole, C.M. Mechanisms and Timing of Metamorphic Fluid Flow in the Scottish Dalradian. Ph.D. Thesis, University of Edinburgh, Edinburgh, UK, 1997.
81. Prave, A.R.; Fallick, A.E.; Thomas, C.W.; Graham, C.M. A composite C-isotope profile for the Neoproterozoic Dalradian Supergroup of Scotland and Ireland. *J. Geol. Soc.* **2009**, *166*, 845–857. [CrossRef]
82. Sangster, D.F. The role of dense brines in the formation of vent-distal sedimentary-exhalative (SEDEX) lead-zinc deposits: Field and laboratory evidence. *Miner. Depos.* **2002**, *37*, 149–157. [CrossRef]
83. Yesares, L.; Menuge, J.F.; Blakeman, R.J.; Ashton, J.H.; Boyce, A.J.; Coller, D.; Drummond, D.A.; Farrelly, I. Pyritic mineralization halo above the Tara Deep Zn-Pb deposit, Navan, Ireland: Evidence for sub-seafloor exhalative hydrothermal processes? *Ore Geol. Rev.* **2022**, *140*, 104415. [CrossRef]
84. Rieger, P.; Magnall, J.M.; Gleeson, S.A.; Oelze, M. Pyrite chemistry records a multistage ore forming system at the Proterozoic George Fisher massive sulfide Zn-Pb-Ag deposit, Mount Isa, Australia. *Front. Earth Sci.* **2023**, *11*, 892759. [CrossRef]
85. Craig, J.R.; Vokes, F.M. The metamorphism of pyrite and pyritic ores: An overview. *Mineral. Mag.* **1993**, *57*, 3–18. [CrossRef]
86. Steadman, J.A.; Large, R.R. Synsedimentary, diagenetic, and metamorphic pyrite, pyrrhotite, and marcasite at the Homestake BIF-hosted gold deposit, South Dakota, USA: Insights on Au-As ore genesis from textural and LA-ICP-MS trace element studies. *Econ. Geol.* **2016**, *111*, 1731–1752. [CrossRef]
87. Scott, S.D. Chemical behaviour of sphalerite and arsenopyrite in hydrothermal and metamorphic environments. *Mineral. Mag.* **1983**, *47*, 427–435. [CrossRef]
88. Cook, N.J.; Ciobanu, C.L.; Pring, A.; Skinner, W.; Shimizu, M.; Danyushevsky, L.; Saini-Eidukat, B.; Melcher, F. Trace and minor elements in sphalerite: A LA-ICPMS study. *Geochim. Cosmochim. Acta* **2009**, *73*, 4761–4791. [CrossRef]
89. McLimans, R.K.; Barnes, H.L.; Ohmoto, H. Sphalerite stratigraphy of the upper Mississippi Valley zinc-lead district, southwest Wisconsin. *Econ. Geol.* **1980**, *75*, 351–361. [CrossRef]
90. Paradis, S.; Petts, D.; Simandl, G.J.; Sharpe, R.; Hamilton, T.S.; Fayek, M.; Jackson, S.E. Impact of deformation and metamorphism on sphalerite chemistry—Element mapping of sphalerite in carbonate-hosted Zn-Pb sulfide deposits of the Kootenay Arc, southern British Columbia, Canada and northeastern Washington, USA. *Ore Geol. Rev.* **2023**, *158*, 105482. [CrossRef]
91. Urabe, T.; Sato, T. Kuroko deposits of the Kosaka Mine, Northeast Honshu, Japan; products of submarine hot springs on Miocene sea floor. *Econ. Geol.* **1978**, *73*, 161–179. [CrossRef]
92. Finlow-Bates, T. The possible significance of uncommon barium-rich mineral assemblages in sediment-hosted lead-zinc deposits. *Geol. En Mijnb.* **1987**, *66*, 65–66.
93. Kelley, K.D.; Leach, D.L.; Johnson, C.A.; Clark, J.L.; Fayek, M.; Slack, J.F.; Anderson, V.M.; Ayuso, R.A.; Ridley, W.I. Textural, compositional, and sulfur isotope variations of sulfide minerals in the Red Dog Zn-Pb-Ag deposits, Brooks Range, Alaska: Implications for ore formation. *Econ. Geol.* **2004**, *99*, 1509–1532. [CrossRef]
94. Magnall, J.M.; Gleeson, S.A.; Paradis, S. A new sub-seafloor replacement model for the Macmillan Pass clastic-dominant Zn-Pb ± Ba deposits (Yukon, Canada). *Econ. Geol.* **2020**, *115*, 953–959. [CrossRef]
95. Hayward, N.; Magnall, J.M.; Taylor, M.; King, R.; McMillan, N.; Gleeson, S.A. The Teena Zn-Pb deposit (McArthur Basin, Australia). Part I: Syndiagenetic base metal sulfide mineralization related to dynamic subbasin evolution. *Econ. Geol.* **2021**, *116*, 1743–1768. [CrossRef]
96. Kalogeropoulos, S.I.; Scott, S.D. On the genesis of barite associated with Volcanogenic Massive Sufides, Fukazawa Mine, Hokuroku District, Japan. In *Geology and Metallogeny of Copper Deposits*; Friedrich, G.H., et al., Eds.; Springer: Berlin/Heidelberg, Germany, 1986; pp. 370–388.

97. Ashton, J.H.; Blakeman, R.J.; Geraghty, J.F.; Beach, A.; Coller, D.; Philcox, M.E. The giant Navan carbonate hosted Zn–Pb deposit—A review. In *Current Perspectives on Zinc Deposits*; Archibald, S.M., Piercey, S.J., Eds.; Irish Association for Economic Geology: Dublin, Ireland, 2015; pp. 85–122.
98. Shen, Y.; Buick, R. The antiquity of microbial sulfate reduction. *Earth-Sci. Rev.* **2004**, *64*, 243–272. [CrossRef]
99. Gadd, M.G.; Layton-Mathews, D.; Peter, J.M.; Paradis, S.J.; Jonasson, I.R. The world-class Howard's Pass SEDEX Zn-Pb district, Selwyn Basin, Yukon. Part II: The roles of thermochemical and bacterial sulfate reduction in metal fixation. *Miner. Depos.* **2017**, *52*, 405–419. [CrossRef]
100. Scherp, A.; Strubel, G. Barium-strontium mineralization. *Miner. Depos.* **1974**, *9*, 155–168. [CrossRef]
101. Insley, M.W. Modification of sedimentary barite textures during deformation, Gataga District, NE British Columbia. *Ore Geol. Rev.* **1991**, *6*, 463–473. [CrossRef]
102. Johnson, C.A.; Emsbo, P.; Poole, F.G.; Rye, R.O. Sulfur- and oxygen-isotopes in sediment-hosted stratiform barite deposits. *Geochim. Cosmochim. Acta* **2009**, *73*, 133–147. [CrossRef]
103. Rajabi, A.; Mahmoodi, P.; Alfonso, P.; Canet, C.; Andrew, C.; Azhdari, S.; Rezaei, S.; Alaminia, Z.; Tamarzadeh, S.; Yarmohammadi, A.; et al. Barite replacement as a key factor in the genesis of sediment-hosted Zn-Pb±Ba and barite-sulfide deposits: Ore fluids and isotope (S and Sr) signatures from sediment-hosted Zn-Pb±Ba deposits of Iran. *Minerals* **2024**, *14*, 671. [CrossRef]
104. Jørgensen, B.B. A theoretical model of the stable sulphur isotope distribution in marine sediments. *Geochim. Cosmochim. Acta* **1979**, *43*, 363–374. [CrossRef]
105. Gomes, M.L.; Hurtgen, M.T. Sulfur isotope fractionation in modern euxinic systems: Implications for paleoenvironmental reconstructions of paired sulfate–sulfide isotope records. *Geochim. Cosmochim. Acta* **2015**, *157*, 39–55. [CrossRef]
106. Canfield, D.E.; Farquhar, J.; Zerkle, A.L. High isotope fractionations during sulfate reduction in a low-sulfate euxinic ocean analog. *Geology* **2010**, *38*, 415–418. [CrossRef]
107. Zhou, X.; Chen, D.; Dong, S.; Zhang, Y.; Guo, Z.; Wei, H.; Yu, H. Diagenetic barite deposits in the Yurtus Formation in Tarim Basin, NW China: Implications for barium and sulfur cycling in the earliest Cambrian. *Precambrian Res.* **2015**, *263*, 79–87. [CrossRef]
108. Canfield, D.E. Isotope fractionation by natural populations of sulfate-reducing bacteria. *Geochim. Cosmochim. Acta* **2001**, *65*, 1117–1124. [CrossRef]
109. Böttcher, M.E.; Effenberger, H.S.; Gehlken, P.-L.; Grathoff, G.H.; Schmidt, B.C.; Geprägs, P.; Bahlo, R.; Dellwig, O.; Leipe, T.; Winde, V.; et al. $BaMn(CO_3)_2$—A previously unrecognized double carbonate in low-temperature environments: Structural, spectroscopic, and textural tools for future identification. *Chem. Erde—Geochem.* **2012**, *72*, 85–89. [CrossRef]
110. Burdige, D.J. *Geochemistry of Marine Sediments*; Princeton University Press: Princeton, NJ, USA, 2006; p. 609.
111. Claypool, G.E.; Holser, W.T.; Kaplan, I.R.; Sakai, H.; Zak, I. The age curves of sulfur and oxygen isotopes in marine sulfate and their mutual interpretation. *Chem. Geol.* **1980**, *28*, 199–260. [CrossRef]
112. Killingworth, B.A.; Sansjofre, P.; Philippot, P.; Cartigny, P.; Thomazo, C.; Lalonde, S.V. Constraining the rise of oxygen with oxygen isotopes. *Nat. Commun.* **2019**, *10*, 4924. [CrossRef] [PubMed]
113. Greinert, J.; Bollwerk, S.M.; Derkachev, A.; Bohrmann, G.; Suess, E. Massive barite deposits and carbonate mineralization in the Derugin Basin, Sea of Okhotsk: Precipitation processes at cold seep sites. *Earth Planet. Sci. Lett.* **2002**, *203*, 165–180. [CrossRef]
114. Aharon, P.; Fu, B. Sulfur and oxygen isotopes of coeval sulfate-sulfide in pore waters and cold seep sediments with sharp redox gradients. *Chem. Geol.* **2003**, *195*, 201–218. [CrossRef]
115. Hemingway, J.D.; Olson, H.; Turchyn, A.V.; Johnston, D.T. Triple oxygen isotope insight into terrestrial pyrite oxidation. *Proc. Natl. Acad. Sci. USA* **2020**, *117*, 7650–7657. [CrossRef] [PubMed]
116. Bao, H.; Fairchild, I.J.; Wynn, P.M.; Spotl, C. Stretching the envelope of past surface environments: Neoproterozoic glacial lakes from Svalbard. *Science* **2009**, *323*, 119–122. [CrossRef]
117. Killingsworth, B.A.; Hayles, J.A.; Zhou, C.; Bao, H. Sedimentary constraints on the duration of the Marinoan Oxygen-17 Depletion (MOSD) event. *Proc. Natl. Acad. Sci. USA* **2013**, *110*, 17686–17690. [CrossRef]
118. Moro, C.M.; Cembranos, M.L.; Fernandez, A. Celsian, (Ba,K)-feldspar and cymrite from sedex barite deposits of Zamora, Spain. *Can. Mineral.* **2001**, *39*, 1039–1051. [CrossRef]
119. Wang, Z.; Li, G. Barite and witherite in Lower Cambrian shales of South China: Stratigraphic distribution and chemical characterization. *Econ. Geol.* **1991**, *86*, 354–363. [CrossRef]
120. Ansdell, K.M.; Nesbitt, B.E.; Longstaffe, F.J. A fluid inclusion and stable isotope study of the Tom Ba-Pb-Zn deposit, Yukon Territory, Canada. *Econ. Geol.* **1989**, *84*, 841–856. [CrossRef]
121. Gardner, H.D.; Hutcheon, I. Geochemistry, mineralogy, and geology of the Jason Pb-Zn deposits, Macmillan Pass, Yukon, Canada. *Econ. Geol.* **1985**, *80*, 1257–1276. [CrossRef]
122. Turner, R.J.W.; Goodfellow, W.D. *Barium Carbonate Bodies Associated with the Walt Stratiform Barite Deposit, Selwyn Basin, Yukon: A Possible Vent Complex Associated with a Middle Devonian Sedimentary Exhalative Barite Deposit*; Current Research, Part E, Paper 90-1E; Geological Survey of Canada: Regina, SK, Canada, 1990; pp. 309–319.
123. Lyons, T.W.; Gellatly, A.M.; McGoldrick, P.J.; Kah, L.C. Proterozoic sedimentary exhalative (SEDEX) deposits and links to evolving global ocean chemistry. In *Evolution of Early Earth's Atmosphere, Hydrosphere, and Biosphere: Constraints from Ore Deposits*; Kesler, S.E., Ohmoto, H., Eds.; Geological Society of America Memoir; GeoScienceWorld: McLean, VA, USA, 2006; Volume 198, pp. 169–184. [CrossRef]

124. Painter, M.G.M.; Golding, S.D.; Hannan, K.W.; Neudert, M.K. Sedimentologic, petrographic, and sulfur isotope constraints on fine-grained pyrite formation at Mount Isa Mine and environs, Northwest Queensland, Australia. *Econ. Geol.* **1999**, *94*, 883–912. [CrossRef]
125. Ye, L.; Cook, N.J.; Ciobanu, C.L.; Liu, Y.; Zhang, Q.; Liu, T.; Gao, W.; Yang, Y.; Danyushevskiy, L. Trace and minor elements in sphalerite from base metal deposits in South China: A LA-ICPMS study. *Ore Geol. Rev.* **2011**, *39*, 188–217. [CrossRef]
126. Yang, Q.; Zhang, X.; Ulrich, T.; Zhang, J.; Wang, J. Trace element compositions of sulfides from Pb-Zn deposits in the Northeast Yunnan and northwest Guizhou Provinces, SW China: Insights from LA-ICP-MS analyses of sphalerite and pyrite. *Ore Geol. Rev.* **2022**, *141*, 104639. [CrossRef]
127. Cave, B.; Lilly, R.; Hong, W. The effect of co-crystallising sulphides and precipitation mechanisms on sphalerite geochemistry: A case study from the Hilton Zn-Pb (Ag) deposit, Australia. *Minerals* **2020**, *10*, 797. [CrossRef]
128. Gadd, M.G.; Layton-Matthews, D.; Peter, J.M.; Paradis, S.J. The world-class Howard's Pass SEDEX Zn-Pb district, Selwyn Basin, Yukon. Part I: Trace element compositions of pyrite record input of hydrothermal, diagenetic and metamorphic fluids to mineralization. *Miner. Depos.* **2016**, *51*, 319–342. [CrossRef]
129. Wilkinson, J.J. The potential of Zn isotopes in the science and exploration of ore deposits. In *Isotopes in Economic Geology, Metallogenesis and Exploration*; Huston, D., Gutzmer, J., Eds.; Mineral Resource Reviews; Springer: Cham, Switzerland, 2023; pp. 451–463. [CrossRef]
130. Wilkinson, J.J.; Weiss, D.J.; Mason, T.F.D.; Coles, B.J. Zinc isotope variation in hydrothermal systems: Preliminary evidence from the Irish Midlands ore field. *Econ. Geol.* **2005**, *100*, 583–590. [CrossRef]
131. Kelley, K.D.; Wilkinson, J.J.; Chapman, J.B.; Crowther, H.L.; Weiss, D.J. Zinc isotopes in sphalerite from base metal deposits in the Red Dog district, northern Alaska. *Econ. Geol.* **2009**, *104*, 767–773. [CrossRef]

**Disclaimer/Publisher's Note:** The statements, opinions and data contained in all publications are solely those of the individual author(s) and contributor(s) and not of MDPI and/or the editor(s). MDPI and/or the editor(s) disclaim responsibility for any injury to people or property resulting from any ideas, methods, instructions or products referred to in the content.